Toward robust scalar-based gradient plasticity modeling and simulation at finite deformations

Mohamed Abatour, Samuel Forest, Kais Ammar, Cristian Ovalle, Nikolay Osipov, Stéphane Quilici

Toward robust scalar-based gradient plasticity modeling and simulation at finite deformations

Mohamed Abatour · Samuel Forest* · Kais Ammar · Cristian Ovalle · Nikolay Osipov · Stéphane Quilici

Abstract Strain gradient plasticity has been the subject of extensive research in the past forty years in order to model size effects in metal plasticity, on the one hand, and provide finite width shear bands in the simulation of localization phenomena, on the other hand. However, the use of the emerging models is still limited to academic applications and has not yet been adopted by industry practitioners. The present paper systematically reviews the pros and the cons of gradient plasticity at finite strains based on gradient of scalar plastic variables, in particular gradient of the cumulative plastic strain. It proposes benchmark tests addressing both size effect modeling and plastic strain localization simulation. It includes new analytical solutions for validation of FE implementation. It focuses on the micromorphic approach to gradient plasticity, as a convenient method for implementation in FE codes. New features of the analysis include the comparison of three distinct formulations of rate-independent gradient plasticity at finite deformations, based on the multiplicative decomposition of the deformation gradient and on quadratic potentials with respect to gradient terms. The performance of micromorphic and Lagrange-multiplier based strain gradient plasticity models is evaluated for various monotonic and cyclic loading conditions including confined plasticity in simple glide and tension, bending and torsion at large deformations. Limitations are pointed out in the case of bending and torsion, which can be overcome for instance by the use of the gradient of equivalent plastic strain model.

Keywords Micromorphic elastoplasticity · Strain gradient plasticity · Strain localization · Finite deformation · Finite strain · Regularization · Size effect

1 Introduction

Many experiments have revealed the size-dependent nature of metal plasticity characterized by intrinsic length scales interacting with small specimen dimensions: grain size effects in thin films [1], the bending of thin foils [2], torsion of copper wires reviewed in [3] until more recent experiments on confined plasticity in thin films [4]. In general, a *smaller is stronger* effect has been reported. The presence of plastic strain gradients leads to enhanced hardening due to the generation of geometrically necessary dislocations [5–7]. The conventional plasticity

* *Corresponding author,* E-mail: samuel.forest@minesparis.psl.eu

M. Abatour · S. Forest[1] · K. Ammar · C. Ovalle
Mines Paris, PSL University, Centre for material sciences (MAT), UMR7633 CNRS, 91003 Evry, France

N. Osipov · S. Quilici
TRANSVALOR S.A., Centre d'affaires la Boursidière, 92357 Le Plessis-Robinson, France

theory is well established and is predictive to some extent. However, the size effects cannot be captured by classical models since no length scale enters the constitutive equations.

On the other hand, strain-softening leads to ill-posed boundary value problems in classical continuum theories. This is due to the loss of ellipticity of the governing partial differential equations in the rate-independent case. The numerical simulations are therefore sensitive to mesh size [8], orientation of element edges [9] and element types. Various types of regularization methods are studied in literature relying on non-local integral operators [10], gradient formulations [11] or extra-degrees of freedom for smoothing strain or damage fields [12]. Further, this spurious mesh dependency can also be solved partially for rate-dependent models [13] provided that rate sensitivity is high enough. Many regularization methods are intrusive regarding their FE implementation. The advantage of scalar micromorphic approaches involving one additional degree for freedom lies in its relative simplicity of implementation as illustrated by its use in explicit codes [14–16].

The mechanics of generalized continua enables the introduction of characteristic lengths into constitutive equations of materials with microstructure. For instance, the micromorphic continuum theory was first proposed in [17, 18]. In this theory, a deformable triad of directors is defined at each material point. Higher-order theories are constructed then by endowing material points by tensors of various orders [19]. These tensors can be related to either deformation measures or internal variables. Various micromorphic models using scalar and tensor variables accounting for elasticity, plasticity, and damage have been suggested in [14, 20, 21]. In crystal plasticity, models with one micromorphic variable accounting for plastic strain in all slip systems are used in order to decrease the number of additional degrees of freedom [22–25]. Many contributions in strain gradient and micromorphic plasticity rely on quadratic potentials with respect to the gradient terms. Limitations of quadratic potentials have been recognized in [26, 27] by comparison with scaling laws from mechanical metallurgy. Rank 1 and logarithmic potentials were proposed by [28–33] based on dislocation density arguments, whereas general power-law potentials are used by [34–36].

Finite strain modeling of elastoplasticity has been studied for decades and is still the subject of current research. The widely used approach to extend the well-established infinitesimal elastoplasticity theory to finite deformations is the so-called hypoelastic formulation relying on the additive decomposition of the total deformation rate into elastic and inelastic parts, and constitutive equations for objective stress rates. However, these formulations suffer from several shortcomings. For instance, spurious energy dissipation in the elastic regime before yield and at post-yield, see [37] and references quoted therein. Formulations relying upon the additive decomposition of the Green-Lagrange strain tensor were developed for isotropic materials in [38] and the additive split of logarithmic strain was suggested in [39]. Several authors have advocated the multiplicative decomposition as a general way of describing the kinematics at finite strain [40, 41]. This decomposition assumes the existence of an intermediate configuration that is generally not unique. The concept of isoclinic intermediate configuration was proposed first in [42] to overcome this limitation.

A general framework for the formulation of generalized continuum constitutive equations at finite deformations based on the multiplicative decomposition was proposed in [43] for Cosserat, strain gradient, micromorphic and gradient of internal variable media. These models are applicable to the modeling of size effects in plasticity of materials as well as the simulation of strain localization phenomena. As summarized in [44], finite strain formulations for strain gradient plasticity lead to distinct regularization operators. Non-coaxial deformations, such as simple glide, reveal significant differences between finite strain formulations, as recently discussed for the micromorphic approach of plasticity in [45]. In particular, the formulation based on additive logarithmic strain decomposition under non-coaxial deformation yields a softer response and eventually leads to early strain localization compared to the multiplicative elastoplasticity. Further investigations on Lagrangian and Eulerian non-local effects were conducted by , *e.g.* [46–49]. According to these works, various formulations de-

viate from each other at finite strain, but with no clear preference. It remains that only few studies were dedicated to the computational analysis of strain gradient plasticity at large deformations, see for instance in [50] based on the gradient of the plastic strain tensor, and [23, 51, 52] for the gradient of scalar variables.

The present work focuses on the micromorphic approach based on the gradient of scalar variables because this class of models remains rather easy to implement in FE codes and provides computationally efficient simulations due to the reduced number of additional degrees of freedom. Several issues related to the particular choice of scalar micromorphic variable are reported in the literature. First, the gradient enhancement may lead to a negative isotropic hardening and ultimately to a non-physical negative radius of elastic domain [53]. Further, scalar variables do not account for flow direction [54]. A scalar enhanced model has been proposed in [55] at small strain to solve this conceptual problem. A tensorial gradient plasticity model was proposed in [53] to address the aforementioned issues but this model remains numerically expensive. Theories involving the gradient of the full plastic strain tensor go back to the works [43, 56–58], these references being limited to the small strain case. The numerical implementation of strain gradient theories has been widely investigated. An implementation of strain gradient plasticity based on Lagrange multipliers has been proposed in [59]. It consists in duplicating the considered variable, one is local and one is non-local and these two variables are then constrained to be equal. An augmented Lagrangian term was introduced to prevent plastic strain oscillations [60, 61]. The computational cost of micromorphic and Lagrange multiplier-based approaches are compared for a rate-(in)dependent single crystal model in [25]. In that case, the authors suggest that the computational performance can be improved by considering the Lagrange multiplier-based formulation. The previous enhanced plasticity theories have been tested against benchmark problems, like thin film behavior under biaxial tension, torsion of wires, but also growth of a spherical void in [57], and bending [53].

The objective of the present work is to provide a series of benchmark tests addressing both size effects in hardening plasticity and simulation of localization phenomena in softening plasticity in order to evaluate the performance of the approach both theoretically and computationally and investigate its limitations. Verification of the proposed finite element implementation is performed via analytical solutions at small strains for hardening and softening plasticity. The considered boundary value problems are simulated according to three distinct formulations of the model at finite deformations. At finite strain, the gradient of the micromorphic variable is defined with respect to (w.r.t.) either the reference, current or intermediate configurations. The free energy potential is assumed to be a quadratic form w.r.t. to one of this gradient variables. This results in three distinct models that will be compared throughout this work for monotonic and cyclic loading conditions. The present approach is applied to size effects in two cases. First, plastic gradients are induced by particular boundary conditions applied to the micromorphic variable corresponding to confined plasticity or passivation of surfaces. Further, gradients emerge from the geometry and the loading in the case of bending and torsion applications. The torsion case is considered in 3D in order to evaluate the computational efficiency of the models and their implementation. Finally, the capability of these models to cancel the spurious mesh dependency is investigated through applications involving strain localization. The present approach is compared in terms of computational cost to the Lagrange multiplier-based approach.

The paper reviews several aspects of micromorphic plasticity but also presents novel features. First, the three finite deformation frameworks are compared for the first time to highlight the differences at large deformations under complex loading. Second, the analysis of cyclic shear, tension and bending using several models shows significantly different material responses ranging from unbounded size-dependent isotropic hardening to several types of size-dependent kinematic hardening. In particular, a new model based on the gradient of an equivalent strain measure at finite deformation is proposed and shown to overcome some

drawbacks of the initial approach. Then, original applications are presented for plastic strain localization in shear and tension. A new analytical solution is presented for shear localization describing the micromorphic model response in detail and thus providing sophisticated verification of the FE implementation. An anisotropic gradient contribution is finally proposed showing the interplay between two length scales during double shear banding in a plate in tension.

The outline of the paper is as follows. The general micromorphic approach for finite strain gradient plasticity is presented in Sec. 2. The special case of scalar micromorphic variables is put forward. Three different finite strain formulations are discussed relying upon gradient variables defined w.r.t. reference, current or intermediate configurations. A strain gradient plasticity model based on Lagrange multipliers is revisited. The finite element implementation is discussed briefly. The capability of different micromorphic formulations to predict size effects is discussed in Sec. 3 for a unit cell subjected to simple glide and tension under confined plasticity boundary conditions. In Sec. 4, size effects in the case of bending of a two-dimensional foil and torsion of a cylindrical bar are investigated. The case of strain localization is addressed in Sec. 5 for a unit cell subjected to simple glide and a plate under tension. Finally, the computational efficiency and the limitations of the approach are discussed in Sec. 6.

According to the notations used throughout this work, first, second and fourth rank tensors are written $\underline{\boldsymbol{a}}$, $\underline{\underline{\boldsymbol{a}}}$ and $\underline{\underline{\underline{\boldsymbol{a}}}}$, respectively. Divergence operator w.r.t. Lagrangian (resp. Eulerian) coordinates is called Div (resp. div). Note that the components of the gradient of a second order tensor $\underline{\underline{\boldsymbol{A}}}$ are taken as $A_{ij,k}$ in a Cartesian orthonormal coordinate system. Its divergence is the trace of the gradient with respect to the last two indices. The scalar product of two vectors is $\underline{\boldsymbol{a}} \cdot \underline{\boldsymbol{b}} = a_i b_i$. The double contraction of two generally non symmetric second order tensors is $\underline{\underline{\boldsymbol{A}}} : \underline{\underline{\boldsymbol{B}}} = A_{ij} B_{ij}$. The inverse of the transpose of $\underline{\underline{\boldsymbol{A}}}$ is $\underline{\underline{\boldsymbol{A}}}^{-T}$. The material points are located at position $\underline{\boldsymbol{X}}$ in the reference configuration. The current position of the material point is $\underline{\boldsymbol{x}}$, at time t. The analysis is limited to the isothermal case for the sake of brevity although extensions to thermomechanics are possible [20, 62]. All the two-dimensional simulations presented in this work are performed under plane strain conditions.

2 Model formulation at finite deformation and FE implementation

According to the classical Cauchy continuum theory, the material body is characterized by a set of degrees of freedom $DOF0 = \{\underline{\boldsymbol{u}}\}$ and state variables $STATE0 = \{\underline{\underline{\boldsymbol{F}}}, T, \boldsymbol{\alpha}_I\}$. The displacement field, the deformation gradient, and temperature are denoted respectively by $\underline{\boldsymbol{u}}$, $\underline{\underline{\boldsymbol{F}}}$, and T, whereas $\boldsymbol{\alpha}_I$ represent scalar and tensor internal variables accounting for hardening/softening properties. The micromorphic approach proposed in [20] at small strains and in [44] at finite deformations, is a systematic enhancement of the classical continuum and constitutive theory to account for size and microstructure internal length effects. Supplementary degrees of freedom, denoted by χ, associated with selected internal variables are introduced, *i.e.* $DOF = \{\underline{\boldsymbol{u}}, \chi\}$. The micromorphic variables and related internal variables have the same tensor rank and physical dimension. The set of material state variables is enriched by the micromorphic variable χ and its gradient $\nabla\chi$, *i.e.* $STATE = \{\underline{\underline{\boldsymbol{F}}}, T, \boldsymbol{\alpha}_I, \chi, \nabla\chi\}$. In what follows, notations are used for a scalar micromorphic variable, even though similar equations are valid for tensor variables as well, but the present work addresses exclusively the case of scalar variables.

2.1 Kinematics and balance equations of the reduced micromorphic elasto(visco)plasticity continuum

The deformation gradient is decomposed multiplicatively following [40–42] into elastic and inelastic parts as

$$\underset{\sim}{\boldsymbol{F}} = \underset{\sim}{\boldsymbol{F}}^{e}\,\underset{\sim}{\boldsymbol{F}}^{p} \tag{1}$$

Following [42], the isoclinic local intermediate configuration, where the material directors describing the anisotropic material behavior have the same inclination or orientation as in the reference configuration, is adopted. This intermediate configuration is then uniquely defined up to an element of the material symmetry group.
The total, elastic and plastic relative volume changes are denoted by J, J_e and J_p, respectively:

$$J = \frac{\rho_0}{\rho} = \det\left(\underset{\sim}{\boldsymbol{F}}\right) \quad , \quad J_e = \frac{\overline{\rho}}{\rho} = \det\left(\underset{\sim}{\boldsymbol{F}}^{e}\right) \quad , \quad J_p = \frac{\rho_0}{\overline{\rho}} = \det\left(\underset{\sim}{\boldsymbol{F}}^{p}\right) \tag{2}$$

where ρ, $\overline{\rho}$ and ρ_0 denote the mass density in the current, intermediate and reference local configurations, respectively. The Lagrangian gradient of additional degrees of freedom $\underline{\boldsymbol{K}} = \dfrac{\partial \chi}{\partial \underline{\boldsymbol{X}}}$ and the Eulerian gradient $\underline{\boldsymbol{k}} = \dfrac{\partial \chi}{\partial \underline{\boldsymbol{x}}}$ are related by

$$\underline{\boldsymbol{k}} = \underset{\sim}{\boldsymbol{F}}^{-T}\,\underline{\boldsymbol{K}} \tag{3}$$

Likewise, a generalized variable $\underline{\overline{\boldsymbol{K}}}$ can be defined w.r.t. the intermediate configuration as

$$\underline{\overline{\boldsymbol{K}}} = \underset{\sim}{\boldsymbol{F}}^{p-T}\,\underline{\boldsymbol{K}} = \underset{\sim}{\boldsymbol{F}}^{eT}\,\underline{\boldsymbol{k}} \tag{4}$$

It must be noted that $\underline{\overline{\boldsymbol{K}}}$ is *not* a gradient field since it is generally not compatible. The power density of internal forces expressed w.r.t. the current configuration, $\mathcal{P}^{(i)}$, is given by

$$\mathcal{P}^{(i)} = \underset{\sim}{\boldsymbol{\sigma}} : \underset{\sim}{\boldsymbol{D}} + a\dot{\chi} + \underline{\boldsymbol{b}} \cdot \underline{\dot{\boldsymbol{k}}} \tag{5}$$

with $\underset{\sim}{\boldsymbol{\sigma}}$ is the Cauchy stress, $\underset{\sim}{\boldsymbol{D}}$ the strain rate tensor, a and $\underline{\boldsymbol{b}}$ are generalized stresses associated with the micromorphic variable and its first gradient. By neglecting volume forces for the sake of brevity, the principle of virtual power is written for all subdomains D of the current configuration Ω of the body as follows

$$\int_D \mathcal{P}^{(i)} dV = \int_{\partial D} \left(\underline{\boldsymbol{t}}.\underline{\dot{\boldsymbol{u}}} + a^c \dot{\chi}\right) dS \quad , \quad \forall D \subset \Omega \tag{6}$$

External forces arise from macroscopic surface traction $\underline{\boldsymbol{t}}$ and a generalized surface traction a^c related to the micromorphic variable. The application of the virtual power principle, w.r.t. the generalized set of independent degrees of freedom, leads to the static balance laws in the current configuration in the form

$$\begin{cases} \operatorname{div} \underset{\sim}{\boldsymbol{\sigma}} &= \underline{\boldsymbol{0}} \\ \operatorname{div} \underline{\boldsymbol{b}} &= a \end{cases} \quad \forall \underline{\boldsymbol{x}} \in \Omega \qquad \begin{cases} \underline{\boldsymbol{t}} &= \underset{\sim}{\boldsymbol{\sigma}} \cdot \underline{\boldsymbol{n}} \\ a^c &= \underline{\boldsymbol{b}} \cdot \underline{\boldsymbol{n}} \end{cases} \quad \forall \underline{\boldsymbol{x}} \in \partial\Omega \tag{7}$$

where $\underline{\boldsymbol{n}}$ denotes the outward surface unit normal. The power density of internal forces expressed w.r.t. the reference configuration $\mathcal{P}_0^{(i)} = J\mathcal{P}^{(i)}$ is given by

$$\mathcal{P}_0^{(i)} = \underset{\sim}{\boldsymbol{P}} : \underset{\sim}{\dot{\boldsymbol{F}}} + a_0\dot{\chi} + \underline{\boldsymbol{b}}_0 \cdot \underline{\dot{\boldsymbol{K}}} \quad , \quad \forall \underline{\boldsymbol{X}} \in \Omega_0 \tag{8}$$

where the generalized stresses a_0 and $\underline{\boldsymbol{b}}_0$ are related to a and $\underline{\boldsymbol{b}}$ by

$$a_0 = \frac{\rho_0}{\rho} a = Ja, \qquad \underline{\boldsymbol{b}}_0 = J\underset{\sim}{\boldsymbol{F}}^{-1}\underline{\boldsymbol{b}} \tag{9}$$

and $\underset{\sim}{\boldsymbol{P}} = J\underset{\sim}{\boldsymbol{\sigma}}\underset{\sim}{\boldsymbol{F}}^{-T}$ is the Boussinesq stress tensor. In the reference configuration, Eq. (6) becomes

$$\int_{D_0} \mathcal{P}_0^{(i)} dV_0 = \int_{\partial D_0} (\underline{\boldsymbol{T}}.\underline{\dot{\boldsymbol{u}}} + a_0^c \dot{\chi})\, dS_0 \quad , \quad \forall D_0 \subset \Omega_0 \tag{10}$$

where D_0 is a subdomain of the reference configuration Ω_0 of the body. Furthermore, the balance laws write

$$\begin{cases} \mathrm{Div}(\underset{\sim}{\boldsymbol{P}}) & = \underline{\boldsymbol{0}} \\ \mathrm{Div}(\underline{\boldsymbol{b}}_0) & = a_0 \end{cases} \quad \forall \underline{\boldsymbol{X}} \in \Omega_0 \qquad \begin{cases} \underline{\boldsymbol{T}} & = \underset{\sim}{\boldsymbol{P}} \cdot \underline{\boldsymbol{n}}_0 \\ a_0^c & = \underline{\boldsymbol{b}}_0 \cdot \underline{\boldsymbol{n}}_0 \end{cases} \quad \forall \underline{\boldsymbol{X}} \in \partial\Omega_0 \tag{11}$$

where $\underline{\boldsymbol{n}}_0$ is the outward surface normal and $\underline{\boldsymbol{T}}$ is the surface traction measured on the reference boundary ∂D_0. Likewise, the power density of internal forces is rewritten w.r.t. the intermediate local configuration[1] $\overline{\mathcal{P}}^{(i)} = J_e \mathcal{P}^{(i)}$ as

$$\overline{\mathcal{P}}^{(i)} = \frac{1}{2}\underset{\sim}{\boldsymbol{\Pi}}^e : \dot{\underset{\sim}{\boldsymbol{C}}}^e + (\underset{\sim}{\boldsymbol{M}} + \underline{\overline{\boldsymbol{K}}} \otimes \underline{\overline{\boldsymbol{b}}}) : \underset{\sim}{\overline{\boldsymbol{L}}}^p + \overline{a}\dot{\chi} + \underline{\overline{\boldsymbol{b}}} \cdot \underline{\dot{\overline{\boldsymbol{K}}}} \tag{12}$$

where $\underline{\overline{\boldsymbol{b}}} = J_e \underset{\sim}{\boldsymbol{F}}^{e-1} \underline{\boldsymbol{b}} = \dfrac{1}{J_p} \underset{\sim}{\boldsymbol{F}}^p \underline{\boldsymbol{b}}_0$ and $\overline{a} = J_e a = \dfrac{a_0}{J_p}$. The Cauchy-Green elastic strain measure defined on the intermediate local configuration is $\underset{\sim}{\boldsymbol{C}}^e = \underset{\sim}{\boldsymbol{F}}^{eT} \underset{\sim}{\boldsymbol{F}}^e$. The Piola stress tensor w.r.t. the intermediate local configuration is $\underset{\sim}{\boldsymbol{\Pi}}^e = J_e \underset{\sim}{\boldsymbol{F}}^{e-1} \underset{\sim}{\boldsymbol{\sigma}} \underset{\sim}{\boldsymbol{F}}^{e-T}$. The plastic velocity gradient $\underset{\sim}{\boldsymbol{L}}^p$ is the work-conjugate of the Mandel stress tensor $\underset{\sim}{\boldsymbol{M}} = \underset{\sim}{\boldsymbol{C}}^e \underset{\sim}{\boldsymbol{\Pi}}^e$. The expression of the virtual power w.r.t. the various local configurations are related by the following

$$\frac{\overline{\mathcal{P}}^{(i)}}{\overline{\rho}} = \frac{\mathcal{P}^{(i)}}{\rho} = \frac{\mathcal{P}_0^{(i)}}{\rho_0} \tag{13}$$

2.2 On three forms of the Helmholtz free energy potential

The mass specific Helmholtz free energy density function for classical elasto(visco)plasticity models, ψ^{ref}, depends on the elastic strain tensor $\underset{\sim}{\boldsymbol{C}}^e$ and internal variables $\boldsymbol{\alpha}_I$, both quantities attached to the intermediate local configuration, according to [63].

The next constitutive choice is to select the dependence of the free energy potential on the micromorphic variables. For that purpose, the total free energy is split into two functions in the form:

$$\psi = \psi^{ref} + \psi^{\chi} \tag{14}$$

where the micromorphic contribution is incorporated into the function ψ^{χ}. The latter is chosen to depend explicitly on one internal variable taken from the set $\boldsymbol{\alpha}_I$, on the micromorphic variable χ and on either $\underline{\boldsymbol{k}}, \underline{\boldsymbol{K}}$ or $\underline{\overline{\boldsymbol{K}}}$. In that way, three distinct functions, $\psi^{\chi}(\boldsymbol{\alpha}_I, \chi, \underline{\boldsymbol{k}}), \psi_0^{\chi}(\boldsymbol{\alpha}_I, \chi, \underline{\boldsymbol{K}}), \overline{\psi}^{\chi}(\boldsymbol{\alpha}_I, \chi, \underline{\overline{\boldsymbol{K}}})$, can be considered that differ only by the choice of the third argument.

[1] To establish this expression, the following equation was used

$$\underline{\dot{\boldsymbol{K}}} = \underset{\sim}{\boldsymbol{F}}^{pT} \underline{\dot{\overline{\boldsymbol{K}}}} + \underset{\sim}{\dot{\boldsymbol{F}}}^{pT} \underline{\overline{\boldsymbol{K}}}$$

Conversion between the three free energy potentials

The free energy potential is an isotropic function of its arguments, the arguments including structural tensors in the case of anisotropic materials [64, 65]. In particular, the dependence on the gradient of the micromorphic variable must fulfill this requirement. This allows for conversion of free energy function from one set of arguments to the others:

$$\begin{aligned}\psi(\underset{\sim}{\boldsymbol{C}}^e, \boldsymbol{\alpha}_I, \chi, \underline{\boldsymbol{k}}) &= \psi(\underset{\sim}{\boldsymbol{C}}^e, \boldsymbol{\alpha}_I, \chi, \underset{\sim}{\boldsymbol{F}}^{-T}\underline{\boldsymbol{K}}) \\ &= \psi(\underset{\sim}{\boldsymbol{C}}^e, \boldsymbol{\alpha}_I, \chi, \underset{\sim}{\boldsymbol{U}}^{-T}\underline{\boldsymbol{K}}) \\ &=: \psi_0(\underset{\sim}{\boldsymbol{C}}^e, \underset{\sim}{\boldsymbol{C}}, \boldsymbol{\alpha}_I, \chi, \underline{\boldsymbol{K}}) \end{aligned} \tag{15}$$

by virtue of space isotropy principle applied at the second line. The right stretch tensor $\underset{\sim}{\boldsymbol{U}} = \underset{\sim}{\boldsymbol{C}}^{1/2}$ was introduced. It is apparent from this expression that a function $\psi(\underset{\sim}{\boldsymbol{C}}^e, \boldsymbol{\alpha}_I, \chi, \underline{\boldsymbol{k}})$ cannot be converted into a function $\psi_0(\underset{\sim}{\boldsymbol{C}}^e, \boldsymbol{\alpha}_I, \chi, \underline{\boldsymbol{K}})$. The conversion is only possible if adding the right Cauchy–Green as an argument. On the other hand,

$$\begin{aligned}\psi(\underset{\sim}{\boldsymbol{C}}^e, \boldsymbol{\alpha}_I, \chi, \underline{\boldsymbol{k}}) &= \psi(\underset{\sim}{\boldsymbol{C}}^e, \boldsymbol{\alpha}_I, \chi, \underset{\sim}{\boldsymbol{F}}^{e-T}\overline{\underline{\boldsymbol{K}}}) \\ &= \psi(\underset{\sim}{\boldsymbol{C}}^e, \boldsymbol{\alpha}_I, \chi, \underset{\sim}{\boldsymbol{U}}^{e-T}\overline{\underline{\boldsymbol{K}}}) \\ &=: \overline{\psi}(\underset{\sim}{\boldsymbol{C}}^e, \boldsymbol{\alpha}_I, \chi, \overline{\underline{\boldsymbol{K}}}) \end{aligned} \tag{16}$$

In that case, conversion from a function $\psi(\underset{\sim}{\boldsymbol{C}}^e, \boldsymbol{\alpha}_I, \chi, \underline{\boldsymbol{k}})$ to a function of the form $\overline{\psi}(\underset{\sim}{\boldsymbol{C}}^e, \boldsymbol{\alpha}_I, \chi, \overline{\underline{\boldsymbol{K}}})$ is always possible.

In the present work, quadratic contributions to the free energy density w.r.t. either $\underline{\boldsymbol{k}}$, $\underline{\boldsymbol{K}}$ or $\overline{\underline{\boldsymbol{K}}}$, will be considered for simplicity. In the isotropic case, a quadratic contribution with respect to $\underline{\boldsymbol{k}}$ takes the form:

$$\frac{1}{2}A\|\underline{\boldsymbol{k}}\|^2 = \frac{1}{2}A\underline{\boldsymbol{k}} \cdot \underline{\boldsymbol{k}} \tag{17}$$

where A is a constant material parameter regarded as a higher order modulus. It is apparent that a quadratic contribution w.r.t. $\underline{\boldsymbol{k}}$ can be converted into non–quadratic expressions for $\underline{\boldsymbol{K}}$ and $\overline{\underline{\boldsymbol{K}}}$, in the following ways:

$$\frac{1}{2}A\underline{\boldsymbol{k}} \cdot \underline{\boldsymbol{k}} = \frac{1}{2}A\underline{\boldsymbol{K}} \cdot \underset{\sim}{\boldsymbol{C}}^{-1} \cdot \underline{\boldsymbol{K}} = \frac{1}{2}A\overline{\underline{\boldsymbol{K}}} \cdot \underset{\sim}{\boldsymbol{C}}^{e-1} \cdot \overline{\underline{\boldsymbol{K}}} \tag{18}$$

As a consequence, adopting a quadratic contribution w.r.t. $\underline{\boldsymbol{K}}$, $\underline{\boldsymbol{k}}$ or $\overline{\underline{\boldsymbol{K}}}$ leads to three *distinct* material models. The corresponding responses will be compared in the various examples handled in the following.

Multiplicative elastoplasticity constitutive equations are naturally expressed w.r.t. the intermediate configuration, the Mandel stress being the driving force for plastic flow. The state and internal variables are all expressed w.r.t. the intermediate configuration: Elastic Green-Lagrange strain and hardening variables. This is the motivation for bringing also the higher order variable $\underline{\boldsymbol{K}}$ into the intermediate configuration to obtain $\bar{\underline{\boldsymbol{K}}}$. Generally, it is more consistent to consider all the arguments of the free energy density function w.r.t. the same configuration and avoid mixing variables defined on distinct configurations. In that way invariance requirements related to symmetry can be applied without ambiguity.

The case of an anisotropic contributions of $\underline{\boldsymbol{K}}$, $\underline{\boldsymbol{k}}$ or $\overline{\underline{\boldsymbol{K}}}$ will also be considered and the discussion is postponed to Sec. 5.2.

2.3 Exploitation of entropy principle and constitutive equations

The entropy principle in its local form is now exploited with the simplifying assumption of non-dissipative generalized stresses (a, $\underline{\boldsymbol{b}}$, a_0, $\underline{\boldsymbol{b}}_0$, $\overline{a}$ and $\overline{\underline{\boldsymbol{b}}}$). Three formulations are presented depending on the use of $\underline{\boldsymbol{K}}$, $\overline{\underline{\boldsymbol{K}}}$ or $\underline{\boldsymbol{k}}$ as an argument of the free energy potential:

Eulerian formulation The dissipation inequality is written as:

$$\mathcal{P}^{(i)} - \rho\dot{\psi} \geq 0 \tag{19}$$

The rate of change of free energy density is evaluated as

$$\dot{\psi}(\underset{\sim}{\boldsymbol{C}}^e, \boldsymbol{\alpha}_I, \chi, \underline{\boldsymbol{k}}) = \frac{\partial \psi}{\partial \underset{\sim}{\boldsymbol{C}}^e} : \dot{\underset{\sim}{\boldsymbol{C}}}^e + \frac{\partial \psi}{\partial \boldsymbol{\alpha}_I}\dot{\boldsymbol{\alpha}}_I + \frac{\partial \psi}{\partial \chi}\dot{\chi} + \frac{\partial \psi}{\partial \underline{\boldsymbol{k}}} \cdot \dot{\underline{\boldsymbol{k}}} \tag{20}$$

By substituting Eq. (5) and the previous equation in the dissipation inequality Eq. (19), the Clausius–Duhem inequality is obtained

$$\left(\frac{1}{2J_e}\underset{\sim}{\boldsymbol{\Pi}}^e - \rho\frac{\partial \psi}{\partial \underset{\sim}{\boldsymbol{C}}^e}\right) : \dot{\underset{\sim}{\boldsymbol{C}}}^e + \frac{1}{J_e}\underset{\sim}{\boldsymbol{M}} : \overline{\underset{\sim}{\boldsymbol{L}}}^p + \left(a - \rho\frac{\partial \psi}{\partial \chi}\right)\dot{\chi} + \left(\underline{\boldsymbol{b}} - \rho\frac{\partial \psi}{\partial \underline{\boldsymbol{k}}}\right)\cdot\dot{\underline{\boldsymbol{k}}} - \rho\frac{\partial \psi}{\partial \boldsymbol{\alpha}_I}\dot{\boldsymbol{\alpha}}_I \geq 0 \tag{21}$$

where the Mandel stress tensor $\underset{\sim}{\boldsymbol{M}} = \underset{\sim}{\boldsymbol{C}}^e\underset{\sim}{\boldsymbol{\Pi}}^e$ is the driving force for plastic flow. Since Eq. (21) holds true for any mechanical process (*i.e.* for any $\dot{\underset{\sim}{\boldsymbol{C}}}^e$, $\dot{\chi}$ and $\dot{\underline{\boldsymbol{k}}}$), and assuming that the conjugate functions do not depend on these increments, the following state laws are derived

$$\underset{\sim}{\boldsymbol{\Pi}}^e = 2\overline{\rho}\frac{\partial \psi}{\partial \underset{\sim}{\boldsymbol{C}}^e} \quad , \quad a = \rho\frac{\partial \psi}{\partial \chi} \quad , \quad \underline{\boldsymbol{b}} = \rho\frac{\partial \psi}{\partial \underline{\boldsymbol{k}}} \quad , \quad \boldsymbol{A_I} = \overline{\rho}\frac{\partial \psi}{\partial \boldsymbol{\alpha}_I} \tag{22}$$

The latter equation defines the thermodynamic forces $\boldsymbol{A_I}$ associated with the internal variables $\boldsymbol{\alpha}_I$. The residual dissipation rate takes the form

$$\underset{\sim}{\boldsymbol{M}} : \overline{\underset{\sim}{\boldsymbol{L}}}^p - \boldsymbol{A_I}\dot{\boldsymbol{\alpha}}_I \geq 0 \tag{23}$$

The previous condition of positive dissipation is automatically satisfied when there exists a convex potential $\Omega(\underset{\sim}{\boldsymbol{M}}, \boldsymbol{A_I})$ providing the flow rule and evolution equations for the internal variables:

$$\overline{\underset{\sim}{\boldsymbol{L}}}^p = \frac{\partial \Omega}{\partial \underset{\sim}{\boldsymbol{M}}} \quad , \quad \dot{\boldsymbol{\alpha}}_I = -\frac{\partial \Omega}{\partial \boldsymbol{A_I}} \tag{24}$$

The existence of such a dissipation potential is convenient but not necessary. In the rate-independent case, the dissipation potential is related to the yield function $f(\underset{\sim}{\boldsymbol{M}}, \underset{\sim}{\boldsymbol{A}}_I)$ by the normality rule

$$\overline{\underset{\sim}{\boldsymbol{L}}}^p = \dot{p}\frac{\partial f}{\partial \underset{\sim}{\boldsymbol{M}}} \quad , \quad \dot{\boldsymbol{\alpha}}_I = -\dot{p}\frac{\partial f}{\partial \boldsymbol{A_I}} \tag{25}$$

where $\dot{p}$ is the plastic multiplier. The cumulative plastic strain results from the time integration the plastic multiplier.

Lagrangian formulation Alternatively, the Lagrangian version of the Clausius–Duhem inequality reads

$$\left(\frac{J_p}{2}\underset{\sim}{\boldsymbol{\Pi}}^e - \rho_0\frac{\partial \psi_0}{\partial \underset{\sim}{\boldsymbol{C}}^e}\right) : \dot{\underset{\sim}{\boldsymbol{C}}}^e + J_p\underset{\sim}{\boldsymbol{M}} : \overline{\underset{\sim}{\boldsymbol{L}}}^p + \left(a_0 - \rho_0\frac{\partial \psi_0}{\partial \chi}\right)\dot{\chi} + \left(\underline{\boldsymbol{b}}_0 - \rho_0\frac{\partial \psi_0}{\partial \underline{\boldsymbol{K}}}\right)\cdot\dot{\underline{\boldsymbol{K}}} - \rho_0\frac{\partial \psi_0}{\partial \boldsymbol{\alpha}_I}\dot{\boldsymbol{\alpha}}_I \geq 0 \tag{26}$$

and constitutive equations are derived as follows

$$\underset{\sim}{\boldsymbol{\Pi}}^e = 2\overline{\rho}\frac{\partial \psi_0}{\partial \underset{\sim}{\boldsymbol{C}}^e} \quad , \quad a_0 = \rho_0\frac{\partial \psi_0}{\partial \chi} \quad , \quad \underline{\boldsymbol{b}}_0 = \rho_0\frac{\partial \psi_0}{\partial \underline{\boldsymbol{K}}} \quad , \quad \boldsymbol{A_I} = \overline{\rho}\frac{\partial \psi_0}{\partial \boldsymbol{\alpha}_I} \tag{27}$$

The equations (23,24) and (25) apply in this case as well.

A drawback of the two previous constitutive formulations is that they combine variables defined on different local configurations. Appropriate push-forward or pull-back operations make it possible to consider variables all defined on the intermediate local configuration, as proposed in [44]. For that purpose, use is made of the variable $\underline{\boldsymbol{K}}$ which is the pull-back of $\underline{\boldsymbol{k}}$ to the intermediate local configuration.

Formulation w.r.t. the intermediate configuration In that case, the dissipation inequality was derived in [44] as

$$\left(\frac{1}{2}\underset{\sim}{\boldsymbol{\Pi}}^e - \overline{\rho}\frac{\partial\overline{\psi}}{\partial\underset{\sim}{\boldsymbol{C}}^e}\right) : \dot{\underset{\sim}{\boldsymbol{C}}}^e + (\underset{\sim}{\boldsymbol{M}} + \overline{\underline{\boldsymbol{K}}}\otimes\overline{\underline{\boldsymbol{b}}}) : \overline{\underset{\sim}{\boldsymbol{L}}}^p + \left(\overline{a} - \overline{\rho}\frac{\partial\psi}{\partial\chi}\right)\dot{\chi} + \left(\overline{\underline{\boldsymbol{b}}} - \overline{\rho}\frac{\partial\overline{\psi}}{\partial\overline{\underline{\boldsymbol{K}}}}\right).\dot{\overline{\underline{\boldsymbol{K}}}} - \overline{\rho}\frac{\partial\overline{\psi}}{\partial\boldsymbol{\alpha}_I}\dot{\boldsymbol{\alpha}}_I \geq 0 \tag{28}$$

The state laws are adopted in a form such that no dissipation is associated to the generalized stress $\overline{\underline{\boldsymbol{b}}}$:

$$\underset{\sim}{\boldsymbol{\Pi}}^e = 2\overline{\rho}\frac{\partial\overline{\psi}}{\partial\underset{\sim}{\boldsymbol{C}}^e} \quad , \quad \overline{a} = \overline{\rho}\frac{\partial\overline{\psi}}{\partial\chi} \quad , \quad \overline{\underline{\boldsymbol{b}}} = \overline{\rho}\frac{\partial\overline{\psi}}{\partial\overline{\underline{\boldsymbol{K}}}} \quad , \quad \boldsymbol{A_I} = \overline{\rho}\frac{\partial\overline{\psi}}{\partial\boldsymbol{\alpha}_I} \tag{29}$$

The mechanical dissipation takes a specific form in that case:

$$\left(\underset{\sim}{\boldsymbol{M}} + \underset{\sim}{\boldsymbol{X}}^b\right) : \overline{\underset{\sim}{\boldsymbol{L}}}^p - \boldsymbol{A_I}\dot{\boldsymbol{\alpha}}_I \geq 0 \tag{30}$$

where

$$\underset{\sim}{\boldsymbol{X}}^b = \overline{\underline{\boldsymbol{K}}}\otimes\overline{\underline{\boldsymbol{b}}} \tag{31}$$

is an additional contribution to the Mandel stress tensor acting as a kinematic hardening variable that naturally emerges from the formulation w.r.t. the intermediate local configuration. The physical meaning of the quadratic gradient term in the energy is related to the development of geometrically necessary dislocations, as documented by many papers in the literature. In contrast, the contribution $\underset{\sim}{\boldsymbol{X}}^b$ according to Eq. (31) is a purely "geometrical" nonlinear contribution which arises when extending the usual small strain gradient contribution to finite deformations by means of a pull-back of the plastic strain gradient to the intermediate configuration. It is of second order compared to the first order gradient term and does not subsist in the infinitesimal case. It is a further consequence of plastic incompatibility and has never been pointed out prior to [44]. The geometrical interpretation is that plastic incompatibility results in a back-stress even when scalar-based gradient plasticity is considered. To our knowledge, there is no clear experimental evidence yet of the need for such a subtle term. This is an incentive for performing cyclic tests at large amplitudes and study the size dependence of the results.

A generalized dissipation potential can be introduced depending on the generalized Mandel stress tensor:

$$\overline{\underset{\sim}{\boldsymbol{L}}}^p = \frac{\partial\Omega}{\partial(\underset{\sim}{\boldsymbol{M}} + \underset{\sim}{\boldsymbol{X}}^b)} \quad , \quad \dot{\boldsymbol{\alpha}}_I = -\frac{\partial\Omega}{\partial\boldsymbol{A_I}} \tag{32}$$

The choice of a convex function $\Omega(\underset{\sim}{\boldsymbol{M}} + \underset{\sim}{\boldsymbol{X}}^b, \boldsymbol{A_I})$ ensures identical fulfillment of the positivity of the dissipation rate.

2.4 Model based on the cumulative plastic strain

The previous formulations are now illustrated in a simple elastoplastic case with the choice of the cumulative plastic strain p as a scalar internal variable controlling isotropic hardening, and of the tensor internal variable $\underset{\sim}{\boldsymbol{\alpha}} \in \{\boldsymbol{\alpha_I}\}$ accounting for kinematic hardening, as done in classical plasticity theory, see [63]. The micromorphic variable associated to cumulative plastic strain is denoted by p_χ ($\chi \equiv p_\chi$). The following quadratic form for the free energy potential is adopted

$$\psi_0(\underset{\sim}{\boldsymbol{C}}^e, p, \underset{\sim}{\boldsymbol{\alpha}}, p_\chi, \underline{\boldsymbol{K}}) = \psi^{ref}(\underset{\sim}{\boldsymbol{C}}^e, p, \underset{\sim}{\boldsymbol{\alpha}}) + \frac{H_\chi}{2\rho_0}(p - p_\chi)^2 + \frac{1}{2\rho_0}\underline{\boldsymbol{K}}\cdot\underset{\sim}{\boldsymbol{A}}\cdot\underline{\boldsymbol{K}} \tag{33}$$

where H_χ is a coupling modulus (MPa) and $\underset{\sim}{\boldsymbol{A}}$ is a second rank tensor of generalized moduli. For the sake of demonstration, the following expression of the classical specific free energy is adopted

$$\psi^{ref}(\underset{\sim}{\boldsymbol{C}}^e, p, \underset{\sim}{\boldsymbol{\alpha}}) = \frac{1}{2\overline{\rho}}\underset{\sim}{\boldsymbol{E}}^e : \underset{\approx}{\mathbb{C}} : \underset{\sim}{\boldsymbol{E}}^e + \psi^h(p, \underset{\sim}{\boldsymbol{\alpha}}) \tag{34}$$

where $\underset{\sim}{\boldsymbol{E}}^e = (\underset{\sim}{\boldsymbol{C}}^e - \underset{\sim}{\mathbf{1}})/2$ is the Green–Lagrange strain w.r.t. the intermediate configuration, $\underset{\approx}{\mathbb{C}}$ is the fourth-order tensor of elastic moduli and $\psi^h(p, \boldsymbol{\alpha}_I)$ is the stored energy contribution associated with work-hardening.

The state laws (27) become

$$\underset{\sim}{\boldsymbol{\Pi}}^e = \underset{\approx}{\mathbb{C}} : \underset{\sim}{\boldsymbol{E}}^e, \qquad a_0 = -H_\chi\,(p - p_\chi) \quad , \quad \underline{\boldsymbol{b}}_0 = \underset{\sim}{\boldsymbol{A}}.\underline{\boldsymbol{K}}, \qquad R(p) = \overline{\rho}\frac{\partial \psi_0}{\partial p} \tag{35}$$

The first equation is called the Saint-Venant-Kirchhoff hyperelasticity law w.r.t. the local intermediate configuration. The yield function is then taken of the form

$$f(\underset{\sim}{\boldsymbol{M}}, \underset{\sim}{\boldsymbol{X}}_m) = \left[\underset{\sim}{\boldsymbol{M}} - \underset{\sim}{\boldsymbol{X}}^{ref}\right]_{eq} - R_0 - R(p) \tag{36}$$

involving the Mandel stress tensor following [37]. The scalar function $[\diamond]_{eq}$ and the material constant R_0 denote the equivalent stress and the initial yield stress, respectively. The back-stress $\underset{\sim}{\boldsymbol{X}}^{ref}$ and the isotropic hardening R^{ref} are related to internal variables $\underset{\sim}{\boldsymbol{\alpha}}$ and p by

$$\underset{\sim}{\boldsymbol{X}}^{ref} = \overline{\rho}\frac{\partial \psi^{ref}}{\partial \underset{\sim}{\boldsymbol{\alpha}}}, \qquad R^{ref} = \overline{\rho}\frac{\partial \psi^{ref}}{\partial p} \tag{37}$$

Remark 1 The last equation (36) implies that the isotropic hardening variable can be written as

$$\begin{aligned} R(p) &= \overline{\rho}\frac{\partial \psi^{ref}}{\partial p} + \frac{\overline{\rho}}{\rho_0}H_\chi(p - p_\chi) \\ &= \overline{\rho}\frac{\partial \psi^{ref}}{\partial p} - a_0 = \overline{\rho}\frac{\partial \psi^{ref}}{\partial p} - \mathrm{Div}\,\underline{\boldsymbol{b}}_0 \\ &= R^{ref}(p) - A\Delta_0 p_\chi \end{aligned} \tag{38}$$

where plastic incompressibility condition and isotropic tensor $\underset{\sim}{\boldsymbol{A}}$ have been implemented. The constraint $p_\chi \equiv p$ can be enforced by adopting a sufficiently large value of the penalty modulus H_χ. The hardening law is then enhanced by a Laplace term and the model coincides accordingly with the Aifantis theory of strain gradient plasticity, see [66, 67].

By combining Eq. (11) and Eq. (35), the following regularization operator is derived

$$p = p_\chi - \frac{1}{H_\chi}\mathrm{Div}(\underset{\sim}{\boldsymbol{A}} \cdot \underline{\boldsymbol{K}}) \tag{39}$$

In the isotropic and homogeneous case, *i.e.* $\underset{\sim}{\boldsymbol{A}} = A\underset{\sim}{\mathbf{1}}$ and material parameter A independent of material point, Eq. (39) reduces to

$$p = p_\chi - \frac{A}{H_\chi}\Delta_0 p_\chi \tag{40}$$

which involves the Laplacian operator Δ_0 w.r.t. Lagrangian coordinates. The constitutive choices of specific free energy potential for different formulations are summarized in Table 1. For the sake of comparison, the regularization equations are all expressed in terms of Lagrangian operators.

	Eulerian	Lagrangian	intermediate
Specific free energy	$\psi = \psi^{ref} + \frac{1}{2\rho}\underline{\boldsymbol{k}}.\underset{\sim}{\boldsymbol{A}}.\underline{\boldsymbol{k}} + \frac{H_\chi}{2\rho}(p-p_\chi)^2$	$\psi_0 = \psi^{ref} + \frac{1}{2\rho_0}\underline{\boldsymbol{K}}.\underset{\sim}{\boldsymbol{A}}.\underline{\boldsymbol{K}} + \frac{H_\chi}{2\rho_0}(p-p_\chi)^2$	$\overline{\psi} = \psi^{ref} + \frac{1}{2\overline{\rho}}\overline{\underline{\boldsymbol{K}}}.\underset{\sim}{\boldsymbol{A}}.\overline{\underline{\boldsymbol{K}}} + \frac{H_\chi}{2\overline{\rho}}(p-p_\chi)^2$
Yield function f	$\left[\underset{\sim}{\boldsymbol{M}} - \underset{\sim}{\boldsymbol{X}}^{ref}\right]_{eq} - (R^{ref} - J_e a)$	$\left[\underset{\sim}{\boldsymbol{M}} - \underset{\sim}{\boldsymbol{X}}^{ref}\right]_{eq} - \left(R^{ref} - J_p^{-1} a_0\right)$	$\left[\underset{\sim}{\boldsymbol{M}} - \underset{\sim}{\boldsymbol{X}}^{ref} + \underset{\sim}{\boldsymbol{X}}^{b}\right]_{eq} - (R^{ref} - \overline{a})$
Generalized stresses	$a = -H_\chi\,(p-p_\chi)$ $\underline{\boldsymbol{b}} = \underset{\sim}{\boldsymbol{A}}.\underline{\boldsymbol{k}}$	$a_0 = -H_\chi\,(p-p_\chi)$ $\underline{\boldsymbol{b}}_0 = \underset{\sim}{\boldsymbol{A}}.\underline{\boldsymbol{K}}$	$\underset{\sim}{\boldsymbol{X}}^{b} = \overline{\underline{\boldsymbol{K}}} \otimes \overline{\underline{\boldsymbol{b}}}$ $\overline{a} = -H_\chi\,(p-p_\chi)$ $\overline{\underline{\boldsymbol{b}}} = \underset{\sim}{\boldsymbol{A}}.\overline{\underline{\boldsymbol{K}}}$
Regularization operator	$p = p_\chi - \frac{1}{H_\chi}\mathrm{Div}\left(J(\underset{\sim}{\boldsymbol{F}}^{-1}\underset{\sim}{\boldsymbol{A}}\underset{\sim}{\boldsymbol{F}}^{-T})\cdot\underline{\boldsymbol{K}}\right)$	$p = p_\chi - \frac{1}{H_\chi}\mathrm{Div}(\underset{\sim}{\boldsymbol{A}}\cdot\underline{\boldsymbol{K}})$	$p = p_\chi - \frac{1}{H_\chi}\mathrm{Div}\left(J_p(\underset{\sim}{\boldsymbol{F}}^{p-1}\underset{\sim}{\boldsymbol{A}}\underset{\sim}{\boldsymbol{F}}^{p-T})\cdot\underline{\boldsymbol{K}}\right)$

Table 1: A summary of constitutive choices and regularization operators for different formulations.

Remark 2 To illustrate the difference between the various formulations while assuming the same form of free energy potentials, let us derive a Lagrangian formulation from a formulation based on a quadratic potential ψ expressed in terms of Eulerian gradient $\underline{\boldsymbol{k}}$. In the isotropic case, the conversion (18) shows that a quadratic potential of Eulerian arguments results in a non-quadratic potential in terms of Lagrangian arguments. As shown in Table 1, the regularization operators provided by the three formulations are then different for a given form of free energy potential and the same material parameters.

2.5 Model based on the equivalent plastic strain

The model based on the cumulative plastic strain will be shown to lead to a size-dependent isotropic hardening. In contrast, an alternative scalar model has been proposed in [55], in the small strain framework, in order to model size-dependent kinematic hardening without using the full plastic strain tensor as done previously in [53] which is believed to be computationally expensive. Here, we present an extension of that model to finite strains by considering the norm of $(\underset{\sim}{\boldsymbol{B}}^p - \underset{\sim}{\boldsymbol{1}})$ where $\underset{\sim}{\boldsymbol{B}}^p = \underset{\sim}{\boldsymbol{F}}^p\underset{\sim}{\boldsymbol{F}}^{pT}$ is the plastic left Cauchy-Green tensor. Accordingly, the micromorphic variable is associated to the equivalent measure of plastic strain B^p_{eq} defined by

$$B^p_{eq} = \sqrt{\frac{1}{6}\left(\underset{\sim}{\boldsymbol{B}}^p - \underset{\sim}{\boldsymbol{1}}\right) : \left(\underset{\sim}{\boldsymbol{B}}^p - \underset{\sim}{\boldsymbol{1}}\right)} \tag{41}$$

In what follows, the derivation of constitutive equations and flow rules for a Lagrangian formulation are presented. Similarly, as shown in Sec. 2.1, other formulations are possible by considering gradients of micromorphic variables defined w.r.t. ~~to~~ Eulerian and intermediate configurations. The free energy potential per unit mass, assumed to be a function

$$\psi_0 = \psi_0(\underset{\sim}{\boldsymbol{C}}^e, \alpha_I, \underset{\sim}{\boldsymbol{B}}^p, \chi, \underline{\boldsymbol{K}}) \tag{42}$$

The Clausius-Duhem inequality becomes[2]

$$\left(\frac{J_p}{2}\underset{\sim}{\boldsymbol{\Pi}}^e - \rho_0\frac{\partial\psi_0}{\partial\underset{\sim}{\boldsymbol{C}}^e}\right) : \dot{\underset{\sim}{\boldsymbol{C}}}^e + \left(J_p\underset{\sim}{\boldsymbol{M}} - 2\rho_0\frac{\partial\psi_0}{\partial\underset{\sim}{\boldsymbol{B}}^p}\underset{\sim}{\boldsymbol{B}}^p\right) : \overline{\underset{\sim}{\boldsymbol{L}}}^p + \left(a_0 - \rho_0\frac{\partial\psi_0}{\partial\chi}\right)\dot{\chi} + \left(\underline{\boldsymbol{b}}_0 - \rho_0\frac{\partial\psi_0}{\partial\underline{\boldsymbol{K}}}\right).\dot{\underline{\boldsymbol{K}}} - \rho_0\frac{\partial\psi_0}{\partial\boldsymbol{\alpha}_I}\dot{\boldsymbol{\alpha}}_I \geq 0 \tag{43}$$

The state laws follow as

$$\underset{\sim}{\boldsymbol{\Pi}}^e = 2\overline{\rho}\frac{\partial\psi_0}{\partial\underset{\sim}{\boldsymbol{C}}^e}, \qquad a_0 = \rho_0\frac{\partial\psi_0}{\partial\chi}, \qquad \underline{\boldsymbol{b}}_0 = \rho_0\frac{\partial\psi_0}{\partial\underline{\boldsymbol{K}}}, \qquad \boldsymbol{A}_I = \overline{\rho}\frac{\partial\psi_0}{\partial\boldsymbol{\alpha}_I} \tag{44}$$

[2] It can be checked that

$$\frac{\partial\psi_0}{\partial\underset{\sim}{\boldsymbol{B}}^p} : \dot{\underset{\sim}{\boldsymbol{B}}}^p = \frac{\partial\psi_0}{\partial\underset{\sim}{\boldsymbol{B}}^p} : (\overline{\underset{\sim}{\boldsymbol{L}}}^p\underset{\sim}{\boldsymbol{B}}^p + \underset{\sim}{\boldsymbol{B}}^p\overline{\underset{\sim}{\boldsymbol{L}}}^{pT}) = 2\frac{\partial\psi_0}{\partial\underset{\sim}{\boldsymbol{B}}^p} : (\overline{\underset{\sim}{\boldsymbol{L}}}^p\underset{\sim}{\boldsymbol{B}}^p) = 2\left(\frac{\partial\psi_0}{\partial\underset{\sim}{\boldsymbol{B}}^p}\underset{\sim}{\boldsymbol{B}}^p\right) : \overline{\underset{\sim}{\boldsymbol{L}}}^p$$

assuming that $\partial\psi_0/\partial\underset{\sim}{\boldsymbol{B}}^p$ is symmetric.

The residual dissipation becomes

$$\left(J_p \underset{\sim}{\boldsymbol{M}} - 2\rho_0 \frac{\partial \psi_0}{\partial \underset{\sim}{\boldsymbol{B}}^p} \underset{\sim}{\boldsymbol{B}}^p\right) : \overline{\underset{\sim}{\boldsymbol{L}}}^p - \boldsymbol{A_I} \dot{\boldsymbol{\alpha}}_I \geq 0 \tag{45}$$

By assuming the existence of a convex yield function $f(\underset{\sim}{\boldsymbol{M}} - \underset{\sim}{\boldsymbol{X}}_m, \boldsymbol{A_I})$, the flow rule follows from the normality condition

$$\overline{\underset{\sim}{\boldsymbol{L}}}^p = \dot{p} \frac{\partial f}{\partial \left(\underset{\sim}{\boldsymbol{M}} - \underset{\sim}{\boldsymbol{X}}_m\right)} \tag{46}$$

where a back-stress arises given by

$$\underset{\sim}{\boldsymbol{X}}_m = 2\overline{\rho} \frac{\partial \psi_0}{\partial \underset{\sim}{\boldsymbol{B}}^p} \underset{\sim}{\boldsymbol{B}}^p \tag{47}$$

The particular choice of a partly quadratic potential as

$$\psi_0(\underset{\sim}{\boldsymbol{C}}^e, \underset{\sim}{\boldsymbol{B}}^p, p, \chi, \underline{\boldsymbol{K}}) = \psi^{ref} + \frac{H_\chi}{2\rho_0}(B^p_{eq} - \chi)^2 + \frac{1}{2\rho_0} \underline{\boldsymbol{K}}.\underset{\sim}{\boldsymbol{A}}.\underline{\boldsymbol{K}} \tag{48}$$

leads to the following constitutive equations

$$\underset{\sim}{\boldsymbol{\Pi}}^e = \mathbb{C} : \underset{\sim}{\boldsymbol{E}}^e, \qquad R(p) = \overline{\rho} \frac{\partial \psi_0}{\partial p}, \qquad a_0 = -H_\chi(B^p_{eq} - \chi), \qquad \underline{\boldsymbol{b}}_0 = \underset{\sim}{\boldsymbol{A}}\underline{\boldsymbol{K}} \tag{49}$$

and

$$\underset{\sim}{\boldsymbol{X}}_m = \frac{H_\chi}{3J_p} \frac{\left(\underset{\sim}{\boldsymbol{B}}^p - \underset{\sim}{\boldsymbol{1}}\right) \underset{\sim}{\boldsymbol{B}}^p}{B^p_{eq}} (B^p_{eq} - \chi) \tag{50}$$

The proposed yield function is given by

$$f(\underset{\sim}{\boldsymbol{M}}, \underset{\sim}{\boldsymbol{X}}_m) = \left[\underset{\sim}{\boldsymbol{M}} - \underset{\sim}{\boldsymbol{X}}_m\right]_{eq} - R_0 - R(p) \tag{51}$$

The size-dependent character of the enhanced kinematic hardening component $\underset{\sim}{\boldsymbol{X}}_m$ is apparent in Eq. (50) by noting that the term $H_\chi(B^p_{eq} - \chi) = -a_0 = -\text{Div}\, \underline{\boldsymbol{b}}_0$ thus involving higher order derivatives.

2.6 Implementation scheme

The generic implementation of constitutive and balance laws of scalar micromorphic models is briefly described in this section. The present approach is implemented in the Finite Element code Zset [68] and follows the programming concepts from [69, 70].

The principle of virtual power in Eq. (10) is discretized as

$$\sum_{e=1}^{n} \int_{D_0^e} \mathcal{P}^{(i)} dV = \sum_{e=1}^{n_s} \int_{\partial D_0^e} \left(\underline{\boldsymbol{t}}.\dot{\underline{\boldsymbol{u}}} + a^c \dot{\chi}\right) dS \quad , \quad \forall D_0 \subset \Omega_0 \tag{52}$$

Here, the sub-domain D_0^e corresponds to the space occupied by the individual element e. The boundary ∂D_0 is discretized into n_s surface elements ∂D_0^e for the application of surface tractions. Within each individual element, u_i is interpolated from the displacement values of m nodes and χ from the values of q nodes as

$$u_i = \sum_{k=1}^{m} {}^{u}N^k \tilde{u}_i^k, \qquad \chi = \sum_{k=1}^{q} {}^{\chi}N^k \tilde{\chi}^k \tag{53}$$

360 ${}^{u}N^{k}$ and ${}^{\chi}N^{k}$ are shape functions for u_i and χ, respectively. The deformation gradient $\underset{\sim}{\boldsymbol{F}}$ and the Lagrangian gradient of χ denoted by $\underline{\boldsymbol{K}}$ are given by

$$F_{ij} - \delta_{ij} = \sum_{k=1}^{m} {}^{u}B_j^k \tilde{u}_i^k, \qquad K_i = \sum_{k=1}^{q} {}^{\chi}B_i^k \tilde{\chi}^k \tag{54}$$

with ${}^{u}B_j^k = \dfrac{\partial {}^{u}N^k}{\partial X_j}$ and ${}^{u}B_i^k = \dfrac{\partial {}^{\chi}N^k}{\partial X_i}$. Finally, by substituting equations (53) and (54) into Eq. (52), one gets

$$\begin{aligned} &\sum_{e=1}^{n}\sum_{k=1}^{m}\left[\int_{D_0^e}(P_{ij}\,{}^{u}B_j^k)dV_0\right]\dot{\tilde{u}}_i^k + \sum_{e=1}^{n}\sum_{k=1}^{q}\left[\int_{D_0^e}(a_0\,{}^{\chi}N^k + \underline{\boldsymbol{b}}\,{}^{\chi}B_i^k)dV_0\right]\dot{\tilde{\chi}}^k \\ &= \sum_{e=1}^{n_s}\sum_{k=1}^{m}\left[\int_{\partial D_0^e}\left(t_{0,i}\,{}^{u}N^k\right)dS_0\right]\dot{\tilde{u}}_i^k + \sum_{e=1}^{n_s}\sum_{k=1}^{q}\left[\int_{\partial D_0^e}\left(a_0^c\,{}^{\chi}N^k\right)dS_0\right]\dot{\tilde{\chi}}^k \end{aligned} \tag{55}$$

According to Eq. (55), an internal (resp. external) reaction is associated with each degree of freedom. The FE problem will be solved by a monolithic iterative method, using a Newton algorithm. The consistent tangent matrix as shown in [23, 25] is given

$$[\boldsymbol{K}] = \frac{\partial \Delta\mathcal{V}_{OUT}}{\partial \Delta\mathcal{V}_{IN}} - \frac{\partial \Delta\mathcal{V}_{OUT}}{\partial \Delta\mathcal{V}_{int}}\left(\frac{\partial \mathcal{R}}{\partial \Delta\mathcal{V}_{int}}\right)^{-1}\frac{\partial \mathcal{R}}{\partial \Delta\mathcal{V}_{IN}} \tag{56}$$

365 where $\mathcal{V}_{OUT}$, $\mathcal{V}_{IN}$ and $\mathcal{V}_{int}$ denote output, input and integrated variables, respectively. The output variables are the ~~Piola~~ Boussinesq stress $\underset{\sim}{\boldsymbol{P}}$ and generalized stresses a and $\underline{\boldsymbol{b}}$. The input variables are $\underset{\sim}{\boldsymbol{F}}$, χ, $\underline{\boldsymbol{K}}$. For the sake of demonstration, we consider $\underset{\sim}{\boldsymbol{F}}^e$ and the cumulative plastic strain p as integrated variables. Additional internal variables related to isotropic/kinematic hardening are readily incorporated in this framework.
The residuals $\mathcal{R}(\Delta\mathcal{V}_{int}, \Delta\mathcal{V}_{IN})$ for the evolution equation for $\underset{\sim}{\boldsymbol{F}}^e$ and the yield conditions, are given by

$$\begin{cases} \mathcal{R}_e = & \Delta\underset{\sim}{\boldsymbol{F}}^e - \underset{\sim}{\boldsymbol{L}}\underset{\sim}{\boldsymbol{F}}^e + \Delta p\,\underset{\sim}{\boldsymbol{F}}^e\dfrac{\partial f}{\partial \underset{\sim}{\boldsymbol{M}}} = 0 \\ \mathcal{R}_p = & \dfrac{f}{H_\chi} = 0 \quad \text{(plastic)}, \quad \text{or} \quad \mathcal{R}_p = \Delta p - \Delta t\dfrac{\partial \Omega}{\partial f} = 0 \quad \text{(viscoplastic)} \end{cases} \tag{57}$$

370 where $\underset{\sim}{\boldsymbol{L}}$ is the velocity gradient. Supplementary equations can be added in order to integrate internal variables (*e.g.* associated to isotropic and kinematic hardening). In order to satisfy the plastic incompressibility condition ($\det\left(\underset{\sim}{\boldsymbol{F}}^p\right) = 1$), $\underset{\sim}{\boldsymbol{F}}^e$ is replaced in Eq. (57) by $\left(\dfrac{\det\left(\underset{\sim}{\boldsymbol{F}}\right)}{\det\left(\underset{\sim}{\boldsymbol{F}}^e\right)}\right)^{1/3}\underset{\sim}{\boldsymbol{F}}^e$. The normalization of $\mathcal{R}_p$ by H_χ parameter is carried out to improve the numerical efficiency by avoiding ill-conditioned Jacobian matrices $\mathcal{J} = \dfrac{\partial \mathcal{R}}{\partial \Delta\mathcal{V}_{int}}$, especially
375 in case of rate-independent plasticity. The calculation of the tangent matrix $[\boldsymbol{K}]$ is detailed in Appendix A.

2.7 Limit case of Aifantis plasticity

Following the Remark 1, we present here an implementation of Aifantis strain gradient plasticity relying upon Lagrange multipliers added to the micromorphic model. This method
380 has been applied for plasticity and damage models [25, 52, 59]. A Lagrange multiplier is

introduced to enforce the internal constraint $p_\chi \equiv p$ at each material point. The enhanced free energy potential, interpreted as a Lagrangian function, is given by

$$\psi_0^{\mathcal{L}}(\underset{\sim}{\boldsymbol{C}}^e, p, p_\chi, \underline{\boldsymbol{K}}) = \psi^{ref}(\underset{\sim}{\boldsymbol{C}}^e, p) + \frac{1}{2\rho}\underline{\boldsymbol{K}}.\underset{\sim}{\boldsymbol{A}}.\underline{\boldsymbol{K}} + \frac{\lambda}{\rho_0}(p_\chi - p) + \frac{\mu_\chi}{2\rho_0}(p_\chi - p)^2 \tag{58}$$

where λ is a Lagrange multiplier and μ_χ is a penalization modulus. The Lagrange multiplier λ is introduced to weakly enforce the equality between p_χ and p. The augmented Lagrangian term $\mu_\chi(p_\chi - p)^2$ provides an additional coercivity so as to avoid potential oscillation of the cumulative plasticity (see *e.g.* [25, 59]). By substituting Eq. (58) in the Clausius–Duhem inequality and assuming that a_0 and $\underline{\boldsymbol{b}}_0$ are non-dissipative generalized stresses, the following constitutive laws are obtained:

$$\underset{\sim}{\boldsymbol{\Pi}}^e = 2\frac{\partial \psi}{\partial \underset{\sim}{\boldsymbol{C}}^e}, \qquad a_0 = \rho_0 \frac{\partial \psi}{\partial \chi}, \qquad \underline{\boldsymbol{b}}_0 = \rho_0 \frac{\partial \psi}{\partial \underline{\boldsymbol{K}}} \tag{59}$$

When the constraint $p \equiv p_\chi$ is met, one has

$$\frac{\partial \psi_0^{\mathcal{L}}}{\partial \lambda}\dot{\lambda} = \frac{\dot{\lambda}}{\rho_0}(p_\chi - p) = 0 \tag{60}$$

Similarly, formulations w.r.t. Eulerian and intermediate configurations are readily developed. The numerical implementation of this approach is detailed thoroughly in [25] for the Lagrangian case.

3 Size effects in confined plasticity

In the following, the ability of the present approach to model size effects is illustrated by several examples. For convenience, only the model presented in 2.4 based on cumulative plastic strain is considered in this section. Confined plasticity conditions are applied to a unit cell in order to induce high plastic strain gradients. Monotonic and cyclic loading conditions are applied in order to compare the three finite strain formulations previously discussed. Throughout the rest of the document, the material parameters for isotropic elasticity are: Young's modulus $E = 78$ GPa and the Poisson ratio $\nu = 0.3$. The plasticity related coefficients and the higher order parameters H_χ (unit MPa) and A (unit N) are varied.

3.1 Confined plasticity under shear loading

A strip of width $2h$ is considered in Fig. 1a. A macroscopic shear deformation $\overline{\underset{\sim}{\boldsymbol{F}}} = \underset{\sim}{\mathbf{1}} + \overline{F}_{12}\underline{\boldsymbol{e}}_x \otimes \underline{\boldsymbol{e}}_y$ is applied such that the displacement field takes the form

$$\underline{\boldsymbol{u}} = (\overline{\underset{\sim}{\boldsymbol{F}}} - \underset{\sim}{\mathbf{1}}) \cdot \underline{\boldsymbol{X}} + \underline{\boldsymbol{v}}(\underline{\boldsymbol{X}}) \tag{61}$$

Periodic boundary conditions are imposed on the displacement fluctuation $\underline{\boldsymbol{v}}$. Dirichlet conditions for the micromorphic variable are prescribed: $p_\chi = 0$ at $x = \pm h$. Periodicity conditions are enforced between top and bottom surfaces for p_χ. As a consequence, the fields are invariant along $\underline{\boldsymbol{e}}_y$, except the linear distribution $u_x(y)$.

A time-independent von Mises plasticity model is considered. The hardening free energy $\overline{\rho}\psi^h(p) = \frac{1}{2}Hp^2$ corresponding to linear hardening/softening leads to the following yield function for classical models

$$f(\underset{\sim}{\boldsymbol{M}}) = \sqrt{\frac{3}{2}\underset{\sim}{\boldsymbol{M}}' : \underset{\sim}{\boldsymbol{M}}'} - (R_0 + Hp) \tag{62}$$

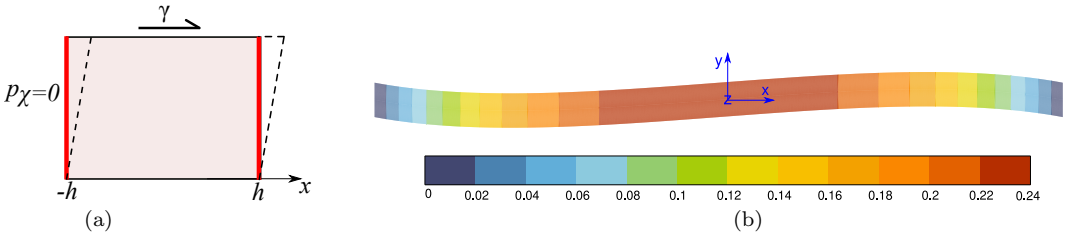

Fig. 1: (a) Simple glide test with imposed microplastic boundary conditions; (b) deformed shape and distribution of microplastic strain p_χ for $\overline{F}_{12} = 1$, $R_0 = 20$ MPa, $H = 0$ (Lagrangian formulation).

where $\underset{\sim}{\boldsymbol{M}}'$ is the deviatoric part of $\underset{\sim}{\boldsymbol{M}}$. The hardening law is modified in the micromorphic model such that the enhanced yield function becomes

$$f(\underset{\sim}{\boldsymbol{M}}) = \sqrt{\frac{3}{2}\underset{\sim}{\boldsymbol{M}}' : \underset{\sim}{\boldsymbol{M}}'} - (R_0 + R) \quad \text{with} \quad R = Hp + H_\chi(p - p_\chi) \tag{63}$$

where H is the plastic hardening modulus. Analytic solutions of this one-dimensional boundary value problem can be derived in the small strain limit. They are provided in Appendix B for $H \geq 0$. An important relation is derived therein, namely the characteristic length $1/\omega$ given by Eq. (98) which emerges from the analysis as a function of hardening modulus H and generalized moduli H_χ and A. The deformed shape and the microdeformation fields are illustrated by Fig. 1b. The latter profiles are also visible in Fig. 2a. The analytical solution predicts parabolic shapes for $H = 0$, at small strain, but more complex distributions are found at large deformations.

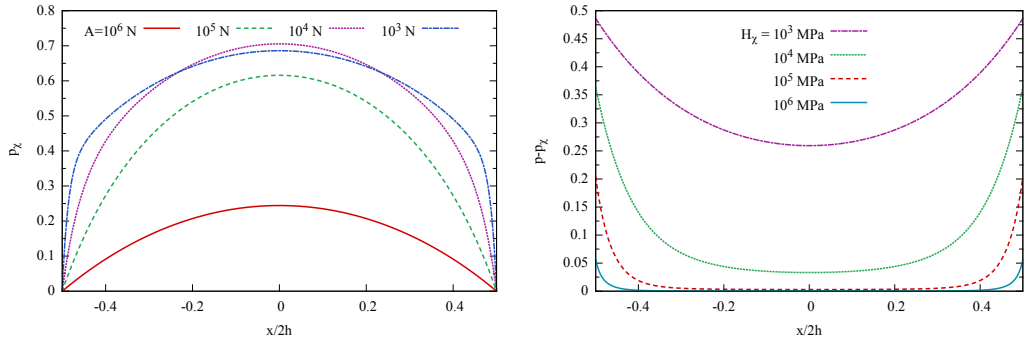

Fig. 2: (a) The profile of microplastic variable p_χ for different values of A ($H_\chi = 10^5$ MPa); (b) the difference $(p - p_\chi)$ for different values of H_χ ($A = 10^4$ N). The applied macroscopic strain is $\overline{F}_{12} = 1$, $R_0 = 20$ MPa, $H = 0$ (Lagrangian formulation).

As shown in Fig. 2b ($H = 0$), by increasing the value of the parameter H_χ, the difference between p and p_χ becomes smaller at a fixed value of higher order modulus A. Meanwhile, the generalized stress $a_0 = -H_\chi(p - p_\chi)$ increases with H_χ. It means that, enforcing equality between p and p_χ induces a very high yield stress in the vicinity of $x = \pm h$ given by

$$\sigma_Y = R_0 + R = R_0 + H_\chi(p - p_\chi) \tag{64}$$

The analytical solution for $H \geq 0$, detailed in Appendix B in the small strain framework, predicts that the profile of cumulative plastic plasticity is given by a hyperbolic (exponential) function. Fig. 3 shows such profiles of microplastic variable p_χ for several values of the parameter A. These curves can be shown to agree well with the predicted profiles at small strains but more complex distributions are found at large shear amounts. Fig. 4a depicts

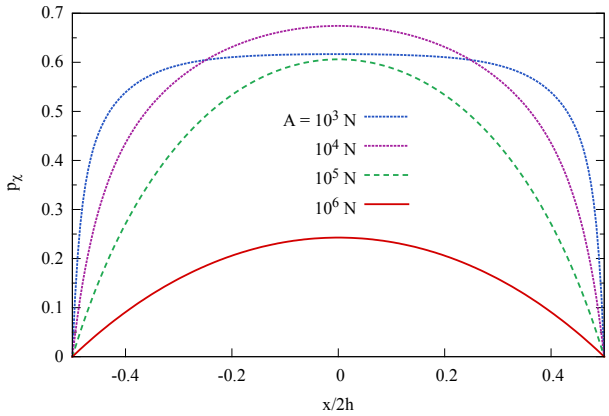

Fig. 3: The profile of microplastic variable p_χ for different values of A ($H_\chi = 10^5$ MPa). The applied macroscopic strain is $\overline{F}_{12} = 1$, $R_0 = 20$ MPa, $H = 1000$ MPa (Lagrangian formulation).

the stress-strain curves for different values of the parameter A in the absence of classical hardening ($H = 0$). A progressive stiffening is observed when increasing the value of parameter A or, equivalently, the intrinsic length scale. The same phenomenon is observed when the size of the unit cell gets smaller for a fixed value of A according to Fig. 4b. This leads to significant stiffening of the overall response when increasing the higher modulus A or, equivalently reducing the strip width. This corresponds to the well-known effect: *smaller is harder*. This is directly related to the fact that gradients of plastic variables are higher at small scales for the same loading conditions.

Some comments are due regarding the physical relevance of fixing the micromorphic variable $p_\chi = 0$ at some boundaries. Prescribing p_χ at a boundary is equivalent to imposing p if H_χ is sufficiently large and corresponds to a condition of surface passivation and the blockage of dislocations [71, 72]. For intermediate values of H_χ, the interpretation of p_χ remains open. However the contribution $(p-p_\chi)^2$ in the free energy density can be interpreted as a variance of spatial distribution of plastic strain inside the volume element, in the spirit of the recent article [73]. Another interpretation is possible based on homogenization arguments as proposed by [74]. These tracks remain to be explored in the future to better interpret the physical content of the micromorphic variable.

The results of a cyclic simple glide loading, with similar boundary conditions as in Fig. 1a, are provided in Fig. 5a for different finite deformation formulations. In this cyclic test, strain values remain moderate so that the differences between Eulerian and Lagrangian formulations are negligible. Meanwhile, a kinematic hardening effect is induced by the formulation w.r.t. the intermediate configuration. Over cycles, the gradient of microplastic variable p_χ increases, so that $\underset{\sim}{\boldsymbol{X}}^b$, given by Eq. (31), increases as well. It turns out that the sign of $\underset{\sim}{\boldsymbol{X}}^b$ components remains the same while shearing in both directions. The kinematic hardening $\underset{\sim}{\boldsymbol{X}}^b$ becomes more significant after few cycles. Nevertheless, the effect of the finite deformation formulation remains rather limited for the components σ_{12} and X^b_{12}. The effect is much more pronounced for the components σ_{11}, σ_{22} and σ_{33} which are not negligible due to the

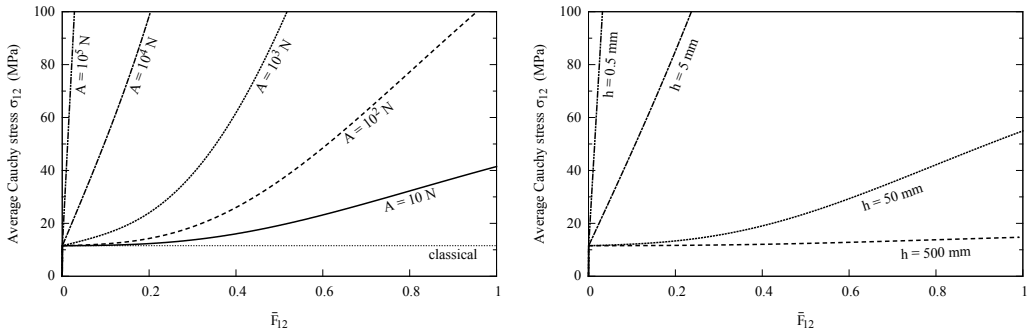

Fig. 4: The macroscopic stress-strain curves for different values of (a) the parameter A, $h = 5$ mm; (b) length of the unit cell h, $A = 10^4$ N. Material parameters: $R_0 = 20$ MPa, $H = 0$ and $H_\chi = 10^5$ MPa (Lagrangian formulation).

Poynting effect, see Fig. 5b. The reason is that X^b_{11} is the component having the highest value.

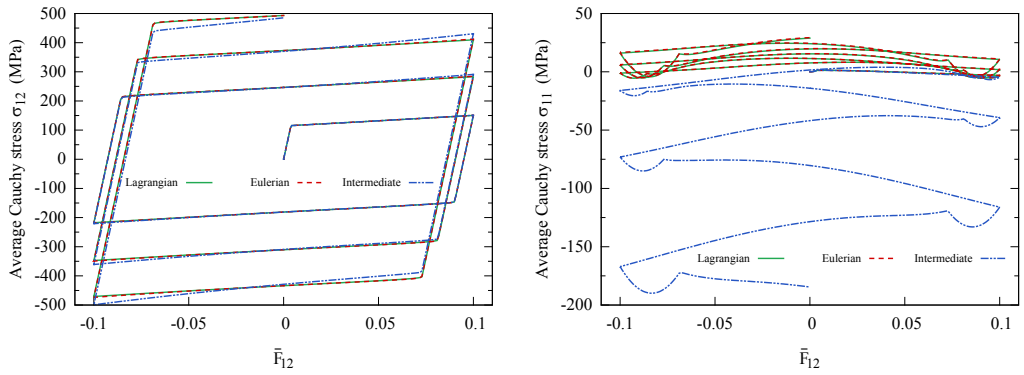

Fig. 5: Cyclic simple glide test with confined plasticity for different finite strain formulations. Material parameters: $R_0 = 200$ MPa, $H = 0$ MPa, $H_\chi = 10^4$ MPa, $A = 10^4$ N.

3.2 Confined plasticity under tensile loading

A simple tension test is considered with confined plasticity boundary conditions (passivation). The unit cell of width $2h$ is subjected to a uniform displacement u_x at $x = h$, u_y being constrained to be uniform at the top and bottom lines, see insert in Fig. 6a. The microplastic variable p_χ is set to zero at $x = \pm h$. Fig. 6a depicts the stress-strain curves for several values of material parameter A and several sizes of unit cell h. It shows that the induced isotropic hardening increases with higher values of the ratio A/h.

The stress-strain curves for a cyclic loading (tension+compression) are shown in Fig. 7a for the three finite deformation formulations. Small differences are noticed between Lagrangian and Eulerian formulations. In contrast, the formulation w.r.t. the intermediate configuration differs significantly from the two others. Note that the stress response drifts

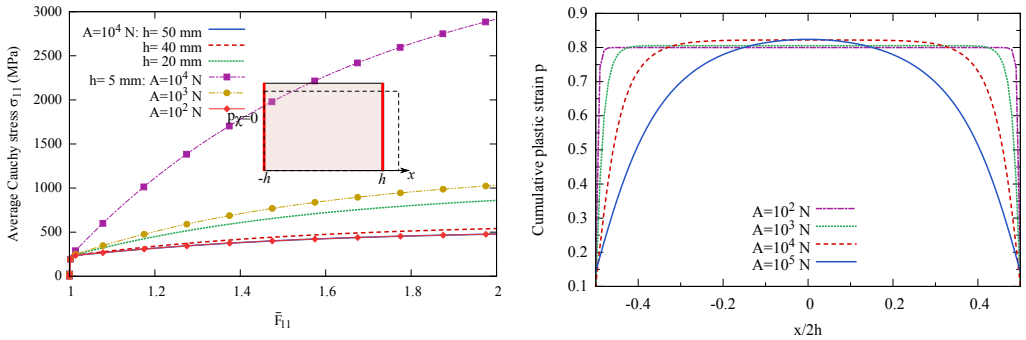

(a) (b)

Fig. 6: Monotonic tensile loading: (a) overall stress-strain curves; (b) profiles of cumulative plastic strain p for $\overline{F}_{11} = 2$. Material parameters are $H_\chi = 10^5$ MPa, $R_0 = 200$ MPa, $H = 0$ (Lagrangian formulation).

away towards negative values. This is due to kinematic hardening contribution by $\underset{\sim}{\boldsymbol{X}}^b$ having the same sign in tension (points 1 and 2 on the curves) and compression (point 1' and 2'). The gradient of cumulative plastic strain increases over cycles, so does $\underset{\sim}{\boldsymbol{X}}^b$ (see results for X^b_{11} component in Fig. 7b). In fact, the quantity $\underset{\sim}{\boldsymbol{X}}^b$ grows proportionally to the square of $\overline{\boldsymbol{K}}$ components according to Eq. (31). This indicates that this back-stress is a second order contribution at small strains but becomes dominant at large strains.

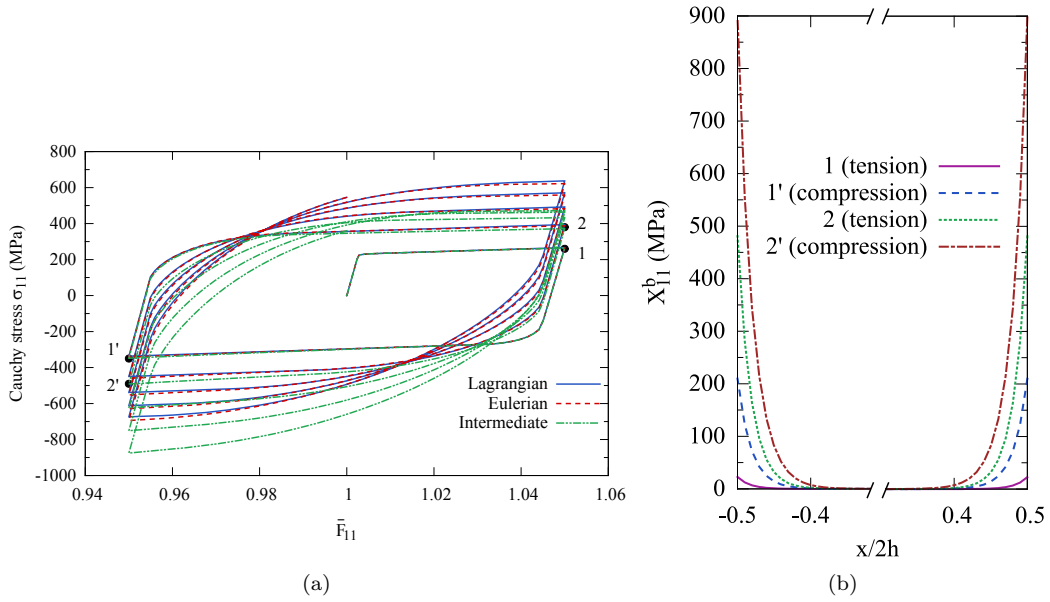

(a) (b)

Fig. 7: Cyclic tensile loading with confined plasticity: (a) Comparison of stress-strain curves for different finite strain formulations; (b) evolution of back-stress X^b_{11}. Material parameters: $H_\chi = 10^5$ MPa, $A = 10000$ N, $R_0 = 200$ MPa, $H = 0$. Unit cell length $h = 5$ mm.

4 Size effects in bending and torsion

At this stage, the scale effect was studied in cases where plastic strain gradients are caused by applying particular boundary conditions (confined plasticity). In this section, another type of loading conditions naturally inducing plastic strain gradients is addressed. Bending and torsion loadings were investigated thoroughly in the past to point out size effects in the plasticity of metals, as discussed in [3]. They represent crucial benchmark tests to analyze the pros and the cons of various gradient approaches. In the following, the bending of a two-dimensional foil and the torsion of a cylinder are investigated at finite strains.

4.1 Bending

The problem of thin foil bending is widely studied in the computational mechanics literature in the small strain framework [53, 55, 75]. As pointed out by these authors, the cumulative plastic strain is shown to be non smooth at the neutral axis when plasticity has invaded the whole beam. The fact that the cumulative plastic strain distribution is not differentiable on the neutral axis is challenging for most strain gradient plasticity algorithms. This difficulty can be overcome using the micromorphic approach since the plastic strain is not required to be smooth. On the other hand, the micromorphic model relying on the cumulative plastic strain was shown in [53] to induce spurious negative yield stress.

The present section aims to investigate this bending problem at finite strain. The plane-strain bending of a 2D-foil of width $2w$, around z-axis is considered. Due to mirror symmetry about $y-$axis, only the right half of the foil is simulated. Four-point bending is applied to the sample, as shown in Fig. 8. The curvature is approximately given by $\kappa = (F_{11}(x = 0, y = w) - 1)/w$ which will be used as loading parameter in the analysis. The material is assumed to be perfectly plastic ($H = 0$ MPa in Eq. (63)). The micromorphic formulation given in Sec. 2.4 where $\chi \equiv p$ is adopted. The FE mesh is made of 3232 P2P1 elements (quadratic for displacement and linear for the micromorphic variable) with reduced integration (C2D8R) and 9963 nodes.

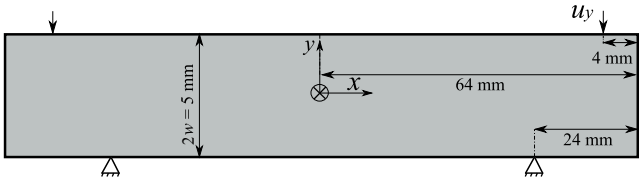

Fig. 8: Schematic of two-dimensional foil subjected to four points bending.

The distribution of cumulative plastic strain is shown in Fig. 9. The profiles of p and p_χ are plotted for two different values of parameter A in Fig. 10a. Contrary to small strain case, the profile of cumulative plastic strain is not symmetric, due to tension-compression asymmetry at finite deformations. Due to nonlinear geometric effects, the neutral axis is shifted. Besides, one can notice that the distribution of cumulative plastic strain p is not smooth in the vicinity of the neutral axis for small values of A. This is in contrast to the microdeformation p_χ distribution exhibiting a horizontal tangent at the neutral axis where p vanishes and p_χ is finite. A gap between p and p_χ occurs around $y = \pm w$ and at the neutral axis. The generalized stress $\underline{\boldsymbol{b}}_0$ vanishes at $y = \pm w$, so does the gradient $\underline{\boldsymbol{K}}$ (see Fig. 10b). As a consequence, the curve of p_χ displays horizontal tangents at $y = \pm w$. By increasing A, the gap between p and p_χ becomes larger. The negative contribution of $(p-p_\chi)$ in the vicinity of the neutral axis leads to a decrease of the radius of the yield surface (see

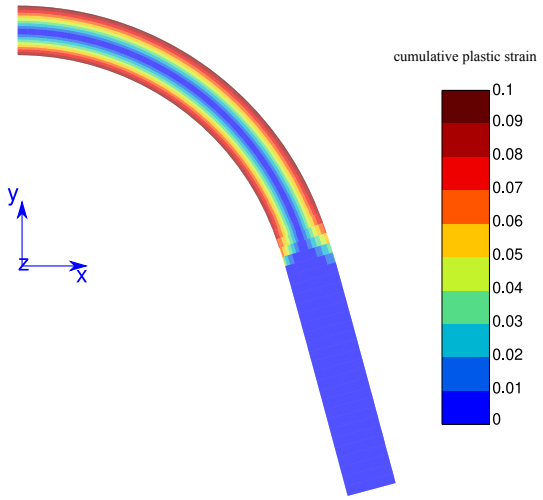

Fig. 9: The contour of cumulative plastic strain in the foil. Material parameters $R_0 = 100$ MPa, $H = 0$, $H_\chi = 10^4$ MPa, $A = 500$ N. Applied curvature $\kappa = 0.0348$ mm^{-1}.

Fig. 11a). As the parameter A (or H_χ) increases, this negative term becomes stronger. To satisfy consistency conditions, the radius of the yield surface must remain positive. Beyond a certain stage of deformation, $H_\chi(p - p_\chi)$ tends to become smaller than $-R_0$, which leads to a negative radius σ_Y. Since the equivalent von Mises stress is positive as well, the condition $f = 0$ cannot be satisfied when σ_Y is negative and the numerical simulation will diverge accordingly. It is the case for $A = 2000$ N in Fig.11b in which the simulation diverges at a curvature of 0.024 mm^{-1}. In the work [53], a negative yield radius is mentioned. This is due the fact that the provided analytical solution does not satisfy the consistency condition. Note also that considering a viscoplastic model will delay to some extent the occurrence of the aforementioned issue due to the overstress. Further discussion about this limitation is postponed to Sec. 6.4.

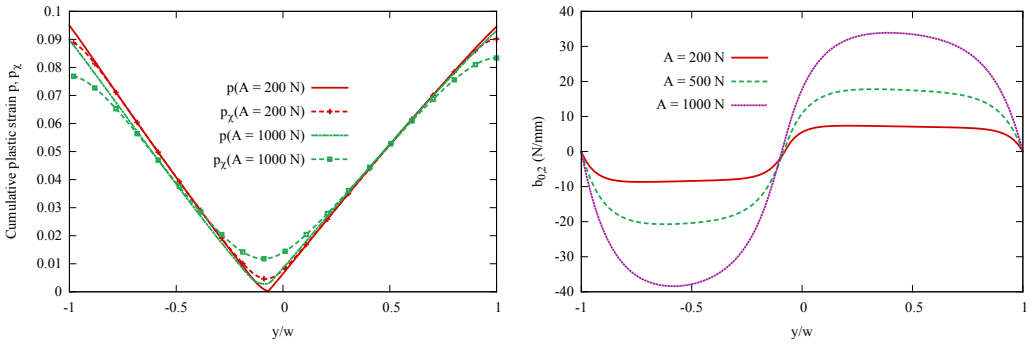

(a) (b)

Fig. 10: (a) Cumulative plastic strain and associated micromorphic variable along the cross section at $x = 0$; (b) the generalized stress component $b_{0,2}$ along the cross-section at $x = 0$. Material parameters: $R_0 = 100$ MPa, $H_\chi = 10^4$ MPa, $H = 0$. Applied curvature $\kappa = 0.0348$ mm^{-1}.

The curves of bending moment w.r.t. current coordinates vs. curvature are depicted in Fig. 11b. A size-dependent hardening effect can be observed while increasing the parameter A. A comparison between formulations w.r.t. Eulerian, Lagrangian and intermediate configurations (see Table 1) has been carried out. Accordingly, no significant differences was noticed between the various formulations. This is due mainly to the fact that the applied loading does not induce sufficiently large values of plastic strain to reveal potential deviation. Note that when the plastic strain becomes higher, its gradient increases as well leading to a negative yield radius σ_Y and accordingly the simulation does not converge. That holds true for both monotonic and cyclic loadings.

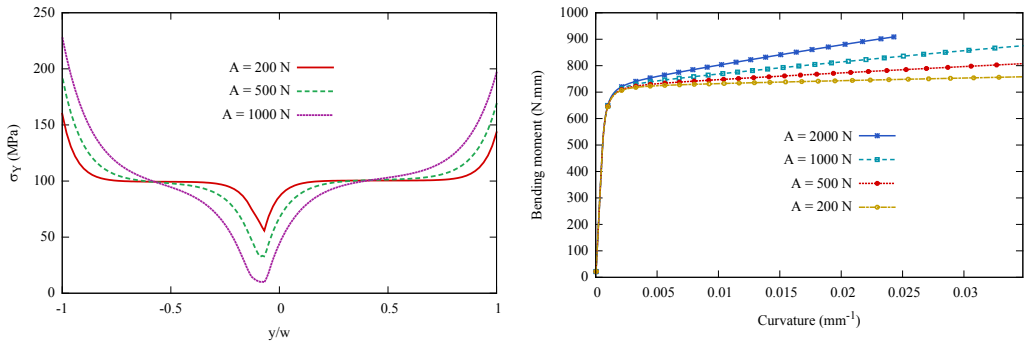

(a) (b)

Fig. 11: (a) The radius of yield surface $\sigma_Y = R_0 + H_\chi(p - p_\chi)$ captured at $\kappa = 0.0348$ mm^{-1}; (b) the bending moment-curvature curve. Material parameters: $H_\chi = 10^4$ MPa, $R_0 = 100$ MPa, $H = 0$.

4.2 Torsion

The torsion of a bar with circular cross-section of diameter $d = 2r$ and length L is considered, see Fig. 12a for the FE mesh and the dimensions used. The cylinder is twisted along z-axis by applying a rotation angle θ on the top surface ($z = L$) and fixing the bottom surface ($z = 0$). The lateral faces are kept traction free. Studies carried out in literature, particularly on single crystal plasticity [76] have shown the existence of plastic gradients along the outer circumference in addition to radial gradients due to the anisotropic activation of slip systems. In the present application, a von Mises time-independent perfectly plastic model is adopted as in Eq. (62). Accordingly, only radial plastic gradients are present, see Fig. 12b. Size-dependent torsion of cylinders has been simulated recently using Cosserat isotropic plasticity in [77] and using strain gradient crystal plasticity in [78]. The torsion test is used here as a benchmark for 3D finite element simulations at large strains.

The fields of cumulative plastic strain in Fig. 13a are found to be similar to the ones obtained in bending case, except that no asymmetry is observed. The cumulative plastic strain is not smooth along the cylinder axis in contrast to p_χ which does not vanish at the center and displays a horizontal tangent at the center and near the circumference. The difference $(p - p_\chi)$ is negative in the middle of the cylinder. As this term decreases, the cylinder's core undergoes a softening. In contrast, the outer region is subjected to hardening since p is larger than p_χ. The resulting size effect is shown by the torque-twist curves of Fig. 13b. The model induces a size-dependent isotropic hardening/softening given by $A\Delta_0 p_\chi$. Again, divergence occurs when the yield stress $\sigma_Y = R_0 + R$ vanishes.

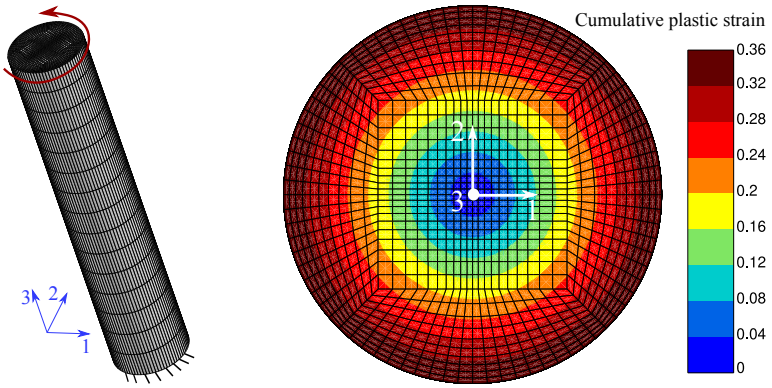

(a) (b)

Fig. 12: Torsion of a circular bar: (a) geometry and boundary conditions. The mesh contains 77511 nodes; $r = 1$ mm and $L = 10$ mm; (b) cumulative plastic strain contours obtained for $r\theta/L = 0.628$ ($\theta = 2\pi$).

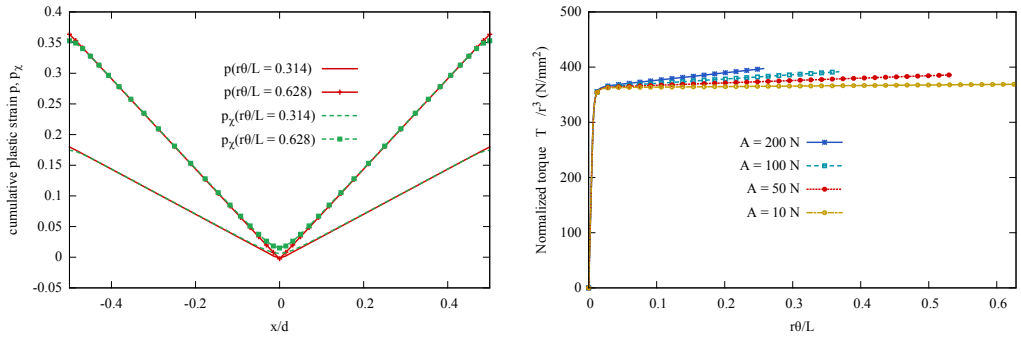

(a) (b)

Fig. 13: Torsion test: (a) Profiles of cumulative plastic strain and microplastic variable for $H_\chi = 10^4$ MPa, $A = 10$ N; (b) the normalized torque (w.r.t deformed configuration) vs. surface strain curves.

5 Regularization of strain localization behavior

The micromorphic model used for the modeling of size effects in hardening materials can also be used for the regularization of spurious mesh-dependence in the simulation of plastic strain localization phenomena for softening materials. Two benchmarks are considered for that purpose. The first case is the simulation of one-dimensional shear banding, for which an analytical solution can be worked out for the micromorphic model at small strains. The second case deals with a two-dimensional plate undergoing anisotropic shear banding. The attention is focused on finite strain effects on plastic strain localization which has rarely been tackled in the literature.

5.1 One-dimensional shear banding

A macroscopic shear deformation $\overline{\underset{\sim}{\boldsymbol{F}}} = \underset{\sim}{\mathbf{1}} + \overline{F}_{12}\, \underline{\boldsymbol{e}}_x \otimes \underline{\boldsymbol{e}}_y$ is applied to a strip of width $2h$. The displacement field is given by $\underline{\boldsymbol{u}} = (\overline{\underset{\sim}{\boldsymbol{F}}} - \underset{\sim}{\mathbf{1}}) \cdot \underline{\boldsymbol{X}} + \underline{\boldsymbol{v}}(\underline{\boldsymbol{X}})$. Periodic boundary conditions are imposed on the displacement fluctuation $\underline{\boldsymbol{v}}$ and the microplastic variable p_χ. A defect is

introduced in the middle of the strip (one element with an initial yield stress of $\approx 0.99\ R_0$) in order to trigger strain localization at a precise location. Fig. 14 shows the development of the shear localizing zone in the strip, see also Fig. 28 from Appendix B.3. A new complete analytical solution for a linear softening model ($H < 0$ in Eq. (63)) for the micromorphic model at small strains is derived and detailed in B.3. The following intrinsic length emerges from the analysis:

$$\ell_c = 2\pi\sqrt{A\frac{H_\chi + H}{H_\chi |H|}} \tag{65}$$

When H_χ is sufficiently large, ℓ_c in Eq. (65) tends to $2\pi\sqrt{A/|H|}$ which corresponds to the characteristic length for the Aifantis model (see Remark 1).

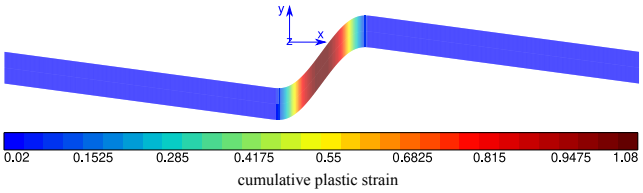

Fig. 14: Localization band in a periodic strip under simple glide conditions ($\overline{F}_{12} = 0.12$); $R_0 = 20$ MPa, $H = -20$ MPa, $H_\chi = 10^5$ MPa, $A = 1$ N, $h = 5$ mm.

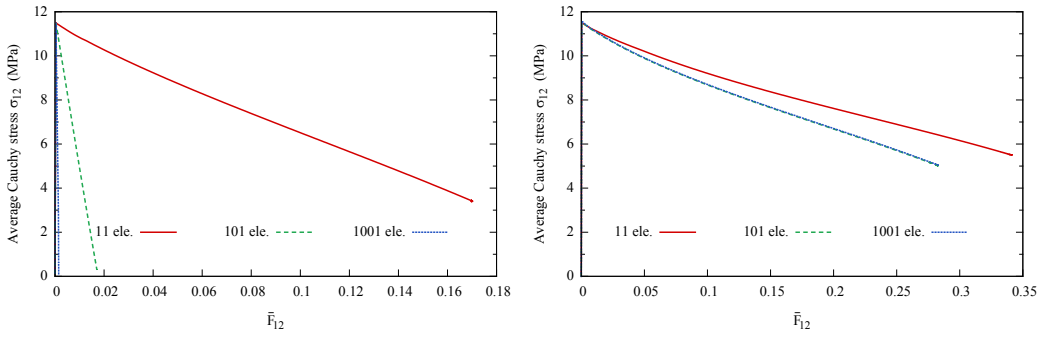

Fig. 15: Mesh dependency for (a) the classical plasticity model, (b) the micromorphic enhanced model. The corresponding material parameters are indicated in the caption of Fig. 14

The curves in Fig. 15a show that the overall response of the softening material without micromorphic enhancement pathologically depends on the mesh size since the plastic strain is localized in only one single element. However, by considering a micromorphic model, the simulations will converge to one well–defined response as soon as the mesh is sufficiently refined, see Fig. 15b. The yield stress evolves according to the equation

$$\sigma_Y = R_0 + R = R_0 + Hp - a_0 = R_0 + Hp + H_\chi(p - p_\chi) \tag{66}$$

The two softening/hardening contribution are depicted in Fig. 16. The generalized stress $a_0 = -H_\chi(p - p_\chi)$ is negative in the middle of the strip. This contribution therefore counteracts the softening term Hp ($H < 0$) in Eq. (66). Fig. 17 shows the profiles of cumulative

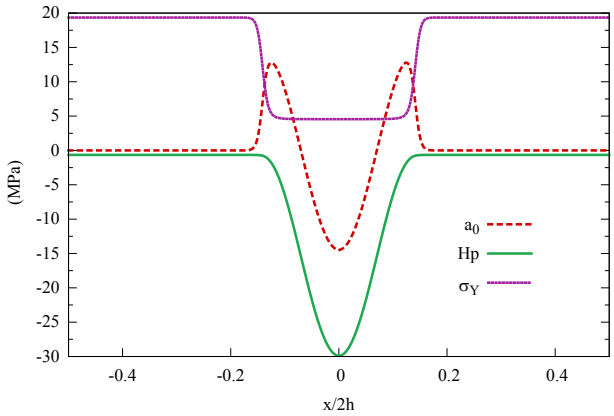

Fig. 16: Radius σ_Y of the yield surface, the generalized stress a_0 and the contribution of the linear softening term Hp along the strip length ($\overline{F}_{12} = 0.12$); $R_0 = 20$ MPa, $H = -20$ MPa, $H_\chi = 10^5$ MPa, $A = 4$ N, $h = 5$ mm.

plastic strain and the generalized stress a_0 for different values of the parameter A. By increasing A, and consequently the characteristic length ℓ_c, the magnitude of plastic strain and of a_0 becomes smaller and the band width is larger.

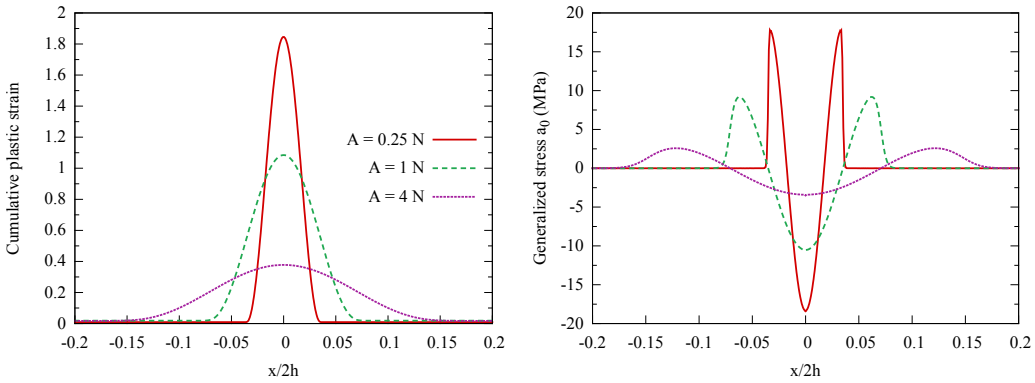

Fig. 17: The distribution of cumulative plastic strain and the generalized stress $a_0 = A\Delta_0 p_\chi$ for different values of generalized modulus A; $\overline{F}_{12} = 0.12$.

The distribution of plastic strain and stress-strain curves given by the three proposed finite strain formulations are plotted in Fig. 18. For a value of imposed macroscopic shear $\overline{F}_{12} = 0.4$, one can notice that the cumulative plastic strain given by the Lagrangian formulation is slightly higher compared to the two other formulations (see Fig. 18a). Accordingly, the average Cauchy stress σ_{12} tends to be lower. Formulations w.r.t. Eulerian and intermediate configurations yield similar profile of cumulative plastic strain. Meanwhile, deviations are noticed between corresponding stress-strain curves at large strain due to the kinematic hardening term $\underset{\sim}{\boldsymbol{X}}^b$.

In the case of linear softening ($H < 0$), the bandwidth is bounded and takes a finite and fixed value, as shown by Fig. 19a. Now, consider an exponential softening law by replacing the linear hardening term (Hp) in Eq. (63) by the saturating function $R_{sat}(p)$ given by

$$R_{sat}(p) = Q(1 - \exp(-cp)) \tag{67}$$

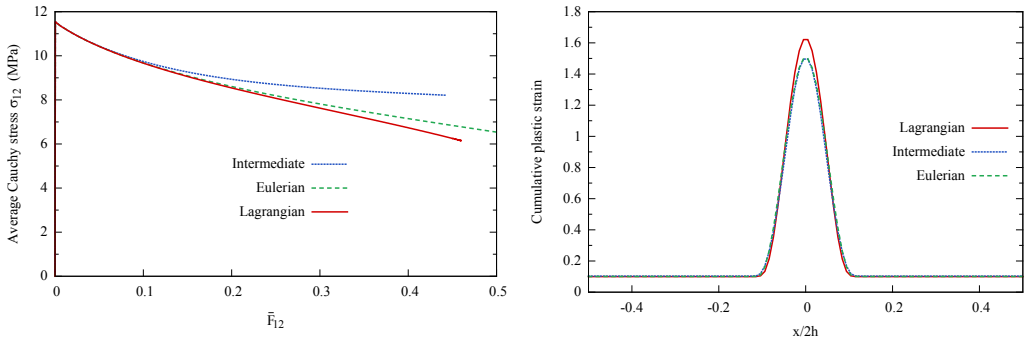

(a) stress-strain curves

(b) profiles of p, $\overline{F}_{12} = 0.4$

Fig. 18: Shear banding for the three finite strain formulations. Material parameters: $R_0 = 20$ MPa, $H_\chi = 10^4$ MPa, $A = 2$ N.

where Q and c are material parameters. Softening is obtained for $Q < 0$, c being always taken positive. In that case, R_{sat} will decrease from 0 at $p = 0$ to the limit Q for $p \to \infty$. Fig. 19b reveals a widening of the localization band for continuing applied shear. This can be explained as follows. For a nonlinear law, the instantaneous softening modulus is $H_\epsilon = \overline{\rho}\dfrac{\partial^2 \psi^h}{\partial p^2}$. When the softening law $\dfrac{\partial \psi}{\partial p}$ saturates (*e.g.* R_{sat}), H_ϵ tends to zero. Therefore, the intrinsic length given in Eq. (65) (replace H par H_ϵ) tends to infinity as plastic strain increases.

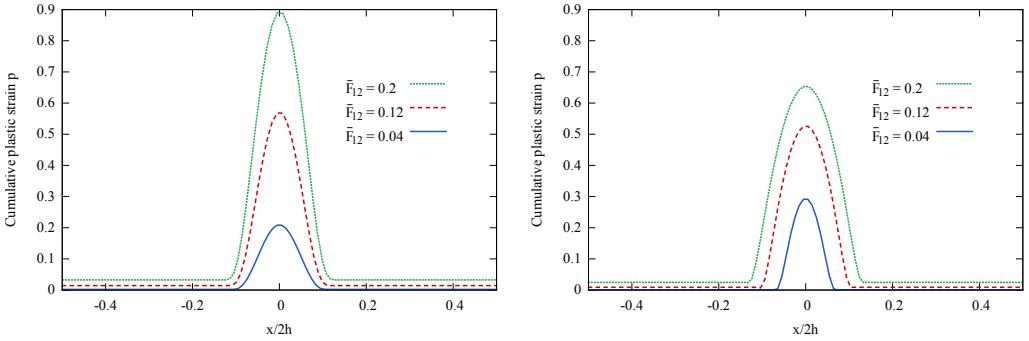

(a) Linear softening ($H = -20$ MPa)

(b) Exponential softening ($Q = -15$ MPa, $c = 10$)

Fig. 19: The exponential softening behavior induces widening of the localization band. Material parameters: $R_0 = 20$ MPa, $A = 2$ N, $H_\chi = 10^5$ MPa.

The band broadening is observed for all three finite strain formulations. The band widening can be an undesirable feature of strain localization simulations. It will happen in case of localization of plastic strain much larger than the saturating softening strain. This feature of the model has been recognized by [24]. A remedy was proposed to ensure that the band remains in a bounded region for ever increasing strain values. It consists in considering that the material parameter A is not constant any more but depends on plastic strain level. That is to say that the width of the localization band is bounded by adjusting properly the value of $A(p)$. It is noteworthy that for nonlinear softening laws at finite strains, only approximate evolutions of A can be derived. By doing that, $A(p)$ tends to decrease for further straining

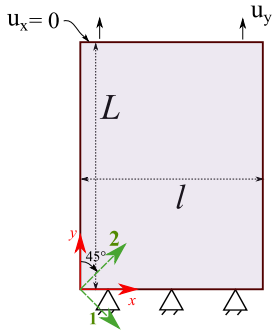

Fig. 20: Schematic of the geometry and boundary conditions for the plane-strain tension problem. The material frame is rotated by -45°. Geometry: $2L = 3l$.

$\overline{F}_{12}$. Consequently, continuing plastic flow was found in [24] to localize in a narrower band until it reaches the size of a single element. At the end, the classical model behavior is retrieved. A similar method was proposed in [79] for ductile damage, and recently in [80, 81]. In these contributions, an exponential function $A(p)$ is introduced within a large deformation constitutive framework. All these works introduce a Lagrangian gradient formulation in which the characteristic length is a decreasing function of plastic strain.

5.2 Anisotropic shear banding in a plate in tension

The shear band formation in a plate in tension is studied in this section in the case of an anisotropic contribution of the micromorphic model represented by the symmetric second order tensor $\underset{\sim}{\boldsymbol{A}}$, see Eq. (33). The orthotropic class symmetry for $\underset{\sim}{\boldsymbol{A}}$ is associated with 3 distinct eigenvalues A_1, A_2, A_3 and 3 orthogonal eigenvectors characterizing the material anisotropy axes. The two-dimensional plate of width $l = 400$ mm and length $L = 3l/2$ is shown in Fig. 20 where the red axes denote the Cartesian coordinate system of the mesh whereas the green axes represent the material anisotropy axes. The simulations are limited to plane-strain conditions, so that only the eigenvalues $A_1 \neq A_2$ play a role in the simulation. Regarding boundary conditions, the nodes along the bottom edge are prescribed to have displacement component $u_x = 0$ and $u_y = 0$, while the nodes along the top part are prescribed to have $u_x = 0$ and a non-zero u_y displacement is applied. The remaining edges are taken to be traction-free. Due to the fact that top and bottom edges are clamped, i.e. not allowed to contract, localization bands emerge automatically in this simulation. Hence, no imperfection is introduced to trigger shear bands at a specific location. This example has been studied previously in [51], also using the micromorphic approach at large deformations (Lagrangian formulation), but the analysis was limited to an isotropic gradient contribution. Quadratic elements with eight nodes and nine integration points C2D8R (reduced integration) are employed, meaning that the same quadratic interpolation is used for displacement and micromorphic degrees of freedom. Fig. 21 shows the localization bands at tensile displacements u_y/L of 0.02 and 0.14 for isotropic and anisotropic generalized moduli $\underset{\sim}{\boldsymbol{A}}$. The material frame is rotated by an angle of $-45°$ so that the anisotropy axes are parallel to the localization bands. A perfect plasticity model is used for this simulation. For isotropic generalized moduli $\underset{\sim}{\boldsymbol{A}} = A\underset{\sim}{\mathbf{1}}$ ($A_1 = A_2$), the resulting bands are strictly symmetric w.r.t. the y and $x-$axes. In the anisotropic case, the localization band that is parallel to the A_1 eigenvector, i.e. the smallest value, is wider, more diffuse and has a lower peak value than the second one. Anisotropy therefore breaks the symmetry of the geometry and loading conditions. The plastic strain profiles along two lines perpendicular to the localization bands are plotted in Fig. 22 in the anisotropic case at 5 loading stages. The two lines are indicated

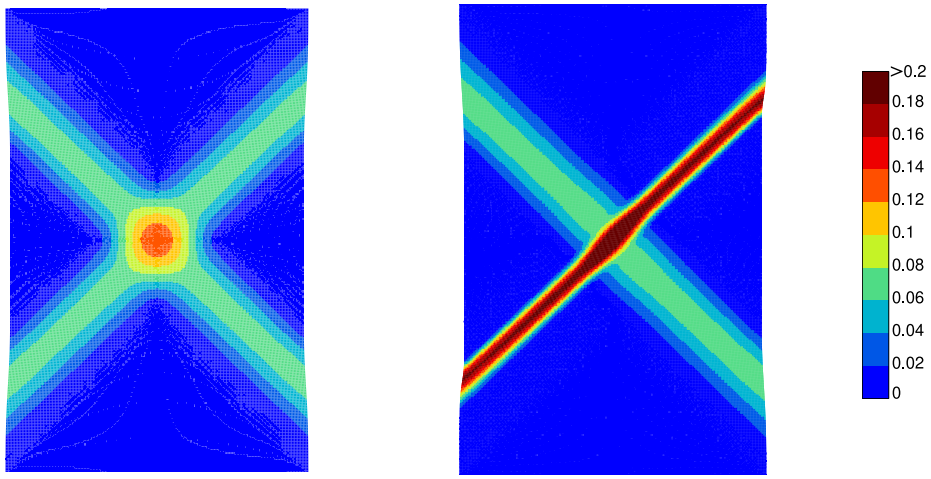

(a) $A_1 = A_2 = 10000$ N (b) $A_1 = 1000$ N, $A_2 = 10000$ N

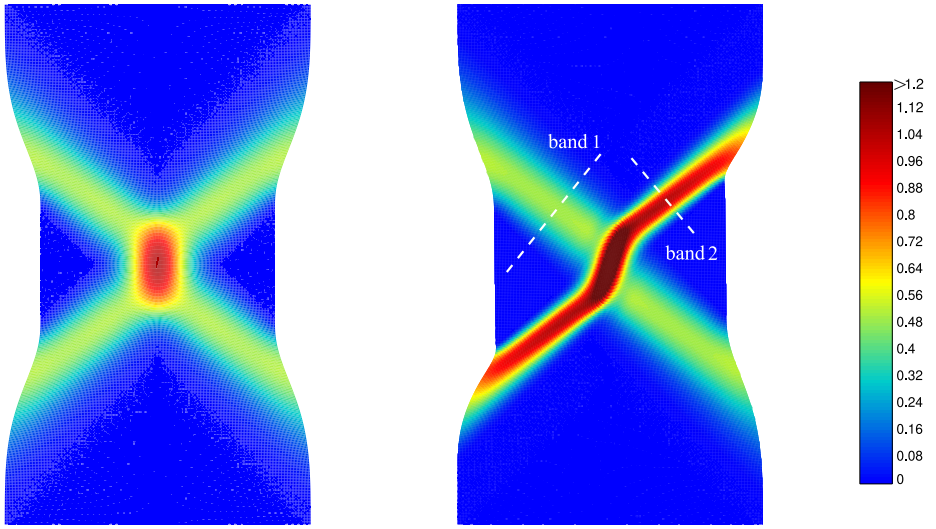

(c) $A_1 = A_2 = 10000$ N (d) $A_1 = 1000$ N, $A_2 = 10000$ N

Fig. 21: The localization of cumulative plastic strain in a plate under tension. Results obtained for applied displacement of: (a)-(b) $u_y/L = 0.02$, (c)-(d) $u_y/L = 0.14$. Material parameters $R_0 = 100$ MPa, $H = -20$ MPa, $H_\chi = 10^5$ MPa. The left (resp. right) pictures correspond to isotropic (resp. anisotropic) gradient contribution in the model.

in Fig. 21d. At small plastic strain levels (levels 1 and 2), the width of the two bands is correctly estimated by means of the formula

$$\ell_c^1 = 2\pi\sqrt{A_1\frac{(H_\chi + H)}{|H|H_\chi}} \approx 44.4, \qquad \ell_c^2 = 2\pi\sqrt{A_2\frac{(H_\chi + H)}{|H|H_\chi}} \approx 140.5 \tag{68}$$

which correspond to independent characteristic lengths induced by A_1 and A_2, respectively. Band 1 is initially significantly wider than band 2. This is due to the fact that the gradient of plastic strain in the direction perpendicular to the band is the dominant gradient component, as can be seen from the fields for Fig. 21b-d. Only one constant A_2 (resp. A_1) then plays a role in the constitutive equations inside band 1 (resp. band 2). After further straining, gradients

of plastic strain parallel to the bands also become significant, leading to a broadening of the bands towards a finite width which is essentially the same for both bands due to the combined influence of parameters A_1 and A_2. However the plastic strain inside the bands remains different due to the localization history of each band.

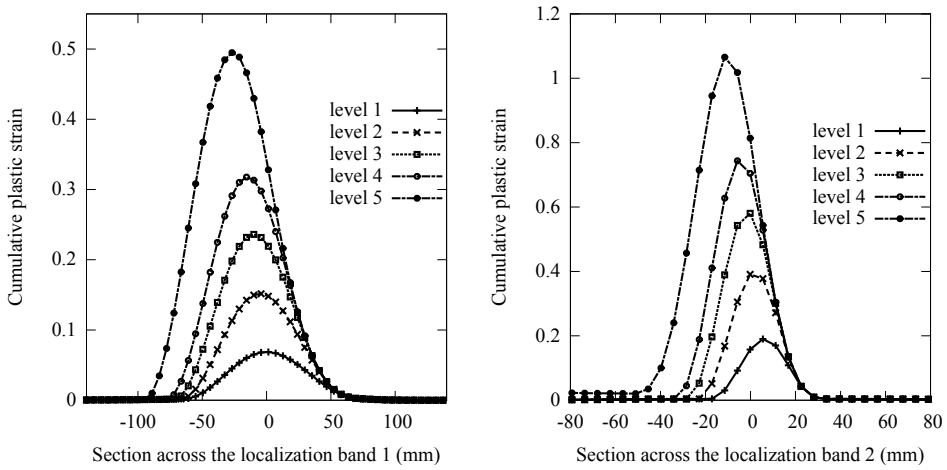

Fig. 22: The evolution of two localization bands for anisotropic generalized moduli with $A_1 = 10000$ N, $A_2 = 1000$ N. Levels 1,2,3,4 and 5 correspond to nominal applied displacement u_y/L of 0.02, 0.04, 0.06, 0.08 and 0.14, respectively.

6 Discussion

Several aspects of the previous simulations are discussed in this section, including limitations of the scalar gradient micromorphic approach and possible remedies. Computational aspects are addressed for an efficient use of gradient plasticity models in practical applications.

6.1 Choice of interpolation

The computation of the generalized stress $a = -H_\chi(p - p_\chi)$ involves two quantities p and p_χ. The cumulative plastic strain p is calculated incrementally by integrating the usual elasto-plasticity constitutive equations. Accordingly, p is related to the deformation gradient $\underset{\sim}{\boldsymbol{F}}$ which is computed as a function of the gradient of shape functions selected for displacement interpolation. If these shape functions are quadratic, the interpolation degree for the deformation gradient is mainly linear. Hence, p_χ should have the same interpolation degree, *i.e.* linear shape functions. On the other hand, the proposed micromorphic model is a first gradient theory meaning that only the first gradient of the degrees of freedom is evaluated. Accordingly, the same degree of interpolation can be used for displacement and micromorphic deformation degrees of freedom. Two interpolation schemes are evaluated in this section, namely P2P1 elements for which displacement and micromorphic deformation interpolation functions are respectively quadratic and linear, and P2P2 elements involving quadratic Lagrange polynomials for both types of degrees of freedom. Elements with linear shape functions for displacement (P1P1-type elements) are excluded here because they are subject to hour-glass arising in the early stage of plasticity and leading to strong oscillations in the displacement and micromorphic variable fields.

On the one hand, the use of P2P1 elements is advantageous because it involves a smaller number of degrees of freedom in the finite element simulation. On the other hand, the use of the same interpolation functions may be useful for practical reasons. In applications where boundary conditions on displacement and micromorphic variables are to be applied, using different interpolation degrees requires the duplication of lines and surfaces forming the boundaries for considering the proper nodes involved. Indeed, handling such issues is necessary to conduct systematic enhancement of classical models in finite element codes. This somewhat cumbersome treatment of boundaries is seen as a drawback of P2P1.

The performance of these elements is evaluated in the case of torsion of the 3D circular bar of Fig. 12 up to an applied angle $\theta = \pi$. The FE mesh is made of 18000 quadratic elements with reduced integration (C3D20R) and 77511 nodes. Brick elements with 20 nodes and reduced integration possessing 8 Gauss points (instead of 27 for full integration) are employed. Reduced integration is preferred in incompressible plasticity in order to limit fluctuations of the hydrostatic stress. The performance of P2P1-type and P2P2-type elements is compared in Table 2 which provides the number of degrees of freedom (DOFs), the total number of Newton iterations to solve the entire problem with the same given precision and the total CPU time on a single node with 24 processors whose characteristics are given in the caption. The use of P2P2-type element leads to 30% higher computational time due mainly to a 23% larger number of DOFs. Besides that, no significant differences between stress and plastic strain fields are noticed.

type of elements	number of DOFs	total number of iterations	total CPU time (s)
P2P1	252389	602	3.24×10^5
P2P2	310044	602	4.41×10^5

Table 2: Computational cost for different element types. Simulations of a cylinder torsion, meshed with 18000 C3D20R elements, run on 24 processors of type Intel(R) Xeon(R) CPU E5-2650 v4 @2.20 GHz. $R_0 = 300$ MPa, $H = 0$, $H_\chi = 10^4$ MPa, $A = 10$ N.

6.2 Micromorphic vs. strain gradient plasticity

In the following, a comparison between Lagrange multiplier based strain gradient plasticity (see Sec. 2.7) with the micromorphic approach is carried out. The strain gradient plasticity model can be seen as the limit of the micromorphic model when increasing the penalty modulus H_χ, as discussed in Remark 1 and Sec. 2.7. In the micromorphic approach, increasing the penalty parameter reduces the gap between the micromorphic variable p_χ and the macro-variable p. The main drawback of the Lagrange based strain gradient plasticity element is that it involves 5 DOFs per node (namely $u_1, u_2, u_3, p_\chi, \lambda$) versus 4 in the micromorphic element. The additional DOF is the Lagrange multiplier λ for which linear interpolation is used (P2P1P1 element). In contrast, the drawback of the micromorphic approach is related to possible numerical problems induced by ill-conditioned matrices in case of high values of the parameter H_χ. These aspects are investigated in the sequel.

The performance of micromorphic and strain gradient plasticity elements is evaluated in the case of torsion of a circular bar, i.e. the same boundary value problem as in the previous section. Table 3 summarizes the results obtained for torsion of a cylinder meshed with 18000 C3D20R elements of type P2P1 (total number of DOFs: 252389). A von Mises perfectly plastic model enhanced by the micromorphic approach is considered. The maximum gap between p and p_χ is observed in the vicinity of the neutral axis (see Fig. 13a). This gap decreases as the parameter H_χ increases. If H_χ is not sufficiently large, the gap between p and p_χ becomes very large (61%). In fact, by multiplying H_χ by 100, the maximum gap

	Micromorphic					Lagrange multiplier
	$H_\chi = 10$	$H_\chi = 10^3$	$H_\chi = 10^5$	$H_\chi = 10^7$	$H_\chi = 10^9$	
Max of $\lvert p - p_\chi \rvert / p_{ref}$	0.61	0.13	0.007	9×10^{-5}	9×10^{-7}	-
Total number of iterations	766	605	600	612	673	601
Total CPU time (s)	4.118×10^5	3.26×10^5	3.22×10^5	3.29×10^5	3.61×10^5	3.99×10^5

Table 3: The maximum gap between micro- and macro-variables and the computational cost for several values of H_χ (unit MPa). The maximum value of cumulative plastic strain, regarded as a reference value, is $p_{ref} = 0.19$ obtained for $r\theta/L = 0.314$. Simulations of a cylinder torsion, meshed with 18000 C3D20R elements (P2P1-type element and 252389 DOFs for the micromorphic model, P2P1P1-type elements and 272245 DOFs for the Lagrange multiplier based approach). Material parameters: $R_0 = 300$ MPa, $A = 10$ N, $H = 0$ MPa.

	Micromorphic			Lagrange multiplier
	$H_\chi = 10^3$	$H_\chi = 10^5$	$H_\chi = 10^7$	
Max of $\lvert p - p_\chi \rvert / p_{ref}$	2.64×10^{-2}	8.26×10^{-4}	9.1×10^{-6}	-
Total number of iterations	749	719	1395	700
Total CPU time (s)	7.61×10^4	7.3×10^4	1.53×10^5	1.03×10^5

Table 4: The maximum gap between micro- and macro-variables and the computational cost for several values of H_χ (unit MPa). The maximum value of cumulative plastic strain, regarded as a reference value, is $p_{ref} = 0.65$ obtained for $u_y = 1/12$ mm (level 4). Simulations are performed using the rectangular plate under tension meshed with 60000 C2D8R elements. P2P1-type element and 422503 DOFs for the micromorphic model, P2P1P1-type elements and 483004 DOFs for the Lagrange multiplier based approach. Material parameters $R_0 = 100$ MPa, $H = -20$ MPa, $A = 10000$ N. The plate geometry 400×600 mm.

decreases by a ratio of 4, 18 and 77 consecutively. This means that the isotropic hardening $H_\chi(p - p_\chi)$ induced by the enhanced model increases rapidly with H_χ for smaller values of H_χ and tends to saturate for larger values of H_χ. The computational cost of simulations using different H_χ remains almost the same. Indeed, for the same number of loading increments, the total number of iterations of Newton-algorithm required to resolve the global problem is relatively constant for $H_\chi = 10^3, 10^5, 10^7$ MPa. Conversely, when H_χ is either significantly smaller or larger than elasticity moduli, the simulation requires higher number of iterations to converge.

On the other hand, the approach based on Lagrange multipliers enforces weakly the equality of local and non-local variables. Meanwhile, this cannot be achieved without numerical difficulties. The augmented Lagrangian term, which is similar to the micromorphic contribution in the free energy potential is known to provide more coercivity, hence attenuate the oscillations of plastic fields [25, 52]. For a given value of μ_χ in Eq. (58), a finer mesh leads to a smoother profile of the Laplacian term $\Delta_\chi = \lambda + \mu_\chi p_\chi$. In other words, increasing the discretization reduces the value of μ_χ required to obtain a smooth profile of Δ_χ. Moreover, the value of an optimal μ_χ depends also on the intrinsic length. In fact, larger values of intrinsic length, or, equivalently, parameter A, require a larger value of μ_χ to smooth the profile of plastic strain.

Table 4 summarizes the computational performance of micromorphic and Lagrange multiplier approaches in case of the plane-strain tension of a plate discussed in Sec. 5.2. A softening case is studied inducing shear band localization as in Fig. 21a-c, for an isotropic gradient contribution. For moderate penalty modulus H_χ, the micromorphic approach performs relatively better compared to the Lagrange multiplier approach. This can be explained mainly by the fact that the Lagrange multiplier based approach involves a larger number of DOFs. Meanwhile, in the case of large values of $H_\chi = 10^7$ MPa, the micromorphic model requires a larger number of iterations to converge. In the presence of localization, high values of H_χ are required to obtained small gaps $\lvert p - p_\chi \rvert$ inside the band. This is associated

with more numerous iterations for the micromorphic model than in the Lagrange multiplier based approach. A compromise is to be found on the tolerance for the gap $|p-p_\chi|$ in various situations, noting that a relative gap less than 0.1% may be acceptable and both models perform similarly in that case.

Parameter H_χ of the micromorphic model can also be viewed as a constitutive parameter that can be calibrated against experimental data, as illustrated in [82] where both parameters A and H_χ are identified. The micromorphic model is more flexible regarding experimental identification, than the strict strain gradient plasticity model.

6.3 Choice of scalar micromorphic variables

In previous sections, the model based on a micromorphic scalar variable associated with cumulative plastic strain was discussed. However, it has been shown that this model gives rise to several issues:

- The radius of elastic domain is shown to depend on the gap between cumulative plastic strain p and the microplastic variable p_χ, or equivalently, on the Laplacian of the micromorphic variable according to Eq. (40). When p is smaller than p_χ, a material softening occurs as illustrated in the core of a beam under bending. But when the generalized stress $a=-H_\chi(p-p_\chi)$ tends to be larger than the radius given by the classical model (initial yield stress R_0 and isotropic hardening), a conceptual problem arises. This problem is more acute in case of time-independent plasticity where consistency condition needs to be satisfied.
- Another conceptual problem of some gradient plasticity formulations has been pointed out in [54]. Since scalar variables generally contain no information on the direction of the plastic flow, an arbitrary small perturbation in the boundary conditions can determine the direction of the plastic deformation in many scalar-based gradient formulations. Accordingly, the solution remains unstable w.r.t. boundary conditions. This problem arises in the case of the model with cumulative plastic strain. Meanwhile, a scalar model developed in [55] has been shown to overcome this conceptual problem. An extension of this model to finite strain was presented in 2.5.
- The cumulative plastic strain is by definition a non-saturating variable and can only increase. Moreover, its gradient may then also become higher and higher, as illustrated in Sec. 3. Indeed, the gap between p and p_χ becomes more significant. This will induce a higher value of isotropic hardening. For cyclic loading, this issue becomes more crucial. One could enforce the equality between p and p_χ by setting H_χ to large values. Nevertheless, the term $H_\chi|p-p_\chi|$ increases with H_χ, i.e. the induced isotropic hardening (or softening according to the sign of $p-p_\chi$) increases. The physical relevance of this unbounded cyclic hardening is questionable, see the discussion in [78].

In the following, the main results obtained for the model proposed in Sec. 2.5 are presented. Note that the resulting back-stress $\underset{\sim}{\boldsymbol{X}}_m$ in Eq. (50) is indeterminate at zero plastic strain. This particular case is regularized numerically as follows. At each iteration, $\underset{\sim}{\boldsymbol{X}}_m$ is computed as

$$\underset{\sim}{\boldsymbol{X}}_m = \frac{H_\chi}{3J_p}\frac{\left(\underset{\sim}{\boldsymbol{B}}^p - \underset{\sim}{\mathbf{1}}\right)\underset{\sim}{\boldsymbol{B}}^p}{B^p_{eq}+\epsilon}(B^p_{eq}-\chi) \tag{69}$$

where ϵ is a small real number taken as $\epsilon = 10^{-6}$ in the following simulations. Fig. 23 depicts the stress-strain curves obtained for a cyclic glide loading with confined plasticity. This test was considered in Sec. 3.1 for the gradient of cumulative plastic strain model. The results given by classical and two micromorphic models based on the cumulative plastic strain p and the equivalent plastic strain B^p_{eq} are compared. The classical case is that of an elastic perfectly plastic solid. The model based on B^p_{eq} leads to kinematic hardening with

795 a strong Bauschinger effect. Since the back-stress $\underset{\sim}{\boldsymbol{X}}_m$ depends only on the plastic strain tensor, its components remain bounded from one cycle to another. In contrast, the model with p induces an isotropic hardening that grows and grows over cycles. It can be noted that the slopes of stress-strain curves after yielding, during the first cycle ($\overline{F}_{12} \in [0,0.1]$), given by both micromorphic models overlap. That is to say that both models are equivalent for 800 monotonic loading, in particular for one-dimensional problems. Differences arise in the next cycles.

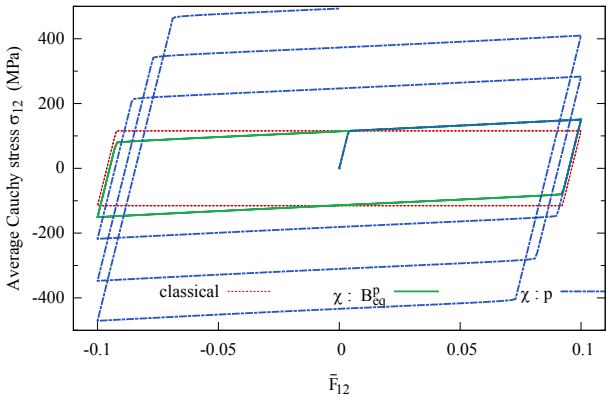

Fig. 23: Cyclic simple glide with confined plasticity for two micromorphic variables associated with p and B^p_{eq}.

Now consider the case of the bending example investigated in Sec. 4.1. A cyclic loading is applied and monitored by the displacement u_y at the top part of the foil (see Fig. 8). Fig. 24 depicts the bending moment vs. curvature curves for the two models based on cumulative 805 and equivalent plastic strain, respectively. Contrary to the model relying upon cumulative plastic strain that leads to isotropic overall hardening, the B^p_{eq}-model induces kinematic hardening.

Recall that the formulation of this model in the intermediate configuration will result in a supplementary back-stress $\underset{\sim}{\boldsymbol{X}}^b$. In case of cyclic loading with moderate imposed strains, 810 $\underset{\sim}{\boldsymbol{X}}^b$ remains negligible since it is a second order contribution. In contrast, the model with cumulative plastic strain induces a significant value of $\underset{\sim}{\boldsymbol{X}}^b$ for the same loading case (not shown here).

Although this model is based on the gradient of a scalar field variable B^p_{eq}, it takes into account the direction of the plastic strain, making the solution stable with respect to the boundary conditions. Indeed, the back-stress $\underset{\sim}{\boldsymbol{X}}_m$ resulting from the higher-order term is a function of the direction of the plastic strain tensor. In order to illustrate that, consider a von Mises viscoplastic model. For instance, a Norton-type viscoplastic potential is $\Omega = \dfrac{K}{n+1}\left\langle \dfrac{f}{K} \right\rangle^n$ where K and n are material parameters. Using the model with cumulative plastic strain, the flow rule and the yield criterion are given by

$$\underset{\sim}{\boldsymbol{L}}^p = \frac{\partial \Omega}{\partial \underset{\sim}{\boldsymbol{M}}} = \frac{\partial \Omega}{\partial f}\frac{\partial f(\underset{\sim}{\boldsymbol{M}})}{\partial \underset{\sim}{\boldsymbol{M}}} = \frac{3}{2}\frac{\underset{\sim}{\boldsymbol{M}}'}{J(\underset{\sim}{\boldsymbol{M}})}\left\langle \frac{f}{K} \right\rangle^n \tag{70}$$

$$f(\underset{\sim}{\boldsymbol{M}}) = [\underset{\sim}{\boldsymbol{M}}]_{eq} - R_0 - R(p) \tag{71}$$

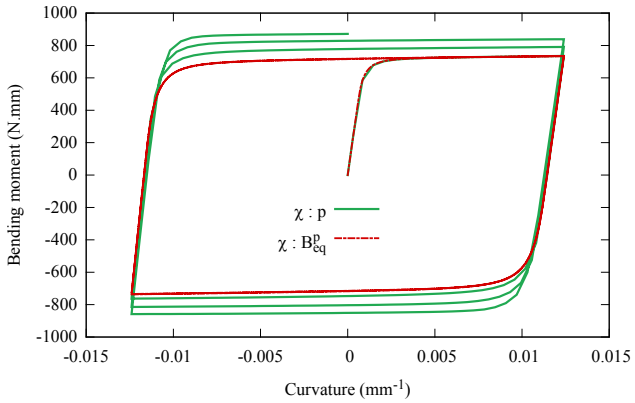

Fig. 24: Bending moment vs. curvature curves for a foil under cyclic loading for two micromorphic variables associated with cumulative plastic variable p and equivalent plastic strain B^p_{eq}. Quadratic Lagrangian formulation of the gradient term. Micromorphic parameters $A = 200$ N, $H_\chi = 10^4$ MPa.

where the von Mises equivalent stress is $[\diamond]_{eq} = \sqrt{\frac{3}{2}\underset{\sim}{\diamond}' : \underset{\sim}{\diamond}'}$ and $\underset{\sim}{\diamond}'$ is the deviatoric part of $\underset{\sim}{\diamond}$. It has been shown that the yield stress $\sigma_Y = R_0 + R$ may vanish in some situations, *e.g.* strong strain gradients. The deviatoric Mandel stress may also vanish (or Cauchy stress $\underset{\sim}{\boldsymbol{\sigma}}$) so that the flow rule in Eq. (70) cannot provide the direction of plastic flow $\underset{\sim}{\boldsymbol{L}}^p$. In contrast, the flow rule and the yield criterion for the model with B^p_{eq} write

$$\underset{\sim}{\boldsymbol{L}}^p = \frac{\partial \Omega}{\partial \underset{\sim}{\boldsymbol{M}}} = \frac{\partial \Omega}{\partial f}\frac{\partial f(\underset{\sim}{\boldsymbol{M}})}{\partial(\underset{\sim}{\boldsymbol{M}} - \underset{\sim}{\boldsymbol{X}}_m)} = \frac{3}{2}\frac{\underset{\sim}{\boldsymbol{M}}' - \underset{\sim}{\boldsymbol{X}}_m}{J(\underset{\sim}{\boldsymbol{M}} - \underset{\sim}{\boldsymbol{X}})}\left\langle \frac{f}{K} \right\rangle^n \tag{72}$$

$$f(\underset{\sim}{\boldsymbol{M}}) = [\underset{\sim}{\boldsymbol{M}} - \underset{\sim}{\boldsymbol{X}}_m]_{eq} - R_0 - R(p) \tag{73}$$

In the case of vanishing yield stress σ_Y, satisfaction of the yield criterion means that $(\underset{\sim}{\boldsymbol{M}}' - \underset{\sim}{\boldsymbol{X}}_m) \neq 0$. Therefore, the flow direction is always defined by Eq. (72).

6.4 Limitations of the model due to negative yield radius and remedies

As shown in the previous examples, the model based on the cumulative plastic strain may induce negative yield radius in the presence of high positive values of the Laplacian $\Delta_0 p_\chi$. A remedy has been proposed in the viscoplastic micromorphic model in [53] by substituting the yield radius by zero whenever it is negative, *i.e.* substitute $R_0 + R(p)$ in Eq. (51) by its positive part $\langle R_0 + R(p) \rangle$. Meanwhile, this remedy is not effective in the case of time-independent plasticity considered in the present work. When the radius of elastic domain is set to zero, the equivalent stress must vanish as well. Numerically, the performed simulations diverge when the radius of the yield surface tends to be negative with or without this modification. For viscoplastic models, due to overstress, the radius can be set to zero while the stress does not vanish. Nevertheless, by doing so the classical model is retrieved insofar as gradient terms are inactive.

The model relying upon equivalent plastic strain B^p_{eq} can be a plausible alternative. The hardening induced by this model manifests itself as a back-stress that can be either positive or negative. For instance, in bending and torsion examples shown previously, the components of the back-stress $\underset{\sim}{\boldsymbol{X}}_m$ go abruptly from large positive values to large negative values across the neutral axis (see Fig. 25). However, a drawback of the model is the indeterminacy of

the back-stress $\underset{\sim}{\boldsymbol{X}}_m$ when the plastic strain vanishes which may lead to some numerical difficulties. A regularized formulation was used here, see Eq. (69).

These examples show that the proposed remedies are still not completely satisfactory. Two other formulations are possible to overcome these difficulties. The first one is based on the gradient of tensor variables, gradient plasticity [43, 56, 57] or micromorphic plasticity [43, 53]. The second one is based on the use of saturating variables, like hardening variables, as mentioned in [20] or bounded variables like phase fields [83]. This remains to be explored in future works.

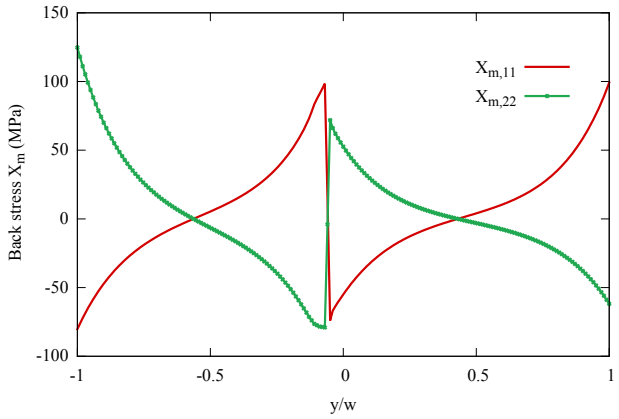

Fig. 25: Back-stress plotted at the cross section $x = 0$ for the bending example in section 4.1. Material parameters $R_0 = 100$ MPa, $H = 0$, $A = 2000$ N, $H_\chi = 10^4$ MPa. Results obtained for $\kappa = 0.0348$ mm^{-1}.

7 Conclusions

The major outcomes of the present work can be stated as follows:

1. A generic approach for micromorphic strain gradient plasticity at finite strains was presented. The finite element implementation is detailed with a particular focus on scalar micromorphic variables. Models were assessed for a variety of benchmarks involving monotonic and cyclic loading conditions.
2. Two main features of micromorphic elastoplastic models are emphasized. First, size effects can be predicted by varying two additional material parameters (A and H_χ contrarily to Aifantis-like models with only one parameter referred to as intrinsic length). Second, the same models allow regularizing finite element simulations of plastic strain localization by canceling the spurious mesh-dependency linked to classical continua without intrinsic length.
3. Three finite strain formulations are discussed based on quadratic functions of the gradient terms w.r.t. either Eulerian, Lagrangian or intermediate configurations. Eulerian and Lagrangian formulations of the gradient of cumulative plastic strain enhance classical elastoplastic models by a supplementary size-dependent isotropic hardening. The formulation defined in the intermediate configuration leads to both isotropic and kinematic size-dependent hardening. The supplementary back-stress is a second-order contribution that vanishes within the small strain limit. Significant differences between the formulations are therefore observed under cyclic loading. Decision on the best framework eventually remains material-dependent.

4. The choice of the micromorphic variable and free energy potentials leads to a wide range of constitutive models. Indeed, the model based on the cumulative plastic strain is shown to induce a size-dependent isotropic hardening whereas the model with equivalent plastic strain results in a size-dependent kinematic hardening. For the sake of demonstration, only quadratic potentials w.r.t. gradient terms were investigated. More general gradient contributions such as power laws can be implemented [36].
5. The model based on cumulative plastic strain leads to a material softening and possibly vanishing or negative yield radius in regions where the plastic strain profile is non-smooth. This feature is related to possible divergence of the integration scheme. To overcome this limitation, an alternative model relying upon gradient of equivalent plastic strain was suggested. Meanwhile, the indeterminate back-stress at zero plastic strain may lead to numerical difficulties under cyclic loading and in regions where the plastic strain vanishes (in the neutral axis in torsion and bending).
6. Numerical comparison between micromorphic approach and Lagrange-multiplier based strain gradient plasticity was carried out. The computational cost of both approaches is shown to be similar. Meanwhile, in the case of applications that involve some instabilities like strain localization modes, the micromorphic approach may perform poorly for very large penalty moduli H_χ since the model becomes stiffer. On the other hand, such large values may not be necessary to obtain satisfactory accordance between micro and macro-variables. A drawback of the presented FE implementation for the Lagrange-multiplier model is that continuity of the Lagrange multiplier λ is enforced by the chosen shape function although this is a too strong requirement, as discussed in Appendix B.3.7. Discontinuous Galerkin methods could be used to overcome this limitation.

The choice of the micromorphic variable was shown to play a key role in the present work which was however limited to plasticity. The present work will be completed in the future by studying other scalar variables, *e.g.* a saturating variable [84, 85] and the equivalent total strain proposed in [44]. Moreover, further investigations on micromorphic models accounting for tensor micromorphic variables [14, 20, 86] will be carried out. Dissipative contributions of gradient terms should also be considered following [3, 43] and [36, 72, 87, 88]. In the two first latter references, the higher order gradients are decomposed into elastic and plastic parts in the same way as conventional strain measures. In the remaining references, the higher order stresses are decomposed into reversible and dissipative contributions. Enhancements of damage models for simulation of crack initiation and propagation have been proposed recently based on the micromorphic approach, see [89–92]. The micromorphic approach can also be useful to ease numerical implementation of phase field models as demonstrated recently for twinning plasticity in [93]. Note finally that the micromorphic approach is also suitable for explicit finite element simulation schemes used in metal forming as recently shown in [16, 94].

Appendix

A Consistent tangent matrices in the numerical implementation

The derivation of the consistent tangent matrix for a time-independent plastic model is detailed in this first appendix. For the sake of brevity, only the model with a micromorphic variable associated with cumulative plastic strain is detailed in the following.

The global resolution algorithm requires the following partial derivatives:

$$\frac{\partial \Delta \mathcal{V}_{OUT}}{\partial \Delta \mathcal{V}_{IN}} = \begin{bmatrix} \frac{\partial \Delta \underset{\sim}{\boldsymbol{P}}}{\partial \Delta \underset{\sim}{\boldsymbol{F}}} & \frac{\partial \Delta \underset{\sim}{\boldsymbol{P}}}{\partial \Delta \chi} & \frac{\partial \Delta \underset{\sim}{\boldsymbol{P}}}{\partial \Delta \underline{\boldsymbol{K}}} \\ \frac{\partial \Delta a}{\partial \Delta \underset{\sim}{\boldsymbol{F}}} & \frac{\partial \Delta a}{\partial \Delta \chi} & \frac{\partial \Delta a}{\partial \Delta \underline{\boldsymbol{K}}} \\ \frac{\partial \Delta \underline{\boldsymbol{b}}}{\partial \Delta \underset{\sim}{\boldsymbol{F}}} & \frac{\partial \Delta \underline{\boldsymbol{b}}}{\partial \Delta \chi} & \frac{\partial \Delta \underline{\boldsymbol{b}}}{\partial \Delta \underline{\boldsymbol{K}}} \end{bmatrix} = \begin{bmatrix} J(\underset{\sim}{\boldsymbol{\sigma}} \underset{\sim}{\boldsymbol{F}}^{-T}) \otimes \underset{\sim}{\boldsymbol{F}}^{-T} - J(\underset{\sim}{\boldsymbol{\sigma}} \underline{\otimes} \underset{\sim}{\boldsymbol{1}}) : (\underset{\sim}{\boldsymbol{F}}^{-T} \bar{\otimes} \underset{\sim}{\boldsymbol{F}}^{-1}) & \boldsymbol{0} & \boldsymbol{0} \\ \boldsymbol{0} & H_\chi & \boldsymbol{0} \\ \boldsymbol{0} & \boldsymbol{0} & \underline{\underline{\boldsymbol{A}}} \end{bmatrix} \tag{74}$$

$$\frac{\partial \Delta \mathcal{V}_{OUT}}{\partial \Delta \mathcal{V}_{int}} = \begin{bmatrix} \frac{\partial \Delta \underset{\sim}{\boldsymbol{P}}}{\partial \Delta \underset{\sim}{\boldsymbol{F}}^e} & \frac{\partial \Delta \underset{\sim}{\boldsymbol{P}}}{\partial \Delta p} \\ \frac{\partial \Delta a}{\partial \Delta \underset{\sim}{\boldsymbol{F}}^e} & \frac{\partial \Delta a}{\partial \Delta p} \\ \frac{\partial \Delta \underline{\boldsymbol{b}}}{\partial \Delta \underset{\sim}{\boldsymbol{F}}^e} & \frac{\partial \Delta \underline{\boldsymbol{b}}}{\partial \Delta p} \end{bmatrix} = \begin{bmatrix} \frac{\partial \Delta \underset{\sim}{\boldsymbol{P}}}{\partial \Delta \underset{\sim}{\boldsymbol{\sigma}}} : \frac{\partial \Delta \underset{\sim}{\boldsymbol{\sigma}}}{\partial \Delta \underset{\sim}{\boldsymbol{F}}^e} & \boldsymbol{0} \\ \boldsymbol{0} & -H_\chi \\ \boldsymbol{0} & \boldsymbol{0} \end{bmatrix} \tag{75}$$

with

$$\frac{\partial \Delta \underset{\sim}{\boldsymbol{P}}}{\partial \Delta \underset{\sim}{\boldsymbol{\sigma}}} = J \, \underset{\sim}{\boldsymbol{1}} \bar{\otimes} \underset{\sim}{\boldsymbol{F}}^{-1} \tag{76}$$

$$\frac{\partial \Delta \underset{\sim}{\boldsymbol{\sigma}}}{\partial \Delta \underset{\sim}{\boldsymbol{F}}^e} = -\frac{1}{J^e}(\underset{\sim}{\boldsymbol{F}}^e \underset{\sim}{\boldsymbol{\Pi}}^e \underset{\sim}{\boldsymbol{F}}^{eT}) \otimes \underset{\sim}{\boldsymbol{F}}^{e-T} + \frac{1}{J^e} \underset{\sim}{\boldsymbol{1}} \bar{\otimes} (\underset{\sim}{\boldsymbol{F}}^e \underset{\sim}{\boldsymbol{\Pi}}^e) + \frac{1}{2J^e} \left(\underset{\sim}{\boldsymbol{F}}^e \bar{\otimes} \underset{\sim}{\boldsymbol{F}}^e \right) : \frac{\partial \underset{\sim}{\boldsymbol{\Pi}}^e}{\partial \underset{\sim}{\boldsymbol{E}}^e} : \left(\underset{\sim}{\boldsymbol{1}} \underline{\otimes} \underset{\sim}{\boldsymbol{F}}^{eT} + \underset{\sim}{\boldsymbol{F}}^{eT} \bar{\otimes} \underset{\sim}{\boldsymbol{1}} \right) \tag{77}$$

$$+ \frac{1}{J^e}((\underset{\sim}{\boldsymbol{F}}^e \underset{\sim}{\boldsymbol{\Pi}}^e) \bar{\otimes} \underset{\sim}{\boldsymbol{1}}) : (\underset{\sim}{\boldsymbol{1}} \underline{\otimes} \underset{\sim}{\boldsymbol{1}})$$

$$\frac{\partial \Delta \mathcal{R}}{\partial \Delta \mathcal{V}_{IN}} = \begin{bmatrix} \frac{\partial \mathcal{R}_e}{\partial \Delta \underset{\sim}{\boldsymbol{F}}} & \frac{\partial \mathcal{R}_e}{\partial \Delta \chi} & \frac{\partial \mathcal{R}_e}{\partial \Delta \underline{\boldsymbol{K}}} \\ \frac{\partial \mathcal{R}_p}{\partial \Delta \underset{\sim}{\boldsymbol{F}}} & \frac{\partial \mathcal{R}_p}{\partial \Delta \chi} & \frac{\partial \mathcal{R}_p}{\partial \Delta \underline{\boldsymbol{K}}} \end{bmatrix} = \begin{bmatrix} -\underset{\sim}{\boldsymbol{1}} \bar{\otimes} (\underset{\sim}{\boldsymbol{F}}^{-1} \underset{\sim}{\boldsymbol{F}}^e)^T + (\Delta \underset{\sim}{\boldsymbol{F}} \bar{\otimes} \underset{\sim}{\boldsymbol{F}}^{eT}) : (\underset{\sim}{\boldsymbol{F}}^{-1} \bar{\otimes} \underset{\sim}{\boldsymbol{F}}^{-T}) & \boldsymbol{0} & \boldsymbol{0} \\ \boldsymbol{0} & 1 & \boldsymbol{0} \end{bmatrix} \tag{78}$$

At Gauss point level, constitutive equations are integrated using a θ-method [63]. The values of all integrated variables evaluated at an intermediate time designated by $\theta \in [0, 1]$ are

$$\mathcal{V}_{int}^{t+\theta\Delta t} = \mathcal{V}_{int}^{t} + \theta \Delta \mathcal{V}_{int} \tag{79}$$

The set of equations (57) can be gathered in the following form

$$\mathcal{R}(\mathcal{V}_{int}^{t+\theta\Delta t}, \Delta \mathcal{V}_{int}) = 0 \tag{80}$$

Since Eq. (80) is highly nonlinear, it is usually solved by means of a Newton method which requires the calculation of the Jacobian matrix

$$\frac{\partial \Delta \mathcal{R}}{\partial \Delta \mathcal{V}_{int}} = \begin{bmatrix} \frac{\partial \mathcal{R}_e}{\partial \Delta \underset{\sim}{\boldsymbol{F}}^e} & \frac{\partial \mathcal{R}_e}{\partial \Delta p} \\ \frac{\partial \mathcal{R}_p}{\partial \Delta \underset{\sim}{\boldsymbol{F}}^e} & \frac{\partial \mathcal{R}_p}{\partial \Delta p} \end{bmatrix} = \begin{bmatrix} \underset{\approx}{\boldsymbol{1}} - \theta \underset{\sim}{\boldsymbol{L}} \bar{\otimes} \underset{\sim}{\boldsymbol{1}} + \theta \Delta p \underset{\sim}{\boldsymbol{N}} + \theta \Delta p \frac{\partial \underset{\sim}{\boldsymbol{N}}}{\partial \underset{\sim}{\boldsymbol{M}}} \frac{\partial \underset{\sim}{\boldsymbol{M}}}{\partial \underset{\sim}{\boldsymbol{F}}^e} & \underset{\sim}{\boldsymbol{F}}^e \underset{\sim}{\boldsymbol{N}} \\ \theta \underset{\sim}{\boldsymbol{N}} : \frac{\partial \underset{\sim}{\boldsymbol{M}}}{\partial \underset{\sim}{\boldsymbol{F}}^e} & -\frac{\theta}{H_\chi} \frac{\partial R}{\partial p} \end{bmatrix} \tag{81}$$

where $\underset{\sim}{\boldsymbol{N}} = \dfrac{\partial f}{\partial \underset{\sim}{\boldsymbol{M}}}$ is the normal to the yield surface. The value $\theta = 1$ (implicit integration) is used in the present work for rate-independent plasticity.

B Analytical solution for confined plasticity under shear

Consider the boundary value problem of Fig. 1a and introduced in Sec. 3.1. The strip is $2h$-wide and infinite in the y-direction (invariant solution in this direction). In the case of a hardening plate (i.e., $\mathrm{H} \geq 0$), the microplastic variable p_χ is set to zero at $x = \pm h$ (Dirichlet higher order boundary conditions). In the case of a softening plate (i.e., $\mathrm{H} < 0$), p_χ is free at $x = \pm h$ far from the localization zone (Neumann higher order conditions). The first balance equation reads

$$\mathrm{div}\, \underset{\sim}{\boldsymbol{\sigma}} = 0 \tag{82}$$

which yields

$$\sigma_{12,2} = 0 \text{ and } \sigma_{12,1} = 0 \tag{83}$$

Therefore, $\sigma_{12} = \tau$, taken positive without loss of generality, is uniform in the plate. The second balance equation is

$$\text{div } \underline{\boldsymbol{b}} = \text{a} \tag{84}$$

where the constitutive equations for generalized stresses are given by

$$a = -H_\chi(p - p_\chi), \qquad \underline{\boldsymbol{b}} = A\nabla p_\chi \tag{85}$$

The differential equation governing the microplastic variable p_χ reads

$$\Delta p_\chi - \frac{H_\chi}{A}(p_\chi - p) = 0 \tag{86}$$

The yield function is given by

$$f(\underline{\boldsymbol{\sigma}}, p) = \sigma_{eq} - (R_0 + Hp + H_\chi\,(p - p_\chi)) = 0 \tag{87}$$

with $\sigma_{eq} = \sqrt{3}\,\tau$ is the von Mises stress. By combining Eqs. (86) and (87), the following partial differential equation for p_χ is obtained

$$\Delta p_\chi - \frac{HH_\chi}{A(H + H_\chi)}p_\chi + \frac{H_\chi}{A(H + H_\chi)}(\sigma_{eq} - R_0) = 0 \tag{88}$$

Three different cases can be distinguished: perfect plasticity ($H = 0$), hardening ($H > 0$) and softening ($H < 0$) behavior.

B.1 Case 1: perfect plasticity (H = 0)

In this case, the equation (88) reduces to

$$\Delta p_\chi + \frac{1}{A}(\sigma_{eq} - R_0) = 0 \tag{89}$$

whose solution is

$$p_\chi(x) = -\frac{\sqrt{3}\tau - R_0}{2A}x^2 + C_1 x + C_2 \tag{90}$$

where C_1 and C_2 are integration constants to be determined from boundary conditions:

$$p_\chi(x = \pm h) = 0 \implies C_1 = 0 \quad \text{and} \quad C_2 = \frac{\sqrt{3}\tau - R_0}{2A}h^2 \tag{91}$$

Finally, the fields of micromorphic deformation and cumulative plastic strain are

$$p_\chi(x) = -\frac{\sqrt{3}\tau - R_0}{2A}(x^2 - h^2) \tag{92}$$

$$p(x) = p_\chi(x) + \frac{\sqrt{3}\tau - R_0}{H_\chi} \tag{93}$$

Further, the expression of the uniform stress τ in the plate is

$$\tau = 2\mu\varepsilon^e_{12} = \frac{\mu}{h}\int_{-h}^{h}(\varepsilon_{12} - \varepsilon^p_{12})dx = \mu\overline{\gamma} - \frac{\sqrt{3}\mu}{2h}\int_{-h}^{h}p(x)dx \tag{94}$$

Using Eq. (93), Eq. (94) reduces to

$$\tau = \frac{\overline{\gamma} + \dfrac{R_0}{\sqrt{3}}\left(\dfrac{3}{H_\chi} + \dfrac{h^2}{A}\right)}{\dfrac{1}{\mu} + \dfrac{3}{H_\chi} + \dfrac{h^2}{A}} \tag{95}$$

The parabolic profiles $p(x)$ et $p_\chi(x)$ are illustrated by Fig. 26 and used for the validation of the FE implementation of the model. It is apparent in Fig. 26a that the value $H_\chi = 10^5$ MPa ensures a very small difference $|p - p_\chi|$. It follows that the presented solution is almost identical to the solution of the same problem using the Aifantis strain gradient plasticity model. Increasing the parameter A flattens the profiles indicating that plastic deformation is more difficult to develop and higher stresses are reached. The limit $H_\chi \to \infty$ in Eq. (95) provides the shear stress level for the Aifantis model:

$$\tau = \frac{\mu}{A + \mu h^2}\left(A\overline{\gamma} + R_0 h^2/\sqrt{3}\right) \tag{96}$$

The limit $A \to \infty$ shows that deformation is then purely elastic: $\tau = \mu\overline{\gamma}$. Plastic strain gradient would be too high to develop. In contrast, setting $A = 0$ provides the classical elastic-perfectly plastic solution. The previous formula also reveals the apparent hardening modulus depending on A and the width h.

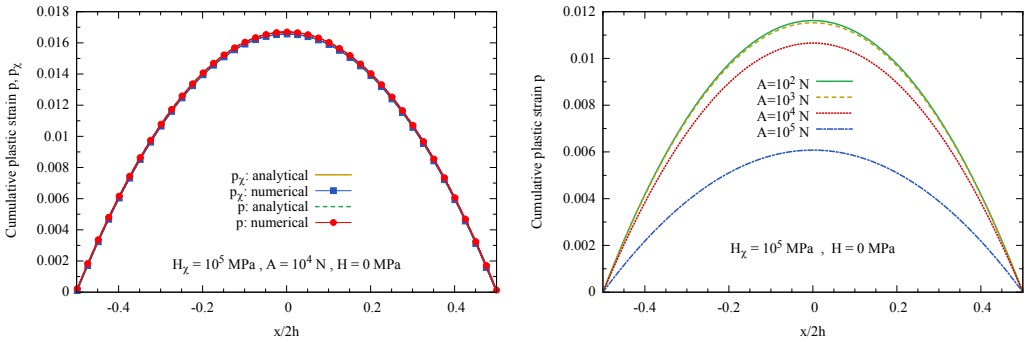

(a) (b)

Fig. 26: (a) Analytic vs. numerical fields of cumulative plastic strain p and micromorphic variable p_χ for confined simple glide; (b) distribution of cumulative plastic strain for different values of the generalized modulus A. The profiles are given for the prescribed overall shear value $\overline{\gamma} = 0.2$.

B.2 Case 2: H > 0 (hardening)

For a strictly positive linear hardening modulus, the solution of Eq. (88) reads

$$p_\chi(x) = C_3 \cosh(\omega x) + C_4 \sinh(\omega x) + \frac{\sigma_{eq} - R_0}{H} \tag{97}$$

where

$$\omega^2 = \frac{H H_\chi}{A(H + H_\chi)} \tag{98}$$

This formula defines the inverse characteristic length ω as a function of the plastic hardening modulus and higher order parameters. The integration constants C_3 and C_4 are obtained by applying boundary conditions:

$$p_\chi(x = \pm h) = 0 \implies C_3 = -\frac{\sigma_{eq} - R_0}{H \cosh(wh)} \text{ and } C_4 = 0 \tag{99}$$

It follows that

$$p_\chi(x) = \frac{\sqrt{3}\tau - R_0}{H}\left(1 - \frac{\cosh(\omega x)}{\cosh(\omega h)}\right) \tag{100}$$

and

$$p(x) = p_\chi(x) + \frac{\sqrt{3}\tau - R_0}{H + H_\chi}\frac{\cosh(\omega x)}{\cosh(\omega h)} = \frac{\sqrt{3}\tau - R_0}{H}\left(1 - \frac{H_\chi}{H + H_\chi}\frac{\cosh(\omega x)}{\cosh(\omega h)}\right) \tag{101}$$

The value of τ is given by

$$\tau = \frac{\overline{\gamma} + R_0 Z_h}{\dfrac{1}{\mu} + \sqrt{3} Z_h} \tag{102}$$

where $Z_h = \dfrac{\sqrt{3}}{H}\left(1 - \sqrt{\dfrac{A H_\chi}{H(H + H_\chi)}}\dfrac{\tanh(\omega h)}{h}\right)$ These results are illustrated by Fig. 27. A clear difference $|p - p_\chi|$ is visible in Fig. 27a for a low value of the penalty modulus $H_\chi = 10^3$ MPa. This difference almost vanished in Fig. 27b when H_χ is sufficiently high. This indicates again that the gradient plasticity model by [66] is a limit case of the micromorphic model as H_χ tends to infinity. The hyperbolic profiles can be recognized in Fig. 27c and 27d. Low values of the higher order modulus A lead to flat distribution of plastic strain where high curvatures are reached for high values of A.

B.3 Shear localization solution in micromorphic plasticity (Case 3: $H < 0$)

The development of a shear localization band in a homogeneous matrix strip is studied. The strip has a thickness of $2h$ in the x–direction and is infinite in the y–direction of the 2D shear plane. The stress state is homogeneous with

$$\underset{\sim}{\boldsymbol{\sigma}} = \tau(\underline{\boldsymbol{e}}_x \otimes \underline{\boldsymbol{e}}_y + \underline{\boldsymbol{e}}_y \otimes \underline{\boldsymbol{e}}_x)$$

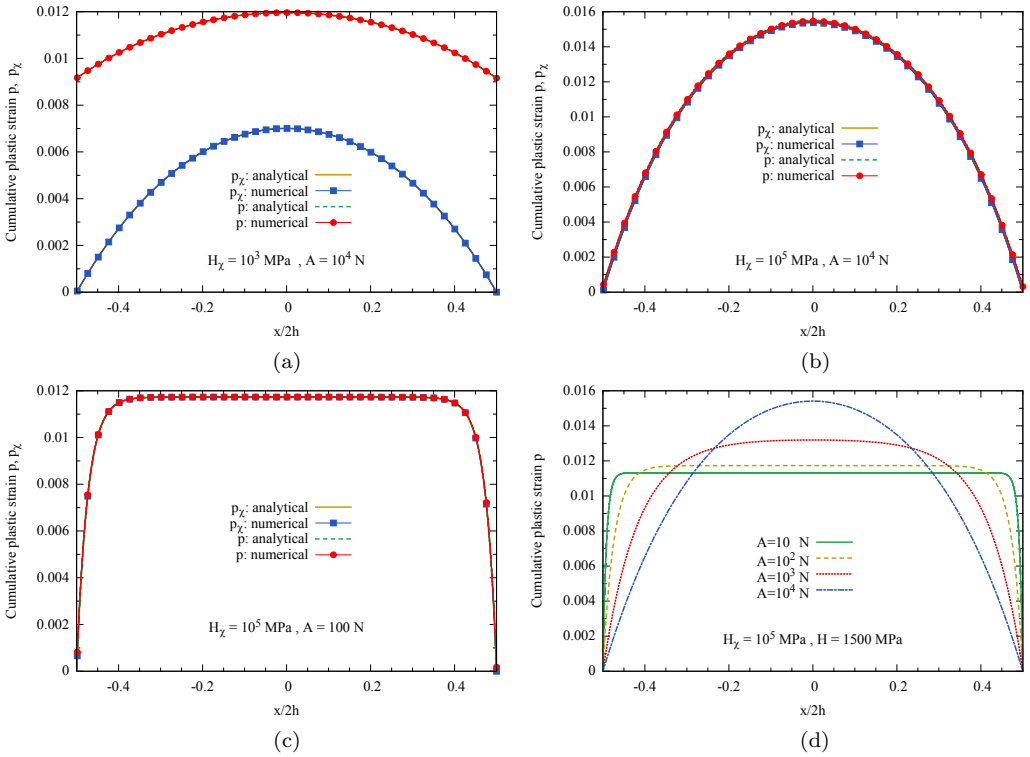

Fig. 27: The distribution of cumulative plastic strain for confined simple glide for various values of A and H_χ. Material parameters: $R_0 = 20$ MPa, $H = 1500$ MPa. The profiles are given for the prescribed overall shear value $\overline{\gamma} = 0.2$.

The localization band of finite width $2x_c < 2h$ is entirely contained in the material strip. It is assumed that no plastic flow takes place outside the localization band so that the following zones can be defined:

- $-h \le x \le -x_c$: elastic domain, labeled with "-" superscript;
- $|x| \le x_c$: plastic domain, without any label;
- $x_c \le x \le h$: elastic domain, labeled with "+" superscript.

Periodicity boundary conditions are applied at the boundaries $x = \pm h$. Solutions are derived for the micromorphic plasticity model in the small deformation framework, using the standard von Mises plasticity yield function and softening modulus $H < 0$. The limit case of the Aifantis strain gradient plasticity model is also obtained. The cumulative plastic strain field $p(x)$ and the plastic microstrain $p_\chi(x)$ are functions of the sole variable x. The displacement field takes the following form:

$$u_x = \overline{\gamma} y, \quad u_y = u(x) \tag{103}$$

where $\bar{\gamma}$ is the applied mean glide amount and $u(x)$ is the unknown displacement fluctuation. The shear strain component is

$$\varepsilon_{12} = \frac{1}{2}(\overline{\gamma} + u') = \varepsilon^e_{12} + \varepsilon^p_{12} = \varepsilon^e_{12} + \frac{\sqrt{3}}{2} p \tag{104}$$

where $u'(x) = du/dx$.

The material is described by a linear hardening law with initial yield stress R_0 and negative hardening modulus $H < 0$.

B.3.1 Solution in the elastic domain

In the elastic domain, the micro–plastic strain $p^{\pm}_\chi(x)$ is the solution of the following differential equation:

$$p^{\pm}_\chi{}'' - \omega^2_\chi p^{\pm}_\chi = 0 \quad \text{with} \quad \omega_\chi = \sqrt{\frac{H_\chi}{A}} \tag{105}$$

This equation admits solutions of exponential type with wave number ω_χ. For symmetry reasons, assuming localization at the center of the plastic zone, the plastic microstrain and higher order stress $b_x = Ap'_\chi(x)$ are respectively even and odd functions. Since b_x is periodic, it must vanish at the boundary (flat profile of microstrain):

$$p_\chi^{-\prime}(-h) = p_\chi^{+\prime}(h) = 0 \tag{106}$$

It follows that

$$p_\chi^-(x) = \alpha^- \cosh(\omega_\chi(h+x)), \quad p_\chi^+(x) = \alpha^+ \cosh(\omega_\chi(h-x)) \tag{107}$$

where $\alpha^\pm$ are integration constants to be determined from boundary conditions.

B.3.2 Solution in the plastic domain

The yield conditions reads

$$\sqrt{3}\tau = R_0 + Hp - Ap''_\chi = R_0 + Hp_\chi - \frac{A(H+H_\chi)}{H_\chi} p''_\chi \tag{108}$$

As a consequence of equilibrium, the shear stress τ is uniform. Due to the linear softening law $H < 0$, the previous equation admits harmonic solutions with the wave number

$$\omega_{\chi p} = \sqrt{\frac{|H|H_\chi}{A(H+H_\chi)}} \tag{109}$$

assuming $H+H_\chi > 0$. This defines the inverse intrinsic length $\omega_{\chi p}$ in the plastic zone. The plastic microstrain profile takes the form

$$p_\chi(x) = \frac{\sqrt{3}\tau - R_0}{H} + C\cos(\omega_{\chi p} x) \tag{110}$$

The plastic strain is obtained from the plastic microstrain field by the following equation, valid for $|x| \leq x_c$:

$$p = p_\chi - \frac{A}{H_\chi} p''_\chi = \frac{\sqrt{3}\tau - R_0}{H} + C\frac{H_\chi}{H+H_\chi}\cos(\omega_{\chi p} x) = \frac{\sqrt{3}\tau - R_0}{H} + C(1 - \frac{\omega_{\chi p}^2}{\omega_\chi^2})\cos(\omega_{\chi p} x) \tag{111}$$

The definition of the location x_c is given by

$$p(\pm x_c) = 0 = \frac{\sqrt{3}\tau - R_0}{H} + C\frac{H_\chi}{H+H_\chi}\cos(\omega_{\chi p} x_c) \tag{112}$$

Four unknowns remain: $\alpha^+, \alpha^-, C, x_c$ to be determined from left-over continuity requirements.

B.3.3 Continuity conditions

The interface conditions to be enforced are the following

- Continuity of microstrain at $x = x_c$: $p_\chi(x_c) = p_\chi^+(x_c)$

$$\alpha^+ \cosh(\omega_\chi(h - x_c)) = \frac{\sqrt{3}\tau - R_0}{H} + C\cos(\omega_{\chi p} x_c) \tag{113}$$

- Continuity of microstrain at $x = -x_c$: $p_\chi(x_c) = p_\chi^-(-x_c)$

$$\alpha^- \cosh(\omega_\chi(h - x_c)) = \frac{\sqrt{3}\tau - R_0}{H} + C\cos(\omega_{\chi p} x_c) \tag{114}$$

It follows from the two previous equations that

$$\alpha^+ = \alpha^- = \alpha \tag{115}$$

- Continuity of the higher order stress component at x_c: $b_x(x_c) = b_x^+(x_c) \implies p'_\chi(x_c) = p_\chi^{+\prime}(x_c)$

$$\alpha^+ \omega_\chi \sinh(\omega_\chi(h - x_c)) = C\omega_{\chi p}\sin(\omega_{\chi p} x_c) \tag{116}$$

- Continuity of the higher order stress component at $-x_c$:
  $b_x(-x_c) = b_x^-(-x_c) \implies p'_\chi(-x_c) = p_\chi^{-\prime}(-x_c)$
  This condition turns out to be automatically fulfilled once the result (115) is taken into account.

Only three unknowns remain, namely α, C, x_c, which are determined from the three equations (112), (113) and (116).

B.3.4 Transcendental equation for the plastic zone boundary

The equation to be solved for x_c is obtained by computing the ratio of Eq. (116) by (113):

$$\begin{aligned}\tanh(\omega_\chi(h-x_c)) &= \frac{\omega_{\chi p}}{\omega_\chi}\frac{C\sin(\omega_{\chi p}x_c)}{\frac{\sqrt{3}\tau-R_0}{H}+C\cos(\omega_{\chi p}x_c)}\\ &= \frac{\omega_{\chi p}}{\omega_\chi}\frac{C\cos(\omega_{\chi p}x_c)}{\frac{\sqrt{3}\tau-R_0}{H}+C\cos(\omega_{\chi p}x_c)}\tan(\omega_{\chi p}x_c)\\ &= \frac{\omega_{\chi p}}{\omega_\chi}\frac{H+H_\chi}{H}\tan(\omega_{\chi p}x_c)\end{aligned} \tag{117}$$

after elimination of $C\cos(\omega_{\chi p}x_c)$ term by means of (112).

The location x_c is therefore a zero of the function

$$f(y) = \tanh(\omega_\chi(h-y)) - \frac{\omega_{\chi p}}{\omega_\chi}\left(1+\frac{H_\chi}{H}\right)\tan(\omega_{\chi p}y) \tag{118}$$

which results in the announced transcendental equation.

Once x_c is determined, the constant C and α are computed from (112) and (116):

$$C = \frac{(R_0-\sqrt{3}\tau)(H+H_\chi)}{HH_\chi\cos(\omega_{\chi p}x_c)}, \quad \alpha = C\frac{\omega_{\chi p}\sin(\omega_{\chi p}x_c)}{\omega_\chi\sin(\omega_\chi(h-x_c))} \tag{119}$$

It remains to derive the relation between $\bar{\gamma}$ and τ. This is done by means of the elasticity law:

$$\frac{\tau}{\mu} = \bar{\gamma} + u' - \sqrt{3}p \tag{120}$$

Integration of this equation over the interval $[-h,h]$, after accounting for the periodicity of u, provides the relation between shear stress and applied shear strain:

$$\frac{\tau}{\mu} = \bar{\gamma} - \frac{1}{h}\left(\frac{\sqrt{3}\tau-R_0}{H}x_c - \sqrt{3}h\bar{p}\right) \tag{121}$$

where the average plastic strain is

$$\begin{aligned}\bar{p} &= \frac{1}{2h}\int_{-x_c}^{x_c} p(x)dx\\ &= \frac{1}{h}\left(\frac{\sqrt{3}\tau-R_0}{H}x_c + C(1-\frac{\omega_{\chi p}^2}{\omega_\chi^2})\sin(\omega_{\chi p}x_c)\right)\\ &= \frac{\sqrt{3}\tau-R_0}{hH}\left(x_c - \frac{\tan(\omega_{\chi p}x_c)}{\omega_{\chi p}}\right)\end{aligned} \tag{122}$$

Finally

$$\bar{\gamma} = \frac{\tau}{\mu} + \sqrt{3}\frac{\sqrt{3}\tau-R_0}{hH}\left(x_c - \frac{\tan(\omega_{\chi p}x_c)}{\omega_{\chi p}}\right) \tag{123}$$

The problem can therefore be solved for each given value of the shear stress τ. The corresponding applied shear is computed from Eq. (123). Conversely, for prescribed shear $\bar{\gamma}$, the unknowns τ and x_c are determined by solving the nonlinear system (118) an (123).

B.3.5 Limit case: strain gradient plasticity

The solution is straightforwardly found in the case of Aifantis strain gradient plasticity, either directly from the strain gradient plasticity equations or as a limit case of the previous micromorphic solution. The plastic field $p(x)$ is the solution of the yield condition

$$\sqrt{3}\tau = R_0 + Hp - Ap'' \tag{124}$$

in the whole plastic domain $|x| \le x_c$. The negative hardening modulus $H<0$ is responsible for the localization phenomenon. A harmonic solution with wave number

$$\omega_p = \sqrt{\frac{|H|}{A}} = \lim_{H_\chi\to\infty}\omega_{\chi p} \tag{125}$$

Half-strip width	$h = 5$ mm
Prescribed shear strain	$\bar{\gamma} = 0.2$
Young's modulus	$E = 78000$ MPa
Poisson ratio	$\nu = 0.3$
Initial yield stress	$R_0 = 20$ MPa
Softening modulus	$H = -20$ MPa
Strain gradient modulus	$A = 5$ N
Micromorphic penalty modulus	$H_\chi = 100$ MPa

Table 5: Geometrical, loading and material parameters for the simulation of shear localization in a strip.

is found. It is the limit of the micromorphic wave number (109) by increasing the penalty on the difference between the cumulative plastic strain p and the plastic microstrain p_χ. The boundary of the plastic zone is defined by the condition

$$p(x_c) = 0 \quad \Longrightarrow \quad x_c = \frac{\pi}{\omega_p} \tag{126}$$

Finally, the localization band can be described by the following sinus branch:

$$p(x) = \frac{\sqrt{3}\tau - R_0}{H}(1 + \cos(\omega_p x)) \tag{127}$$

with maximum plastic strain $2(\sqrt{3}\tau - R_0)/H$ at $x = 0$. Using the Hooke law (120) and periodicity of displacement, the relation between shear stress and shear strain is obtained:

$$\tau\left(\frac{1}{\mu} + \frac{3}{H}\frac{x_c}{h}\right) = \bar{\gamma} + \frac{\sqrt{3}R_0}{H}\frac{x_c}{h} \tag{128}$$

This relation is also obtained from the micromorphic solution (123) in the limit $H_\chi \to \infty$, which leads to $\tan(\omega_{\chi p} x_c) \to 0$.

B.3.6 Example and discussion of multiple solutions

The previous solutions are illustrated in a specific case characterized by the parameters given in Table 5. The analytical solutions are compared to finite element simulations based on the micromorphic plasticity model at small deformations. The finite element simulation is illustrated by the deformed states of the strip and plastic microstrain fields of Fig. 28.

The limit case of strain gradient plasticity is illustrated by Fig. 29 where the analytical solution is compared to the FE simulations using the micromorphic model with the penalty parameter $H_\chi = 10^5$ MPa. The same excellent agreement is observed using the Lagrange multiplier based model.

Fig. 30 shows that the transcendental equation $f(x) = 0$, see Eq. (118), admits three solutions for x_c in the interval $[0, h]$, namely $x_c \simeq 1.198, 2.604, 4.012$ mm.

Fig. 31 shows perfect agreement between the analytical and FE solutions, for the lowest value of x_c. The regularity of the $p_\chi(x)$ profile is clearly visible with vanishing tangents around $x = \pm 2$ mm. In contrast, the $p(x)$ function is not differentiable at $\pm x_c$ and reaches higher peak value than the smoother microplastic strain $p_\chi(x)$.

Fig. 32 and 33 show the solutions obtained for the other possible values of x_c. They correspond to the existence of 2 or 3 coexisting bands. However these solutions cannot be accepted because it is apparent that the cumulative plastic strain variable takes negative values at some places, which is forbidden. This means that these solutions must be reconsidered by taking possible elastic unloading into account. This explains why these two or three-branch solutions are not found in the FE analysis. Note also that the number of finite width localization bands is limited by the size $2h$ of the strip element.

B.3.7 Regularity of the Laplacian term

It is instructive to analyze the profiles of the Laplacian of the plastic and microplastic variables since it plays a fundamental role in the modeling approach. In the strain gradient plasticity limit case, the function $p(x)$ and its first derivative are continuous at $x = x_c$, as discussed in Sec. B.3.3 and illustrated in Fig. 29. In contrast, the second derivative

$$p''(x) = -\frac{\sqrt{3}\tau - R_0}{H}\cos(\omega_p x) \tag{129}$$

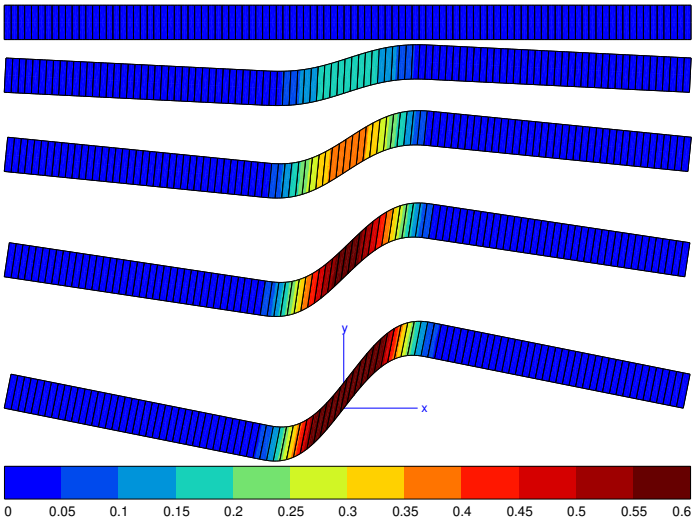

Fig. 28: Finite element simulation of shear localization in a micromorphic strip. Deformed states $\bar{\gamma} = 0.; 0.05; 0.1; 0.15; 0.2$, from top to bottom, respectively. The fields of plastic microstrain p_χ are also given. The parameters of the simulation are given in Table 5.

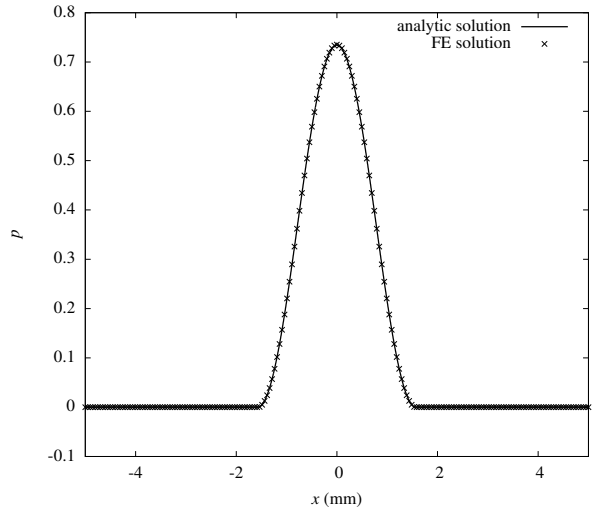

Fig. 29: Strain gradient plasticity solution of the shear localization problem with parameters listed in Table 5.

is expected to experience a discontinuity at $x = x_c$. The discontinuity takes the value

$$[\![p''(x_c)]\!] = \frac{\sqrt{3}\tau - R_0}{H}\omega_p^2 \quad \text{since} \quad \cos(\omega_p x_c) = -1 \tag{130}$$

With the parameters given in Table 5, the jump takes the value 1.47 mm^{-2}. This is clearly demonstrated by Fig. 34.

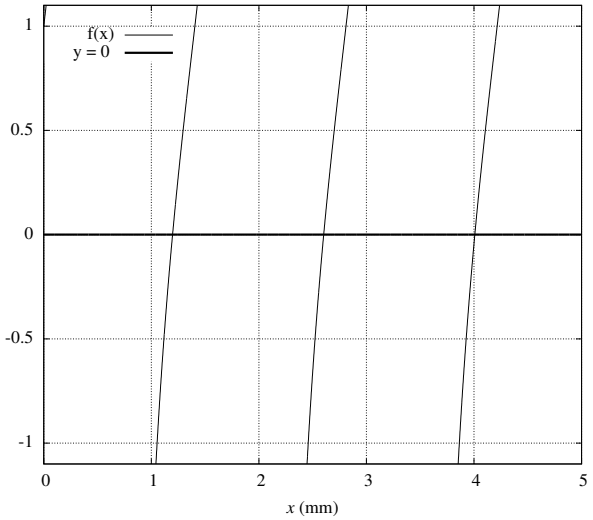

Fig. 30: Roots of the transcendental equation $f(x) = 0$ given by Eq. (118), with parameters listed in Table 5.

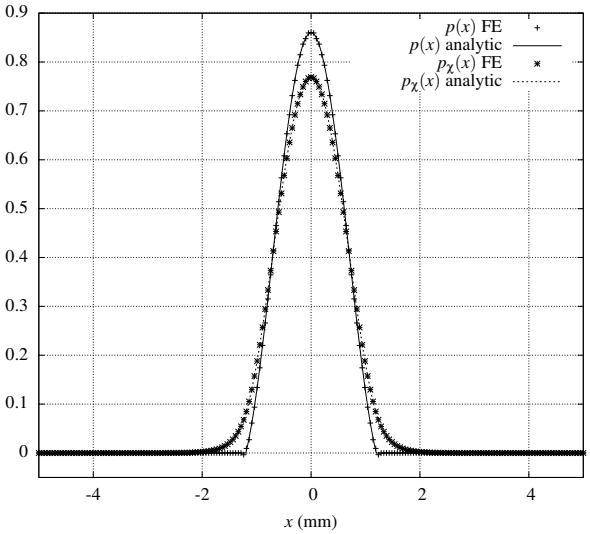

Fig. 31: Comparison between analytical and FE solutions of the shear localization problem for the micromorphic plasticity model and the smallest positive solution of the transcendental equation, with parameters listed in Table 5.

According to the micromorphic model, $p_\chi(x)$ and $p'_\chi(x)$ are continuous functions at $x = x_c$. The second derivative is computed as

$$\begin{aligned} p''_\chi(x) &= -C\omega_{\chi p}^2 \cos(\omega_{\chi p} x) \quad (|x| < x_c) \\ p^{+}{}''_\chi(x) &= \alpha\omega_\chi^2 \cosh(\omega_\chi(h - x)) \quad (x_c < x < h) \\ [\![p''_\chi(x_c)]\!] &= \alpha\omega_\chi^2 \cosh(\omega_\chi(h - x_c)) + C\cos(\omega_{\chi p} x_c)\omega_{\chi p}^2 = 0 \end{aligned}$$

The last result is obtained after consideration of Eq. (113) and (119). The Laplacian of p_χ is therefore also continuous at x_c. This is a consequence of the second balance law (84) of the micromorphic model and constitutive laws for the generalized stresses a and $\underline{\boldsymbol{b}}$. The latter equation results in PDE (86) which implies

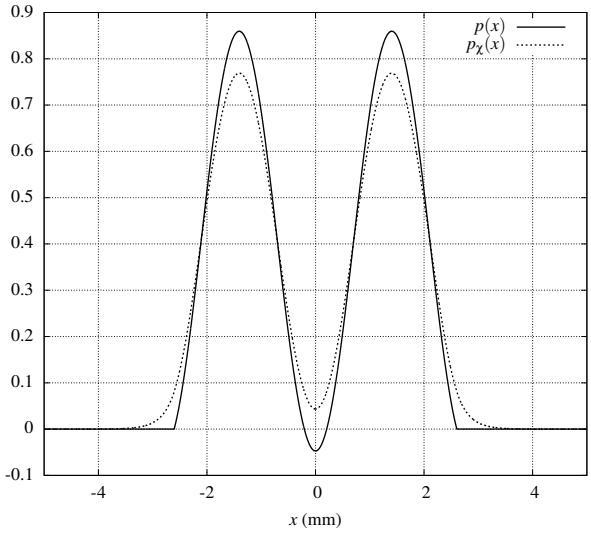

Fig. 32: Analytic solution of the shear localization problem using the second smallest positive value of x_c, with parameters listed in Table 5.

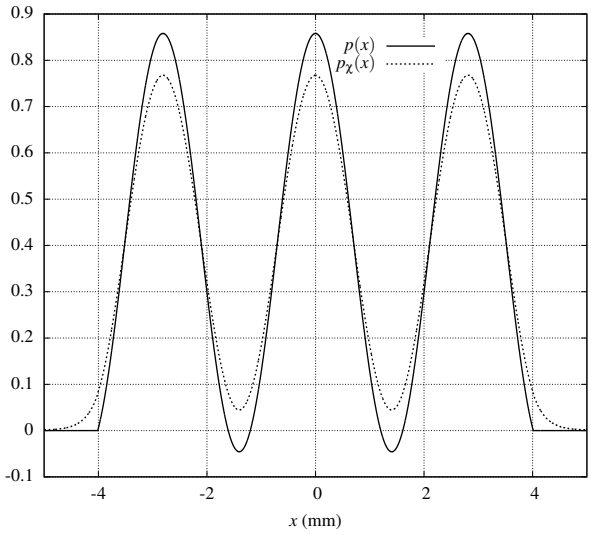

Fig. 33: Analytic solution of the shear localization problem using the third smallest positive value of x_c, with parameters listed in Table 5.

the continuity of the Laplacian Δp_χ under the condition that p is continuous as it is the case in the present example. The Laplacian is therefore continuous as soon as $p - p_\chi$ is. This does not hold for the Laplacian of $p(x)$. This is illustrated by Fig. 34 where the micromorphic response is compared to the constrained case. Note that $x_c = 1.198$ mm in the micromorphic case, which is smaller than $x_c = 1.571$ mm found in the limit case of strain gradient plasticity. This ranking is also apparent in Fig. 34.

Note that in the constrained strain gradient plasticity model, the Lagrange multiplier λ is directly proportional to the Laplace term. Its FE discretization with continuous shape functions is not compatible with the existence of discontinuities of the Laplacian. This may result in local oscillations around $x = x_c$ depending on the mesh size, see the discussion in [25].

B.3.8 Convergence of various energies to the strain gradient plasticity case

The free energy potential adopted in the considered example for the micromorphic model is

$$\rho\psi(\underset{\sim}{\varepsilon}^e, p, p_\chi, \boldsymbol{\nabla} p_\chi) = \frac{1}{2}\underset{\sim}{\varepsilon}^e : \underset{\approx}{\boldsymbol{C}} : \underset{\sim}{\varepsilon}^e + \frac{1}{2}Hp^2 + \rho\psi^\chi(p, p_\chi, \boldsymbol{\nabla} p_\chi) \tag{131}$$

where $\underset{\approx}{\boldsymbol{C}}$ denotes the fourth order tensor of elasticity. The micromorphic part of the free energy is

$$\rho\psi^\chi(p, p_\chi, \boldsymbol{\nabla} p_\chi) = \frac{1}{2}H_\chi(p - p_\chi)^2 + \frac{1}{2}A\boldsymbol{\nabla} p_\chi \cdot \boldsymbol{\nabla} p_\chi \tag{132}$$

In contrast, the Aifantis strain gradient plasticity model can be described by the following free energy potential

$$\rho\psi(\underset{\sim}{\varepsilon}^e, p, \boldsymbol{\nabla} p) = \frac{1}{2}\underset{\sim}{\varepsilon}^e : \underset{\approx}{\boldsymbol{C}} : \underset{\sim}{\varepsilon}^e + \frac{1}{2}Hp^2 + \rho\psi_\nabla(\boldsymbol{\nabla} p) \tag{133}$$

The plastic strain gradient part of the free energy is

$$\rho\psi_\nabla(\boldsymbol{\nabla} p) = \frac{1}{2}A\boldsymbol{\nabla} p \cdot \boldsymbol{\nabla} p \tag{134}$$

It is instructive to study the convergence of the micromorphic energy contribution ψ^χ towards the gradient energy ψ_∇ in the limit $H_\chi \to \infty$, in the particular case of shear localization.

The profiles of the various contributions to the free energy of the micromorphic model are drawn in Fig. 35 for two values of the penalty modulus: $H_\chi = 100$ MPa and $H_\chi = 1000$ MPa. In the more constrained case ($H_\chi = 1000$ MPa), the gradient energy ψ_∇ is found to almost coincide with the micromorphic energy ψ^χ, the penalty contribution $H_\chi(p - p_\chi)^2/2$ being negligible.

For the lower value $H_\chi = 100$ MPa, the energy densities ψ_∇ and ψ^χ differ significantly. This is due, on the one hand, to the non–negligible contribution of the $H_\chi(p-p_\chi)^2/2$ term, and, on the other hand, to high values of the gradient micromorphic contribution

$$\rho\psi^\chi_\nabla(\boldsymbol{\nabla} p_\chi) = \frac{1}{2}\boldsymbol{\nabla} p_\chi \cdot \boldsymbol{\nabla} p_\chi$$

compared to ψ_∇.

Conflict of interest

The authors declare that they have no known competing financial interests or personal relationships that could have appeared to influence the work reported in this paper.

References

1. R. Venkatraman and J.C. Bravman. Separation of film thickness and grain boundary strengthening effects in Al thin films on Si. *Journal of Materials Research*, 7(8):2040–2048, August 1992. doi: 10.1557/JMR.1992.2040.
2. J. S. Stölken and A. G. Evans. A microbend test method for measuring the plasticity length scale. *Acta Materialia*, 46(14):5109–5115, September 1998. doi: 10.1016/S1359-6454(98)00153-0.
3. N.A. Fleck and J.W. Hutchinson. Strain gradient plasticity. *Adv. Appl. Mech.*, 33:295–361, 1997.
4. Y. Mu, X. Zhang, J.W. Hutchinson, and W.J. Meng. Dependence of confined plastic flow of polycrystalline Cu thin films on microstructure. *MRS Communications*, 6:289–294, 2016. doi: 10.1557/mrc.2016.20.
5. J.F. Nye. Some geometrical relations in dislocated crystals. *Acta Metallurgica*, 1:152–162, 1953.
6. M. F. Ashby. The deformation of plastically non-homogeneous materials. *The Philosophical Magazine: A Journal of Theoretical Experimental and Applied Physics*, 21(170):399–424, February 1970. doi: 10.1080/14786437008238426.
7. N. A. Fleck and J. W. Hutchinson. A phenomenological theory for strain gradient effects in plasticity. *Journal of the Mechanics and Physics of Solids*, 41(12):1825–1857, December 1993. doi: 10.1016/0022-5096(93)90072-N.
8. R. de Borst, J. Pamin, and L.J. Sluys. Computational issues in gradient plasticity. *In: Continuum models for materials with microstructure*, pages 159–200, 1995. Publisher: Wiley.
9. M. Mazière and S. Forest. Strain gradient plasticity modeling and finite element simulation of Lüders band formation and propagation. *Continuum Mechanics and Thermodynamics*, 27(1):83–104, January 2015. doi: 10.1007/s00161-013-0331-8.

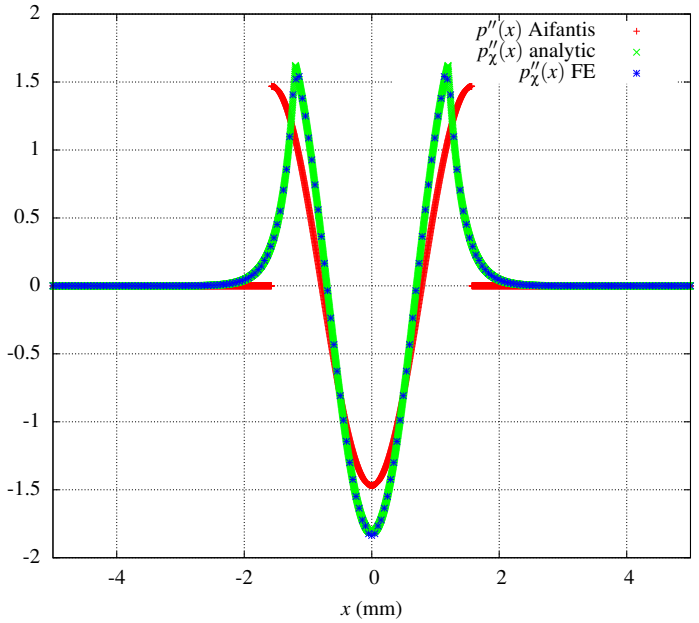

Fig. 34: Profiles of the Laplacian of plastic strain $p''(x)$ in the limit case of strain gradient plasticity (Aifantis model) and $p''_\chi(x)$ in the micromorphic case, with parameters given in Table 5. Analytic and FE results are compared.

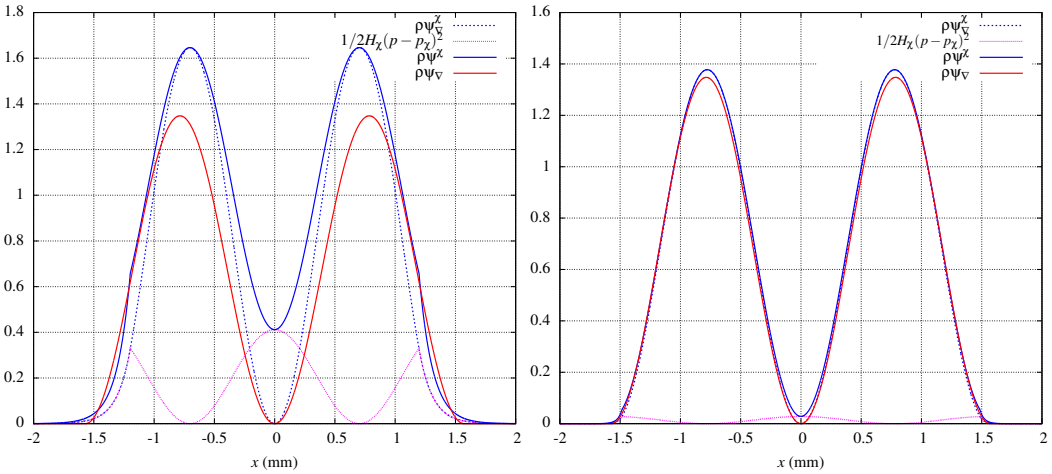

Fig. 35: Various energy profiles in the shear localization zone. The predictions of the micromorphic model for two values of the penalty modulus ($H_\chi = 100$ MPa on the left, $H_\chi = 1000$ MPa on the right) are compared to the strain gradient plasticity solution. The other parameters are taken from Table 5.

10. A. S. Botta, W. S. Venturini, and A. Benallal. BEM applied to damage models emphasizing localization and associated regularization techniques. *Engineering Analysis with Boundary Elements*, 29(8):814–827, August 2005. doi: 10.1016/j.enganabound.2005.04.006.
11. R. de Borst, J. Pamin, and M. G. D. Geers. On coupled gradient-dependent plasticity and damage theories with a view to localization analysis. *European Journal of Mechanics - A/Solids*, 18(6):939–962, November 1999. doi: 10.1016/S0997-7538(99)00114-X.

12. R. H. J. Peerlings, R. de Borst, W. a. M. Brekelmans, and J. H. P. De Vree. Gradient enhanced damage for quasi-brittle materials. *International Journal for Numerical Methods in Engineering*, 39 (19):3391–3403, 1996. doi: 10.1002/(SICI)1097-0207(19961015)39:19⟨3391::AID-NME7⟩3.0.CO;2-D.
13. A. Needleman. Material rate dependence and mesh sensitivity in localization problems. *Computer Methods in Applied Mechanics and Engineering*, 67(1):69–85, March 1988. doi: 10.1016/0045-7825(88)90069-2.
14. K. Saanouni and M. Hamed. Micromorphic approach for finite gradient-elastoplasticity fully coupled with ductile damage: Formulation and computational aspects. *International Journal of Solids and Structures*, 50(14):2289–2309, July 2013. doi: 10.1016/j.ijsolstr.2013.03.027.
15. V. Davaze, N. Vallino, B. Langrand, J. Besson, and S. Feld-Payet. A non-local damage approach compatible with dynamic explicit simulations and parallel computing. *International Journal of Solids and Structures*, 228:110999, 2021. doi: 10.1016/j.ijsolstr.2021.02.010.
16. R. Russo, V. Phalke, D. Croizet, M. Ziane, S. Forest, F.A. Girot Mata, H.J. Chang, and A. Roos. Regularization of shear banding and prediction of size effects in manufacturing operations: A micromorphic plasticity explicit scheme. *International Journal of Material Forming*, 15:21, 2022. doi: 10.1007/s12289-022-01657-9.
17. A. C. Eringen and E. S. Suhubi. Nonlinear theory of simple micro-elastic solids–I. *International Journal of Engineering Science*, 2(2):189–203, May 1964. doi: 10.1016/0020-7225(64)90004-7.
18. E. S. Suhubi and A. C. Eringen. Nonlinear theory of micro-elastic solids—II. *International Journal of Engineering Science*, 2(4):389–404, October 1964. doi: 10.1016/0020-7225(64)90017-5.
19. P. Germain. The method of virtual power in continuum mechanics. part 2: microstructure. *SIAM Journal on Applied Mathematics*, 25(3):556–575, November 1973. doi: 10.1137/0125053. Publisher: Society for Industrial and Applied Mathematics.
20. S. Forest. Micromorphic approach for gradient elasticity, viscoplasticity, and damage. *Journal of Engineering Mechanics*, 135(3):117–131, March 2009. doi: 10.1061/(ASCE)0733-9399(2009)135:3(117).
21. B. Kiefer, T. Waffenschmidt, L. Sprave, and A. Menzel. A gradient-enhanced damage model coupled to plasticity-multi-surface formulation and algorithmic concepts. *International Journal of Damage Mechanics*, 27:253–295, 2018. doi: 10.1177/1056789516676306.
22. S. Wulfinghoff and T. Böhlke. Equivalent plastic strain gradient enhancement of single crystal plasticity: theory and numerics. *Proceedings of the Royal Society A: Mathematical, Physical and Engineering Sciences*, 468(2145):2682–2703, September 2012. doi: 10.1098/rspa.2012.0073. Publisher: Royal Society.
23. C. Ling, S. Forest, J. Besson, B. Tanguy, and F. Latourte. A reduced micromorphic single crystal plasticity model at finite deformations. Application to strain localization and void growth in ductile metals. *International Journal of Solids and Structures*, 134:43–69, 2018. doi: 10.1016/j.ijsolstr.2017.10.013.
24. J.M. Scherer, J. Besson, S. Forest, J. Hure, and B. Tanguy. Strain gradient crystal plasticity with evolving length scale: Application to voided irradiated materials. *European Journal of Mechanics - A/Solids*, 77:103768, September 2019. doi: 10.1016/j.euromechsol.2019.04.003.
25. J.M. Scherer, V. Phalke, J. Besson, S. Forest, J. Hure, and B. Tanguy. Lagrange multiplier based vs micromorphic gradient-enhanced rate-(in)dependent crystal plasticity modelling and simulation. *Computer Methods in Applied Mechanics and Engineering*, 372:113426, December 2020. doi: 10.1016/j.cma.2020.113426.
26. N. Ohno and D. Okumura. Higher–order stress and grain size effects due to self–energy of geometrically necessary dislocations. *Journal of the Mechanics and Physics of Solids*, 55:1879–1898, 2007.
27. S. Forest. Questioning size effects as predicted by strain gradient plasticity. *Journal of the Mechanical Behavior of Materials*, 22:101–110, 2013.
28. V.L. Berdichevsky. Continuum theory of dislocations revisited. *Continuum Mechanics and Thermodynamics*, 18:195–222, 2006.
29. B. Svendsen and S. Bargmann. On the continuum thermodynamic rate variational formulation of models for extended crystal plasticity at large deformation. *Journal of the Mechanics and Physics of Solids*, 58:1253–1271, 2010.
30. S. Forest and N. Guéninchault. Inspection of free energy functions in gradient crystal plasticity. *Acta Mechanica Sinica*, 29:763–772, 2013.
31. S. Wulfinghoff, S. Forest, and T. Böhlke. Strain gradient plasticity modeling of the cyclic behavior of laminate microstructures. *Journal of the Mechanics and Physics of Solids*, 79:1–20, June 2015. doi: 10.1016/j.jmps.2015.02.008.
32. C. Nellemann, C.F. Niordson, and K.L. Nielsen. Hardening and strengthening behavior in rate-independent strain gradient crystal plasticity. *European Journal of Mechanics - A/Solids*, 67:157 – 168, 2018. doi: https://doi.org/10.1016/j.euromechsol.2017.09.006.
33. S.A. El-Naaman, K.L. Nielsen, and C.F. Niordson. An investigation of back stress formulations under cyclic loading. *Mechanics of Materials*, 130:76–87, 2019. doi: 10.1016/j.mechmat.2019.01.005.
34. L. Bardella. Size effects in phenomenological strain gradient plasticity constitutively involving the plastic spin. *International Journal of Engineering Science*, 48:550–568, 2010. doi: 10.1016/j.ijengsci.2010.01.003.

35. E. Bayerschen and T. Böhlke. Power-law defect energy in a single-crystal gradient plasticity framework: a computational study. *Computational Mechanics*, 58:13–27, 2016. doi: 10.1007/s00466-016-1279-x.
36. M. Jebahi, L. Cai, and F. Abed-Meraim. Strain gradient crystal plasticity model based on generalized non-quadratic defect energy and uncoupled dissipation. *International Journal of Plasticity*, 126:102617, 2020. doi: 10.1016/j.ijplas.2019.10.005.
37. M. Abatour, K. Ammar, S. Forest, C. Ovalle-Rodas, N. Osipov, and S. Quilici. A generic formulation of anisotropic thermo-elastoviscoplasticity at finite deformations for Finite Element codes. working paper or preprint, 2021. URL hal.archives-ouvertes.fr/hal-03462216v2.
38. A. E. Green and P. M. Naghdi. A general theory of an elastic-plastic continuum. *Archive for Rational Mechanics and Analysis*, 18(4):251–281, January 1965. doi: 10.1007/BF00251666.
39. C. Miehe, N. Apel, and M. Lambrecht. Anisotropic additive plasticity in the logarithmic strain space: modular kinematic formulation and implementation based on incremental minimization principles for standard materials. *Computer Methods in Applied Mechanics and Engineering*, 191(47):5383–5425, November 2002. doi: 10.1016/S0045-7825(02)00438-3.
40. E. Kröner. Allgemeine Kontinuumstheorie der Versetzungen und Eigenspannungen. *Archive for Rational Mechanics and Analysis*, 4(1):273–334, January 1959. doi: 10.1007/BF00281393.
41. E. H. Lee and D. T. Liu. Finite strain elastic-plastic theory with application to plane-wave analysis. *Journal of Applied Physics*, 38(1):19–27, January 1967. doi: 10.1063/1.1708953.
42. J. Mandel. Equations constitutives et directeurs dans les milieux plastiques et viscoplastiques. *International Journal of Solids and Structures*, 9(6):725–740, June 1973. doi: 10.1016/0020-7683(73)90120-0.
43. S. Forest and R. Sievert. Elastoviscoplastic constitutive frameworks for generalized continua. *Acta Mechanica*, 160:71–111, 2003.
44. S. Forest. Nonlinear regularization operators as derived from the micromorphic approach to gradient elasticity, viscoplasticity and damage. *Proceedings of the Royal Society A: Mathematical, Physical and Engineering Sciences*, 472(2188):20150755, April 2016. doi: 10.1098/rspa.2015.0755.
45. J. Friedlein, J. Mergheim, and P. Steinmann. Observations on additive plasticity in the logarithmic strain space at excessive strains. *International Journal of Solids and Structures*, 239-240:111416, March 2022. doi: 10.1016/j.ijsolstr.2021.111416.
46. P. Steinmann. Formulation and computation of geometrically non-linear gradient damage. *International Journal for Numerical Methods in Engineering*, 46(5):757–779, 1999. doi: 10.1002/(SICI)1097-0207(19991020)46:5⟨757::AID-NME731⟩3.0.CO;2-N.
47. M.G.D. Geers, R.A.B. Engelen, and R.J.M. Ubachs. On the numerical modelling of ductile damage with an implicit gradient-enhanced formulation. *Revue Européenne des Éléments Finis*, 10(2-4):173–191, 2001. doi: 10.1080/12506559.2001.11869246.
48. M. G. D. Geers, R. L. J. M. Ubachs, and Roy A.B. Engelen. Strongly non-local gradient-enhanced finite strain elastoplasticity. *International Journal for Numerical Methods in Engineering*, 56(14):2039–2068, 2003. doi: 10.1002/nme.654.
49. M. G. D. Geers. Finite strain logarithmic hyperelasto-plasticity with softening: a strongly non-local implicit gradient framework. *Computer Methods in Applied Mechanics and Engineering*, 193(30):3377–3401, July 2004. doi: 10.1016/j.cma.2003.07.014.
50. E. Martinez-Paneda and C.F. Niordson. On fracture in finite strain gradient plasticity. *International Journal of Plasticity*, 80:154–167, 2016. doi: 10.1016/j.ijplas.2015.09.009.
51. L. Anand, O. Aslan, and S. A. Chester. A large-deformation gradient theory for elastic–plastic materials: Strain softening and regularization of shear bands. *International Journal of Plasticity*, 30-31:116–143, March 2012. doi: 10.1016/j.ijplas.2011.10.002.
52. Y. Zhang, E. Lorentz, and J. Besson. Ductile damage modelling with locking-free regularised GTN model. *International Journal for Numerical Methods in Engineering*, 113(13):1871–1903, 2018. doi: 10.1002/nme.5722.
53. L. H. Poh, R.H.J. Peerlings, M.G.D. Geers, and S. Swaddiwudhipong. An implicit tensorial gradient plasticity model – Formulation and comparison with a scalar gradient model. *International Journal of Solids and Structures*, 48(18):2595–2604, September 2011. doi: 10.1016/j.ijsolstr.2011.05.019.
54. S. Wulfinghoff, E. Bayerschen, and T. Böhlke. Conceptual difficulties in plasticity including the gradient of one scalar plastic field variable. *PAMM*, 14(1):317–318, 2014. doi: 10.1002/pamm.201410146.
55. M. Jebahi and S. Forest. Scalar-based strain gradient plasticity theory to model size-dependent kinematic hardening effects. *Continuum Mechanics and Thermodynamics*, 33(4):1223–1245, 2021. doi: 10.1007/s00161-020-00967-0.
56. Morton E. Gurtin. On a framework for small-deformation viscoplasticity: free energy, microforces, strain gradients. *International Journal of Plasticity*, 19:47–90, 2003. doi: 10.1016/S0749-6419(01)00018-3.
57. P. Gudmundson. A unified treatment of strain gradient plasticity. *Journal of the Mechanics and Physics of Solids*, 52:1379–1406, 2004. doi: https://doi.org/10.1016/j.jmps.2003.11.002.
58. N.A. Fleck and J.R. Willis. A mathematical basis for strain-gradient plasticity theory. Part II: Tensorial plastic multiplier. *Journal of the Mechanics and Physics of Solids*, 57(7):1045–1057, July 2009. doi: 10.1016/j.jmps.2009.03.007.
59. E. Lorentz and A. Benallal. Gradient constitutive relations: numerical aspects and application to gradient damage. *Computer Methods in Applied Mechanics and Engineering*, 194(50):5191–5220, December 2005.

doi: 10.1016/j.cma.2004.12.016.
60. Y. Chen, E. Lorentz, and J. Besson. Crack initiation and propagation in small-scale yielding using a nonlocal GTN model. *International Journal of Plasticity*, 130:102701, July 2020. doi: 10.1016/j.ijplas.2020.102701.
61. Y. Chen, E. Lorentz, A. Dahl, and J. Besson. Simulation of ductile tearing during a full size test using a non local Gurson–Tvergaard–Needleman (GTN) model. *Engineering Fracture Mechanics*, 261:108226, February 2022. doi: 10.1016/j.engfracmech.2021.108226.
62. S. Felder, N. Kopic-Osmanovic, H. Holthusen, T. Brepols, and S. Reese. Thermo-mechanically coupled gradient-extended damage-plasticity modeling of metallic materials at finite strains. *International Journal of Plasticity*, 148:103142, 2022. doi: 10.1016/j.ijplas.2021.103142.
63. J. Besson, G. Cailletaud, J.-L. Chaboche, and S. Forest. *Non-linear mechanics of materials*. Solid Mechanics and Its Applications. Springer Netherlands, 2010. ISBN 978-90-481-3355-0. doi: 10.1007/978-90-481-3356-7.
64. J. P. Boehler. *Applications of tensor functions in solid mechanics*. CISM Courses and Lectures No. 292, Udine, Springer Verlag, Wien, 1987. doi: https://doi.org/10.1007/978-3-7091-2810-7.
65. Q.S. Zheng. Theory of representations for tensor functions–A unified invariant approach to constitutive equations. *Applied Mechanics Review*, 47:545–587, 1994.
66. E. C. Aifantis. On the microstructural origin of certain inelastic models. *Journal of Engineering Materials and Technology*, 106(4):326–330, October 1984. doi: 10.1115/1.3225725.
67. S. Forest and E. C. Aifantis. Some links between recent gradient thermo-elasto-plasticity theories and the thermomechanics of generalized continua. *International Journal of Solids and Structures*, 47(25):3367–3376, December 2010. doi: 10.1016/j.ijsolstr.2010.07.009.
68. Z-set. Non-linear material & structure analysis suite, 2022. URL www.zset-software.com.
69. J. Besson and R. Foerch. Large scale object–oriented finite element code design. *Computer Methods in Applied Mechanics and Engineering*, 142:165–187, 1997.
70. R. Foerch, J. Besson, G. Cailletaud, and P. Pilvin. Polymorphic constitutive equations in finite element codes. *Computer Methods in Applied Mechanics and Engineering*, 141:355–372, 1997.
71. E. Bittencourt, A. Needleman, Gurtin M.E., and E. Van der Giessen. A comparison of nonlocal continuum and discrete dislocation plasticity predictions. *Journal of the Mechanics and Physics of Solids*, 51:281–310, 2003.
72. N. A. Fleck, J. W. Hutchinson, and J. R. Willis. Guidelines for constructing strain gradient plasticity theories. *J. Appl. Mech.*, 82:071002, 2015. ISSN 0021-8936.
73. C. Mareau. Thermodynamic framework for variance-based non-local constitutive models. *Continuum Mech. Thermodyn.*, 34:1173–1195, 2022. doi: 10.1007/s00161-022-01113-8.
74. Geralf Hütter. Homogenization of a cauchy continuum towards a micromorphic continuum. *Journal of the Mechanics and Physics of Solids*, 99:394–408, 2017. doi: 10.1016/j.jmps.2016.09.010.
75. R.H.J. Peerlings. On the role of moving elastic–plastic boundaries in strain gradient plasticity. *Modelling and Simulation in Materials Science and Engineering*, 15(1):S109–S120, January 2007. doi: 10.1088/0965-0393/15/1/S10.
76. D. Nouailhas and G. Cailletaud. Tension-torsion behavior of single-crystal superalloys: experiment and finite element analysis. *International Journal of Plasticity*, 11(4):451–470, January 1995. doi: 10.1016/S0749-6419(98)80004-1.
77. F. Ghiglione and S. Forest. On the torsion of isotropic elastoplastic Cosserat circular cylinders. *Journal of Micromechanics and Molecular Physics*, 6:1–14, 2022. doi: 10.1142/S2424913021420078.
78. V. Phalke, T. Kaiser, J. M. Scherer, and S. Forest. Modeling size effects in microwire torsion: A comparison between a lagrange multiplier-based and a CurlF^p gradient crystal plasticity model. *European Journal of Mechanics A/Solids*, 94:104550, 2021. doi: 10.1016/j.euromechsol.2022.104550.
79. Y. Xu and L.-H. Poh. Localizing gradient-enhanced rousselier model for ductile fracture. *International Journal for Numerical Methods in Engineering*, 119:826–851, 2019. doi: 10.1002/nme.6074.
80. S. Sarkar, I.V. Singh, and B.K. Mishra. A localizing gradient plasticity model for ductile fracture. *Computer Methods in Applied Mechanics and Engineering*, 388:114205, 2022. doi: 10.1016/j.cma.2021.114205.
81. S. Yasayanlar, B. Kaçmaz, and I. Özdemir. Localizing implicit gradient damage based treatment of softening in elasto-plasticity. *Procedia Structural Integrity*, 35:18–24, 2022. doi: 10.1016/j.prostr.2021.12.043.
82. E. Diamantopoulou, W. Liu, C. Labergere, H. Badreddine, K. Saanouni, and P. Hu. Micromorphic constitutive equations with damage applied to metal forming. *International Journal of Damage Mechanics*, 26:314–339, 2017. doi: 10.1177/1056789516684650.
83. C. Miehe. A multifield incremental variational framework for gradient type standard dissipative solids. *Journal of the Mechanics and Physics of Solids*, 59:898–923, 2011.
84. U.F. Kocks and H. Mecking. Physics and phenomenology of strain hardening: the FCC case. *Progress in Materials Science*, 48(3):171–273, January 2003. doi: 10.1016/S0079-6425(02)00003-8.
85. S. Ren, M. Mazière, S. Forest, T.F. Morgeneyer, and G. Rousselier. A constitutive model accounting for strain ageing effects on work-hardening. Application to a C–Mn steel. *Comptes Rendus Mécanique*, 345(12):908–921, December 2017. doi: 10.1016/j.crme.2017.09.005.

86. O. Aslan, N.M. Cordero, A. Gaubert, and S. Forest. Micromorphic approach to single crystal plasticity and damage. *International Journal of Engineering Science*, 49(12):1311–1325, December 2011. doi: 10.1016/j.ijengsci.2011.03.008.
87. M. E. Gurtin. A gradient theory of small-deformation isotropic plasticity that accounts for the burgers vector and for dissipation due to plastic spin. *Journal of the Mechanics and Physics of Solids*, 52: 2545–2568, 2004. doi: 10.1016/j.jmps.2004.04.010.
88. L. Bardella. On a mixed energetic-dissipative constitutive law for non-proportional loading, with focus on small-scale plasticity. *Proceedings of the Royal Society A*, 477:20200940, 2021. doi: 10.1098/rspa.2020.0940.
89. M. Fassin, R. Eggersmann, S. Wulfinghoff, and S. Reese. Gradient-extended anisotropic brittle damage modeling using a second order damage tensor - Theory, implementation and numerical examples. *International Journal of Solids and Structures*, 167:93 – 126, 2019. doi: 10.1016/j.ijsolstr.2019.02.009.
90. K. Langenfeld and J. Mosler. A micromorphic approach for gradient-enhanced anisotropic ductile damage. *Computer Methods in Applied Mechanics and Engineering*, 360:112717, 2020. doi: 10.1016/j.cma.2019.112717.
91. L. Sprave and A. Menzel. A large strain gradient-enhanced ductile damage model: finite element formulation, experiment and parameter identification. *Acta Mechanica*, 231:5159–5192, 2020. doi: 10.1007/s00707-020-02786-5.
92. H. Holthusen, T. Brepols, S. Reese, and J.-W. Simon. A two-surface gradient-extended anisotropic damage model using a second order damage tensor coupled to additive plasticity in the logarithmic strain space. *Journal of the Mechanics and Physics of Solids*, 163:104833, 2022. doi: 10.1016/j.jmps.2022.104833.
93. M. Rezaee-Hajidehi, P. Sadowski, and S. Stupkiewicz. Deformation twinning as a displacive transformation: Finite-strain phase-field model of coupled twinning and crystal plasticity. *Journal of the Mechanics and Physics of Solids*, 163:104855, 2022. doi: 10.1016/j.jmps.2022.104855.
94. V. Davaze, N. Vallino, S. Feld-Payet, B. Langrand, and J. Besson. Plastic and fracture behavior of a dual phase steel sheet under quasi-static and dynamic loadings. *Engineering Fracture Mechanics*, 235: 107165, 2020. doi: 10.1016/j.engfracmech.2020.107165.